COMPUTATIONAL STUDIES OF THE EFFECTS OF ACTIVE AND PASSIVE CIRCULATION ENHANCEMENT CONCEPTS ON WIND TURBINE PERFORMANCE

A Dissertation
Presented to
The Academic Faculty

by

Chanin Tongchitpakdee

In Partial Fulfillment
of the Requirements for the Degree
Doctor of Philosophy in the
School of Aerospace Engineering

Georgia Institute of Technology
August 2007

COMPUTATIONAL STUDIES OF THE EFFECTS OF ACTIVE AND PASSIVE CIRCULATION ENHANCEMENT CONCEPTS ON WIND TURBINE PERFORMANCE

Approved by:

Dr. Lakshmi N. Sankar, Advisor
School of Aerospace Engineering
Georgia Institute of Technology

Dr. John W. Holmes
School of Aerospace Engineering
Georgia Institute of Technology

Dr. Stephen M. Ruffin
School of Aerospace Engineering
Georgia Institute of Technology

Dr. Jechiel I. Jagoda
School of Aerospace Engineering
Georgia Institute of Technology

Prof. Robert J. Englar
Georgia Tech Research Institute
Georgia Institute of Technology

Date Approved: June 11, 2007

Dedicated to my parents

Wichien and Wanwipa Tongchitpakdee

ACKNOWLEDGEMENTS

I would like to express my sincere gratitude and heartfelt appreciation to my thesis advisor and mentor, Dr. Lakshmi N. Sankar, for his encouragement and invaluable support throughout my school years at Georgia Tech. His knowledge and experience has guided me along the way, and his understanding and kindness has encouraged me to accomplish this research work. His great personality and being a great teacher will definitely be the biggest influence in my future academic and research career. It is my pleasure to say that pursuing my doctorate under his guidance made my life at Georgia Tech a very valuable, positive learning experience.

I would also like to thank Dr. Stephen Ruffin, Professor Robert Englar, Dr. John Holmes and Dr. Jeff Jagoda for their services as members of my thesis committee. I am grateful to their continued guidance and support, thorough review of my thesis and valuable comments.

I would like to acknowledge the National Renewable Energy Laboratory for sponsoring this research under contract No. XCX-2-32227-02. I am grateful to Dr. Scott Schreck, the technical monitor, for providing experimental data, and for his many valuable comments. I would also like to acknowledge the Anandamahidol Foundation Thailand for providing me financial support and opportunity for this important accomplishment of my life.

I would especially like to thank Dr. Jeff Jagoda, Associate Chair for Graduate Studies and Research, for being very helpful and supportive whenever I needed

assistance during my school years. I would like to thank the administrative staff at School of Aerospace Engineering, especially Loretta Carroll, for all help they have provided me.

I would like to thank all my past and present colleagues in CFD lab, Dr. Liu Yi, Dr. Roxana Vasilescu, Dr. Sarun Benjanirat, Vishwas Iyengar, Sujeet Phanse, Joseph Gillman, Jingshu Wu, Goktan Guzel, Mina Zaki, Nischint Rajmohan, Nandita Yeshala, Byung Young Min, Jeremy Bain, and Lan Wu, for their friendship and support during my years in the lab. I also thank all of my Thai friends both here in Atlanta, and in Thailand for all support they have given me.

I would like to dedicate this thesis work to my parents for their unconditional endless love and continued support throughout my entire educational journey. Last but not least, I would like to express my deepest love and appreciation to my fiancé, Sasitorn Chantanawarangoon, for her love and support. Without her encouragement and warm care, this research work could not have been completed.

TABLE OF CONTENTS

LIST OF TABLES

LIST OF FIGURES

NOMENCLATURE

a	Speed of sound
A	Area
A, B, C	Flux Jacobian matrices
c	Chord length
C_D	Drag force coefficient
C_L	Lift force coefficient
C_M	Pitching moment coefficient
C_N	Normal force coefficient
c_p	Pressure coefficient
C_p	Specific heat at constant pressure
C_T	Tangential force coefficient
C_μ	Jet momentum coefficient
$C_{\mu,0}$	Time-averaged momentum coefficient for pulsed jets
d	Distant from the wall
D	Drag force
e	Internal energy
$\tilde{e}$	Internal energy per unit mass
f_{v1}	Damping function for Spalart-Allmaras model
F(t)	Function of time

F, G, H	Inviscid flux matrices
$\vec{i}, \vec{j}, \vec{k}$	Cartesian unit vectors
I	Identity metric
J	Jacobian of transformation
k	Thermal conductivity
L	Lift force, Length
L, D, U	Lower, diagonal and upper block triangular matrix
$\dot{m}$	Mass flow rate
M	Mach number
$O(.)$	Order of variable
p	Pressure
Pr	Prandtl number
Pr_T	Turbulent Prandtl number
q	State variable vector
r	Radial position from rotor hub, Roughness factor
R	Rotor radius, Gas constant
Re	Reynolds number
RHS	Shorthand notation for the terms on the right hand side for any equation
R, S, T	Viscous flux matrices
S	Vorticity
t	Time in physical domain
T	Temperature

T_0	Total temperature
u, v, w	Cartesian components of velocity
U^+, U^-	Convection velocity used in upwind scheme
U, V, W	Contravariant velocities
V	Velocity
$\vec{V}_{grid}$	Grid velocity
$\vec{V}_{induced}$	Induced velocity
$\vec{V}_{wind}$	Wind velocity
x, y, z	Cartesian coordinates
y^+	Viscous sublayer length scale, $y(\tau_w / \rho)^{1/2} / \nu_\infty$

Greek Symbols

Δ	Forward difference operator
∇	Backward difference operator
δ	Central difference operator
γ	Specific heat ratio
θ	Momentum thickness
ρ	Density
Ω	Rotational speed
τ	Non-dimensional time
τ_{ij}	Shear stress tensor component

τ_w	Wall shear stress
ξ, η, ζ	Computational coordinate system
μ	Molecular viscosity
μ_T	Turbulent viscosity
$\tilde{\nu}$	Undamped turbulent viscosity

Subscripts

∞	Free-stream value
i, j, k	Indices in three coordinate directions
jet	Variable at the jet slot exit
L, R	Left and right sides of the cell faces
ref	Reference value
t	Derivative with respect to physical time
τ	Derivative with respect to time in (ξ, η, ζ) coordinates
w	Variable on the wall surface
x, y, z	Derivatives with respect to Cartesian coordinates
ξ, η, ζ	Derivatives with respect to generalized coordinates

Superscripts

$n, n+1$	Time level
$*$	Non-dimensional variable
^	Variable in the computational domain

–	Mean value of the flow variable
'	Fluctuation quantity after average
+	Positive eigenvalue
-	Negative eigenvalue
~	Roe-averaged quantity

Acronyms and Abbreviations

2-D	Two Dimensional
3-D	Three Dimensional
CC	Circulation Control
CCW	Circulation Control Wing
CER	Combined Experiment Rotor
CFD	Computational Fluid Dynamics
DES	Detached Eddy Simulation
DNS	Direct Numerical Simulation
GFRP	Glass-Fibre Reinforced Plastic
HAWT	Horizontal Axis Wind Turbine
LE	Leading Edge
LES	Large Eddy Simulation
LU-SGS	Lower-Upper Symmetric Gauss Seidel
MUSCL	Monotone Upstream-centered Scheme for Conservation Laws
NACA	National Advisory Committee for Aeronautics
NASA	National Aeronautics and Space Administration

NREL	National Renewable Energy Laboratory
RANS	Reynolds-Averaged Navier-Stokes
RHS	Right Hand Side
SA	Spalart-Allmaras
SA-DES	Spalart-Allmaras based Detached Eddy Simulation
TE	Trailing edge
VAWT	Vertical Axis Wind Turbine

SUMMARY

With the advantage of modern high speed computers, there has been an increased interest in the use of first-principles based computational approaches for the aerodynamic modeling of horizontal axis wind turbine (HAWT). Since these approaches are based on the laws of conservation (mass, momentum, and energy), they can capture much of the physics in great detail. The ability to accurately predict the airloads and power output can greatly aid the designers in tailoring the aerodynamic and aeroelastic features of the configuration. First-principles based analyses are also valuable for developing active means (e.g., circulation control), and passive means (e.g., Gurney flap) of reducing unsteady blade loads, mitigating stall, and for efficient capture of wind energy leading to more electrical power generation.

In this present study, the aerodynamic performance of a wind turbine rotor equipped with circulation enhancement technology (trailing edge blowing or Gurney flap) is investigated using a three-dimensional unsteady viscous flow analysis. The National Renewable Energy Laboratory (NREL) Phase VI horizontal axis wind turbine is chosen as the baseline configuration. Prior to its use in exploring these concepts, the flow solver is validated with the experimental data for the baseline case under yawed flow conditions. The conditions chosen for study range from fully attached flow to fully separated flow. Results presented include radial distribution of normal and tangential forces, shaft torque, root flap moment, surface pressure distributions at selected radial locations, and power output. Results show that good agreement has been for a range of wind speeds and yaw angles, where the flow is attached. At high wind speeds, however,

where the flow is fully separated, it is found that the fundamental assumptions behind this present methodology breaks down for the baseline turbulence model (Spalart-Allmaras model), giving less accurate results. With the implementation of advanced turbulence model (SA-DES model), the accuracy of the results at high wind speeds are improved.

Results of circulation enhancement concepts at low wind speed (attached flow) conditions show that a Coanda jet at the trailing edge of the rotor blade is effective at increasing circulation resulting in an increase of lift and the chordwise thrust force. This leads to an increased amount of net power generation compared to the baseline configuration for moderate blowing coefficients. At high wind speed leading edge separation occurs and the trailing edge blowing becomes ineffective in increasing the power output.

The effects of jet slot height, pulsed blowing jet, and leading edge blowing have also been investigated in this study. Results show that, at fixed momentum coefficient, a thin jet requires a lower mass flow rate than a thick jet to get almost the same efficiency, although the power requirement for producing a thin jet is higher. A pulsed jet uses less mass flow rate to achieve same performance as a steady jet. However, the pulsed jet requires a higher input power, or a lower net useable power compared to the steady jet. Results of leading edge blowing indicate that a leading edge blowing jet is found to be beneficial in increasing the power generation at high wind speeds.

A passive Gurney flap is found to increase the bound circulation and produce increased power in a manner similar to the Coanda jet. At low wind speeds, a Gurney flap can produce a net increase in generated power compared to the baseline rotor. At high wind speeds where the flow is separated, Gurney flap becomes ineffective in increasing

the power output. Gurney flap angle has significant influence in power generation. Higher power output is obtained at higher flap angles.

CHAPTER 1

INTRODUCTION

1.1 Background of Wind Energy

Human beings have been utilizing wind energy for at least two thousand years. The first windmills on record were built by the Persians in circa 900 AD. Windmills in their early form were primarily used for grinding grain and pumping water. During the nineteenth century, new designs of wind mills for pumping water evolved and were used for agriculture. At the beginning of the twentieth century, electricity came into use and windmills further evolved. These were called wind turbines and were connected to an electric generator. These designs could produce power only at low rates and the energy was stored in batteries. Though there was a continued interest in the use of wind turbines to produce electricity during the early twentieth-century, the evolution of diesel generators and stream turbines eventually took over the production of electricity. The use of windmills declined generally during the later part of 20^{th} century.

However, with the oil crisis in 1973, wind turbines became attractive again for many countries including the United States because of the desire to be less dependent on oil imports. National research programs were initiated around the world to investigate the possibilities of using wind energy and other renewable energy sources. An increasing concern for the environment also promoted interest in the use of wind energy. Over the past thirty years, large-scale generation of electricity by wind power has grown into an important industry. It has been estimated that the total energy output from wind resources has been increasing by approximately 20% a year. The rapid increase in the size and

capacity of commercial wind turbines between the years 1980 and 2003 is illustrated in Figure 1.1.

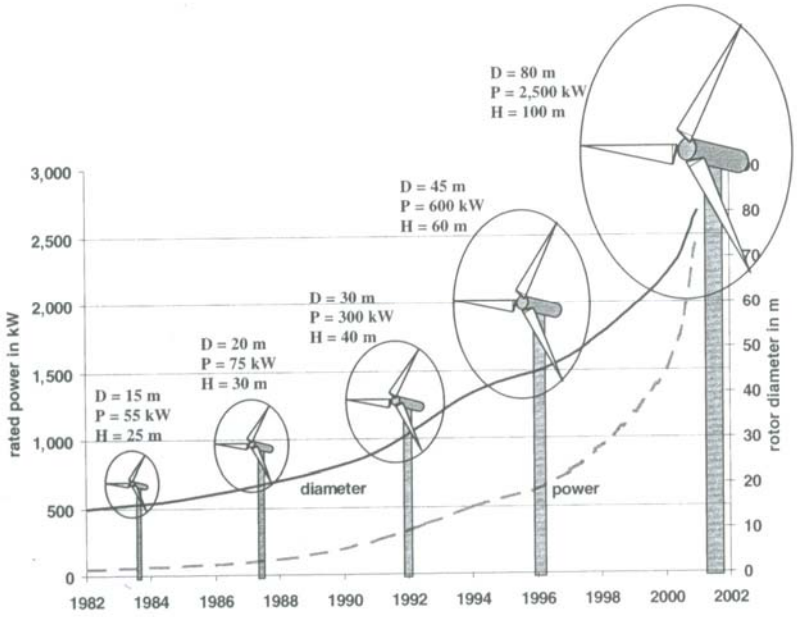

Figure 1.1 Size and power increase of commercial wind turbines over time (from Ref. [1])

The power production from a wind turbine is proportional to the rotor disk area, and varies as (wind speed)^3. A doubling of the rotor thus diameter leads to a four-time increase in power output. The influence of the wind speed is even more pronounced, with a doubling of wind speed leading to an eight-time increase in power. There have been considerable efforts to ensure that wind farms are developed in areas of the highest wind speeds and the turbines are optimally located. In some areas, very high towers are being used to take advantage of the increase of wind speed at high altitudes, in the outer edges of the atmospheric boundary layer.

Why use wind power? A country or region whose energy production is based on imported coal or oil can become more self-sufficient by using alternate sources such as

wind and solar power. Moreover, the growth in the global economy, particularly in Asia has spurred demand for energy (specifically electricity). The environmental impacts of conventional forms of energy production using oil, gas, or coal become an issue and affect the quality of life. Electricity produced from the wind produces no CO_2 emissions and does not contribute to the greenhouse effect. Wind energy is relatively labor-intensive, rather than land-intensive, and thus creates many jobs. Wind energy, however, also have some drawbacks. When operating, wind turbines create a certain level of noise. Noise is an important issue, especially in densely populated areas. Noise and visual impact, in the future, will be less important as more wind turbines will be sited off-shore. Another drawback is that wind energy can only be produced when nature allows the wind to blow. This problem can be addressed in part by knowing in advance what resources will be available in the near future, leading to a hybrid system that uses a combination of conventional power plants and renewable energy resources.

The reader interested in a fuller review of the history of wind energy development is referred to Ref. [2]-[5].

1.2 Short Description of Modern Wind Turbine

A wind turbine is device for extracting kinetic energy from the wind. The wind blows through the turbine and turns the blades, converting the kinetic energy of the wind into mechanical torque. This torque can be converted to produce useful work, usually in the form of electric power. All modern electricity-generating wind turbines use the lift force derived from the blade to drive the rotor. If the blades are connected to a vertical shaft, the turbine is called a vertical axis wind turbine (VAWT), and if the shaft is

horizontal, the turbine is called a horizontal axis wind turbine (HAWT). Most commercial wind turbines are the HAWTs.

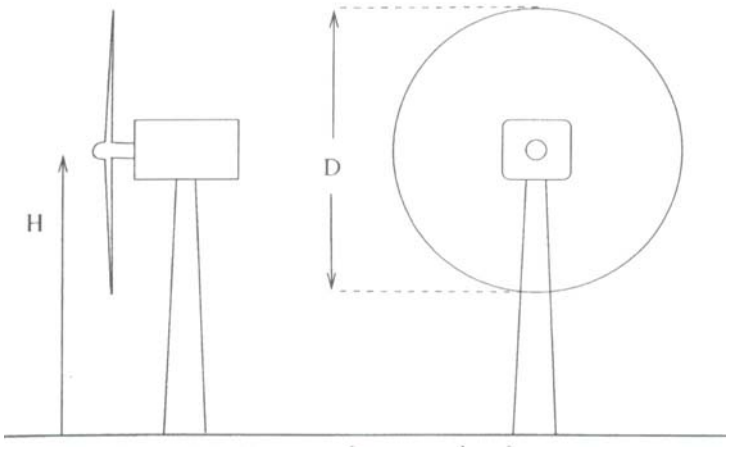

Figure 1.2 Sketch of Horizontal Axis Wind Turbine (from Ref. [6])

A HAWT, as sketched in Figure 1.2, is described in terms of the rotor diameter, the number of blades, the tower height, the rated power and the control system. The tower height is important since the wind speed increases with the height above the ground. The rotor diameter is also important since this determines the area used for extracting the available power from the wind. The ratio between the rotor diameter and the hub height is often approximately 1. The rated power is the maximum power allowed for the installed generator, and the control system must ensure that this power is not exceeded in high winds.

The number of blades is often two or three. Two-bladed wind turbines are cheaper since they have one blade fewer, but they are rotate faster and appear more flickering to the eyes, whereas three-bladed wind turbines seem calmer and therefore less disturbing in a landscape. The aerodynamic efficiency is lower on a two-bladed than on a three-bladed

wind turbines. A high rotational speed of the rotor is desirable in order to reduce the gearbox ratio required and this leads to low solidity rotors.

1.3 Wind Turbine under Yawed Flow Condition

Ideally, to extract maximum power from the wind, a wind turbine rotor should always operate with the wind direction perpendicular to its plane of rotation. However, this is seldom achieved in practice. The rotor axis of a wind turbine rotor is usually not aligned with the wind because the wind keeps changing its direction continuously, and the rotor yaw control system is usually not capable of following this variability and so spends most of its time in a yawed flow condition.

Even if the rotor is operating in a steady wind, if the rotor is misaligned the angle of attack on each blade will change azimuthally as the turbine rotates leading to fluctuating loads on the rotor blades. This can lead to fatigue damage. The changes in angle of attack may also cause undesirable moments about the yaw axis and the tilt axis due to the unbalanced blade forces.

In the yawed flow condition, yaw misalignment to the wind flow produces a velocity component parallel to the plane of rotation of the turbine disk, which leads to unsteady aerodynamic forces and also results in a skewed wake. The skewed wake causes unsteady, spatially non-uniform inflow through the rotor. The induced velocity varies both azimuthally and radially which makes the aerodynamics of the wind turbine even more complicated for yawed flow than for axial flow conditions. Under certain conditions, blade-vortex interactions can occur. These factors may lead to flow separation, inflow gradient across the rotor disk, and dynamic stall.

Although the physics behind these phenomena has been studied extensively [7]-[10], attempts at modeling these effects have been limited due to the computational complexity. Some recent noteworthy efforts in modeling HAWTs under yawed flow conditions may be found in Ref. [9] and [10].

During the past several years, a research effort has been underway at Georgia Tech under the National Renewable Energy Laboratory (NREL) support. This effort is aimed at first-principles based modeling of horizontal axis wind turbines (HAWT). As part of this effort, a three-dimensional hybrid methodology that combines the desired features of Navier-Stokes equations and wake models has been developed. This hybrid method, and a companion full Navier-Stokes solver, have been extensively applied to the performance of the NREL Phase VI rotor, under axial and yawed flow conditions [7]-[14]. Full Navier-Stokes simulations of HAWT configurations have been done using an overset grid approach by Duque et al. [15] . Incompressible multi-block Navier-Stokes analyses have been used by Sørensen and Hansen [16], and by Sørensen and Michelsen [17]. Sørensen et al. [18] have reported excellent Navier-Stokes simulations for the NREL Phase VI rotor tested at the NASA Ames Research Center. The effect of transition and turbulence models on the Navier-Stokes predictions has been studied by Xu and Sankar [7],[12], Benjanirat et al. [8], and by Shaw et al. [19].

1.4 Circulation Control Technology

Circulation control wing (CCW) technology is known as beneficial in increasing the bound circulation and hence the sectional lift coefficient of airfoil. This technology has been extensively investigated both experimentally [20]-[23] and numerically [24]-[30] over many years. Circulation control is implemented by tangentially blowing a small

high-velocity jet over a highly curved surface, such as a rounded trailing edge. This causes the boundary layer and the jet sheet to remain attached along the curved surface due to the Coanda effect (a balance of the pressure and centrifugal forces) and causing the jet to turn without separation [31]. The rear stagnation point location moves toward the lower airfoil surface, producing additional increase in circulation around the entire airfoil. The outer irrotational flow is also turned substantially, leading to high value of lift coefficient comparable to that achievable from conventional high lift systems. A typical CCW airfoil is shown in Figure 1.3.

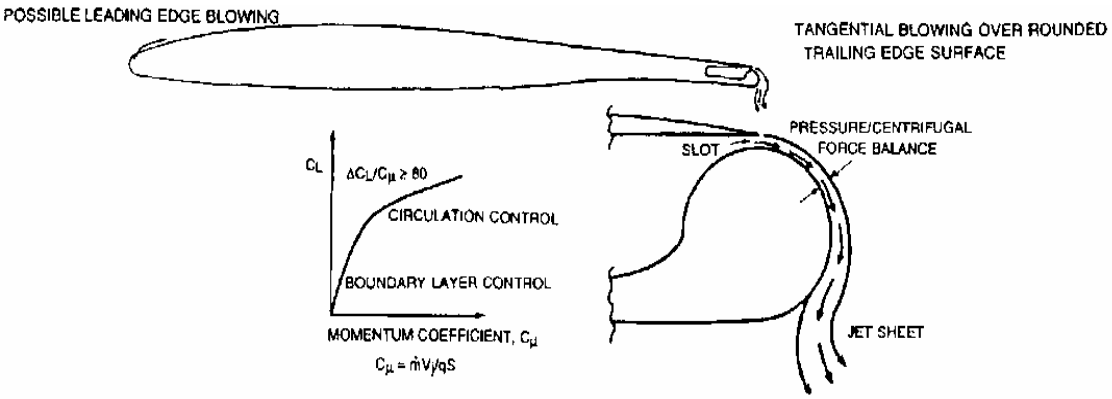

Figure 1.3 Basics of circulation control aerodynamics [from Ref.[21]]

Early CCW designs typically had a large-radius rounded trailing edge to maximize the lift benefit. These designs, however, also result in high drag penalty when the jet is turned off [20]. One way to reduce this drag is to make the lower surface of the trailing edge a flat surface, while keeping the upper surface highly curved [20],[23]. This curvature on the upper surface produces a large jet turning angle, leading to high lift.

The ability of circulation control technology to produce large values of lift may be advantageous for wind turbine design for the following reasons. Recall that wind turbines

generate power as a result of induced thrust forces generated by a forward rotation of the lift vector. Thus, any increase in the magnitude of the lift force (while keeping drag small, and L/D high) will immediately contribute to a corresponding increase in induced thrust and torque.

While circulation control technology has the potential for increased power generation, power is consumed in the generation of the jet. There should be a net positive increase in power generated for this concept to be attractive. The weight and the manufacturing cost of the ducts supplying high pressure air, and the logistics of delivering the air to the slots must all be addressed. Finally, circulation control technology aims at keeping the flow attached over the trailing edge, and will not be effective if the flow over the airfoil separates at the leading edge unless secondary Coanda jets are used at the leading edge as well. A systematic study is thus needed to fully evaluate the benefits of circulation control technology for wind turbines. In this work, the present author only address the aerodynamic aspects of this problem, although a crude estimate has been made to take into account the power consumed in generating the Coanda jet.

1.5 Gurney Flap

Another technique of increasing the lift coefficient of airfoils is the use of passive devices known as Gurney flap. The Gurney flap, first introduced by Lieback [32], is a small tab attached perpendicular to the lower surface of the airfoil in the vicinity of the trailing edge, with a height that can vary from 1% to 5% of the airfoil chord. The original Gurney flap was installed at the trailing edge of a rectangular race car wing. Race car testing by Dan Gurney demonstrated improved downforce with the flap.

Lieback's results showed a significant increment in lift compared to the baseline airfoil. In general, the drag of the airfoil increases with the addition of the Gurney flap, but often the percentage increase in lift is greater, resulting in an increased lift-to-drag ratio and therefore a better efficiency and performance. Lieback suggested that the optimal Gurney flap height should be on the order of 1-2 percent of the airfoil chord.

The increase in lift comes primarily from the effective increased camber on the lower surface without adversely disturbing the upper surface flow. Lieback hypothesized that a flow structure downstream of a Gurney flap has dual recirculation regions as shown in Figure 1.4. His wind tunnel studies indicated turning of the flow over the back of the flap and reverse flow directly behind it. An interesting feature of the hypothesized flow is the significant turning of the upper-surface trailing-edge flow, in terms of producing both increased lift due to turning and reduced form drag due to the longer region of attached flow near the trailing edge. Water tunnel dye flow experiments [33] and numerical studies [34] have support his hypothesis.

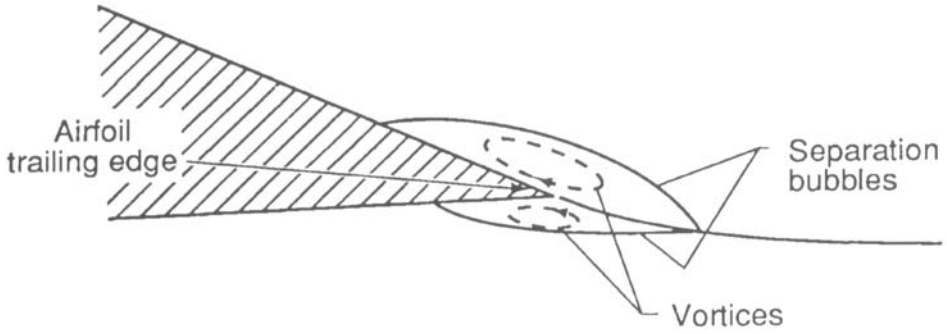

(a) Conventional airfoil at moderate C_L

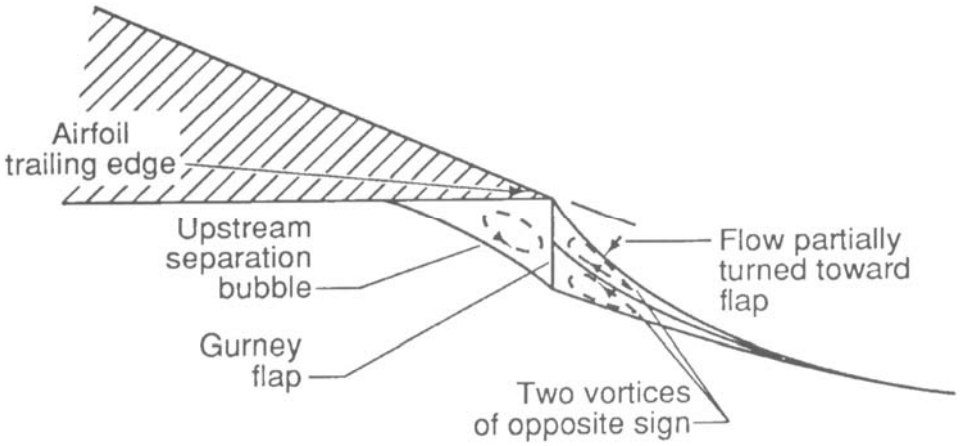

(b) Hypothesized flow near Gurney flap

Figure 1.4 Trailing edge flow fields [from Ref.[32]]

Due to its simple geometry, construction of the Gurney flap is simple, weight is low, and implementation with the flap system is easily accomplished.

Gurney flap has been extensively investigated [34]-[40] and used in many applications, e.g., alleviation of airfoil static and dynamic stall [41]-[43], flutter control [44]-[46], and rotor blade load control [47]-[49]. In those applications, the Gurney flap

has been found to enhance lift generation. The drag penalty varies depending on the airfoils used, flow conditions, and the Gurney flap configurations.

1.6 NREL Phase VI Rotor

Over the past several years, NREL has built and extensively tested a number of horizontal axis wind turbines under their Combined Experiment Rotor (CER) program [50]-[52]. Table 1.1 provides a brief summary of some of wind turbine rotors previously developed by NREL.

Table 1.1 Previous NREL rotors

	Phase II	**Phase III**	**Phase IV**	**Phase V**
Data collection dates	4/25/89–7/25/92	4/7/95–6/6/95	4/3/96–5/18/96 and 4/29/97–5/7/97	4/3/96–5/18/96 and 4/29/97–5/7/97
Blades / hub	untwisted / rigid	twisted / rigid	twisted / rigid	twisted / teeter
Number of blades	3	3	3	2

All of these tests were done in the field. While these tests provided useful data (e.g. power vs. wind speed) that could be used to validate aerodynamic analyses ([12], [53]-[56]), only the time-averaged data could be extracted. There was uncertainty associated with the wind speed and direction. Also, sectional data (surface pressures, normal and tangential forces) were not readily available for code validation.

In the present work a first-principles based flow solver has been applied to simulate the aerodynamics of the Phase VI rotor tested by the National Renewable Energy Laboratory at the 80ft × 120ft wind tunnel facility at NASA Ames Research Center. The NREL Phase VI rotor was designed by Giguère and Selig [57] under contract from NREL during March 1998 – March 1999. The Phase VI rotor geometry is based on the S809 airfoil, and more details about the blade can be found in Ref. [57]. A

comprehensive set of data that includes surface pressures, integrated normal and tangential forces, torque, root flap moment, and inflow were measured for a number of wind speeds and yaw angles [58].

The NREL Phase VI rotor is a stall-regulated rotor, in contrast to most modern designs that are pitch controlled machines. The rotor consists of two blades with a rotor diameter of 10.058 m. The blade flap or coning angle is either 0° for the upwind configurations or 3.4° for the downwind configurations. The S809 airfoil is used except in the root and hub region where the blade profile is modified to provide mechanical links. The blade geometry of Phase VI rotor and basic information of the machine are shown in Figure 1.5 and Table 1.2, respectively.

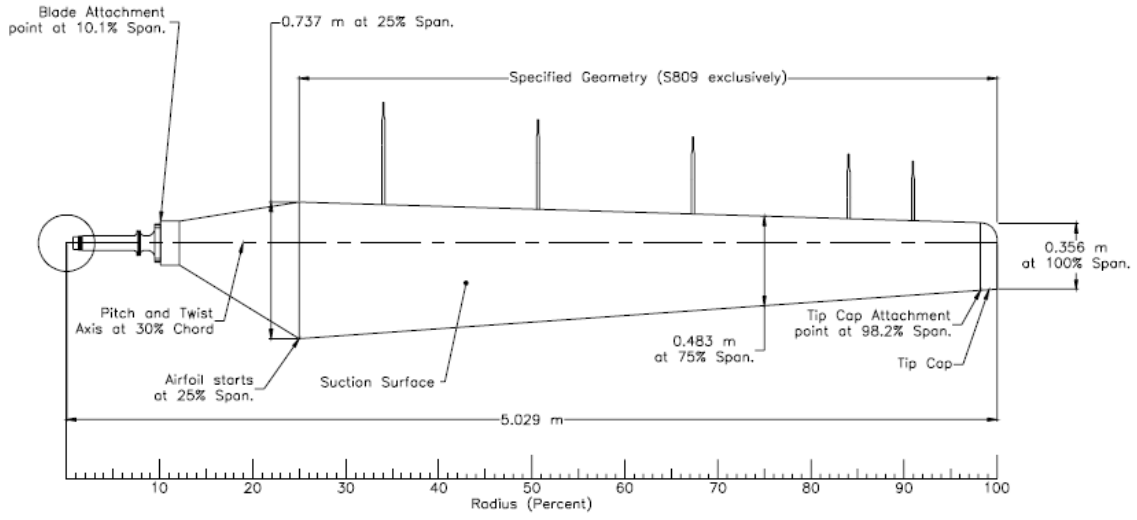

Figure 1.5 Blade planform dimensions [from Ref. [58]]

Table 1.2 Basic information of NREL Phase VI rotor

Number of Blades	2
Rotor Diameter	10.058m
Hub height	12.192m
Type of rotor	Teetered/Rigid
Rotational Speed	71.63 RPM
Power Regulation	Stall
Rated Power	19.8kW
Location of rotor	Upwind/Downwind
Rotational Direction	CCW (viewed from upwind)

The distribution of the non-linear twist angle is shown in Figure 1.6; with the reference zero pitch angle at 75% span.

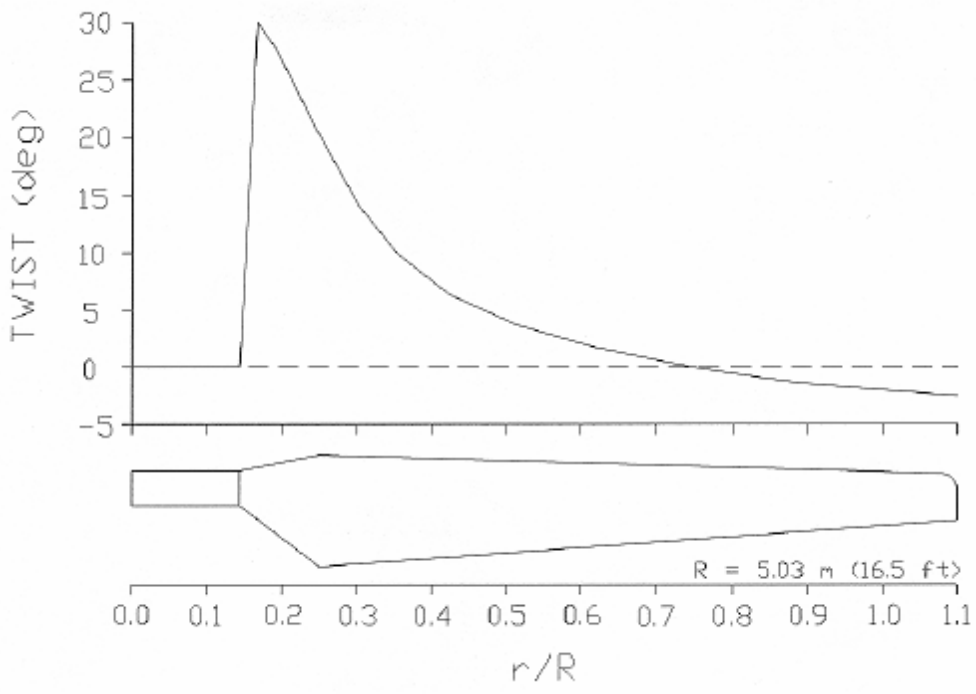

Figure 1.6 Twist angle distribution on the Phase VI rotor [from Ref. [57]]

The S809 airfoil used this rotor is designed by Airfoil, Inc. [59]. More details on this airfoil can be found in the work by Somers [60].

The blade surface pressure distribution was measured with a series of pressure taps on several spanwise stations as shown in Figure 1.7. Twenty-two pressure taps were installed at five primary spanwise stations: 30%, 46.6%, 63.3%, 80%, and 95%. There are also several pairs of pressure taps installed at 4% and 34% chord at other spanwise stations.

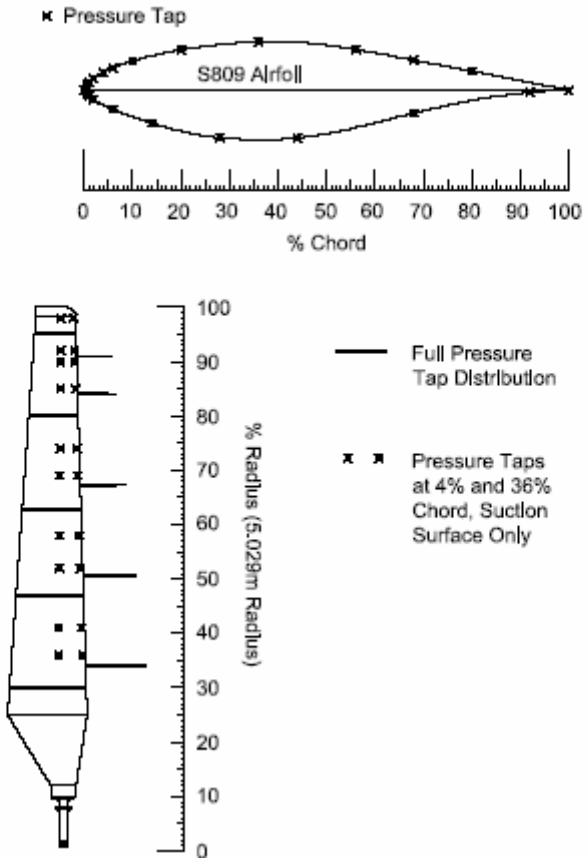

Figure 1.7 Pressure tap and five-hole probe locations [from Ref. [58]]

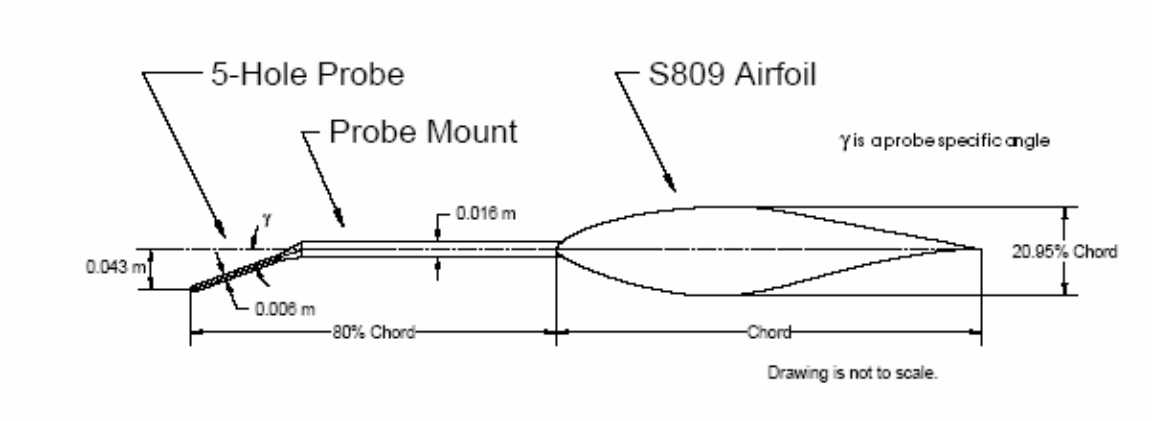

Figure 1.8 Blade-mounted five-hole probe [from Ref. [58]]

The upstream dynamic pressure and the angle of attack are measured by the five-hole probes as shown in Figure 1.8. The probes are installed at 34%, 51%, 67%, 84%, and 91% of span. The probe tip is located upstream about 80% of the chord and about 20 degrees below the chord line. The dynamic pressure was used in the calculation of the pressure and force coefficients, in the experiments.

1.7 Aerodynamic Force Coefficients

The present approach solves the viscous flow equations to compute the flow properties as a function of time in the entire region surrounding the rotor disk. Of particular interest is the surface pressure distribution which may be integrated to compute instantaneous (and time averaged) values of force coefficient C_N normal to the chord line and the force coefficient C_T tangential to the chord line, along the entire span of the blade. The represent the forces acting perpendicular and parallel to the airfoil chord, respectively. Other aerodynamic loads, such as torque, thrust and root flap moment, were computed using the C_N and C_T values in conjunction with their reference angles. The aerodynamic force coefficients are illustrated in Figure 1.9.

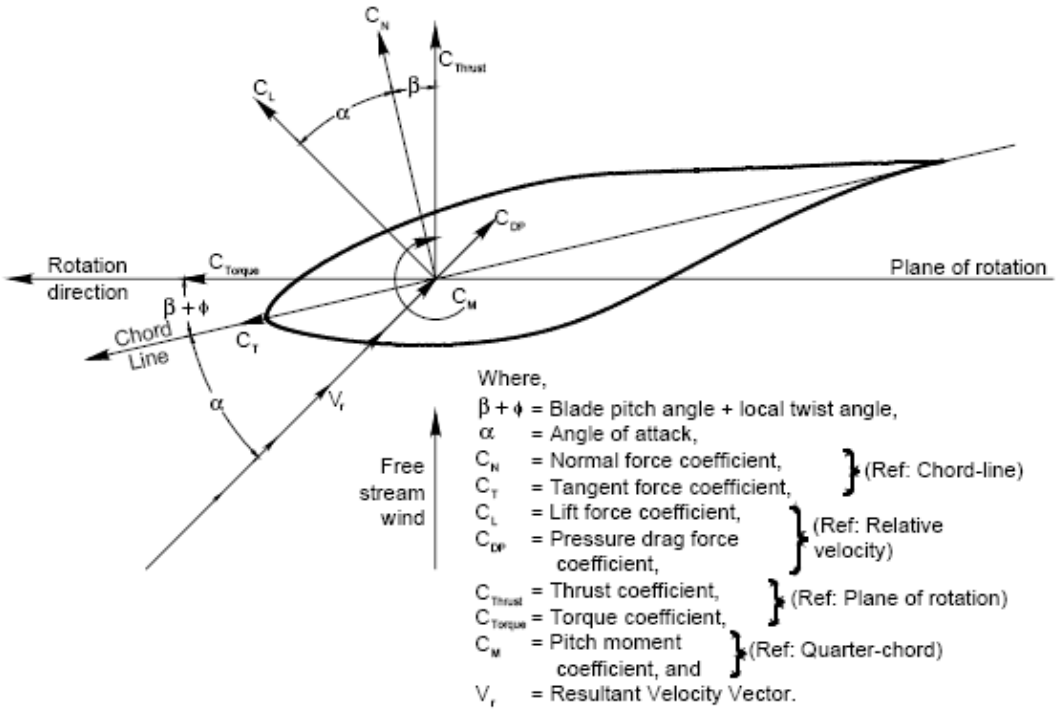

Figure 1.9 Aerodynamic force coefficient conventions [from Ref.[58]]

1.8 Research Objectives and Scope

With the advantage of modern high speed computers, there has been an increased interest in the use of first-principles based computational approaches for the aerodynamic modeling of HAWT. Since these approaches are based on the laws of conservation (mass, momentum, and energy), they can capture much of the physics in great detail. These approaches are particularly helpful at high wind speeds, where appreciable regions of separation are present and the flow is unsteady. The ability to accurately model the airloads can greatly aid the designers in tailoring the aerodynamic and aeroelastic features of the configuration. An improved understanding of the unsteady load environment will also help wind turbine engineers to efficiently design the rotor structure to meet the

fatigue life requirements. First-principles based analyses are also valuable for developing active means (e.g., circulation control), and passive means (e.g., Gurney flap) of reducing unsteady blade loads, mitigating stall, and for efficient capture of wind energy leading to more electrical power generation.

The primary objectives of the present research effort are to:

- Improve and validate an existing first-principles based hybrid solver for accurately simulating the aerodynamics of HAWT under yaw conditions.
- Examine the physics of the flow field and determine what further efforts are needed to improve the existing solver and turbulence models, to simulate all the physical phenomena that significantly affect the aerodynamics of HAWT.
- Numerically investigate the aerodynamics and benefit of circulation control technology (Coanda jet at the leading and trailing edge) and Gurney flap to HAWT under axial and yawed flow conditions.
- Determine what modifications to circulation control technique are needed, to achieve a more efficient system, hereby optimizing the power output while limiting the power consumption.

It should be noted that a full engineering study of the use of active and passive concepts will require a careful evaluation of issues such as feasibility, cost, weight, and ease of manufacturing. This work is limited only to the aerodynamic aspects of these concepts.

CHAPTER 2

MATHEMATICAL AND NUMERICAL FORMULATION

In this chapter, the formulation for the viscous flow solver used in this present study is presented. The governing equations (Navier-Stokes equations), the numerical discretization, and boundary conditions are documented. The methodology given below has been developed and used in many fixed wing, rotorcraft and wind turbine studies by Sankar and his co-workers [27],[61]-[65].

Section 2.1 describes the governing equations for the three-dimensional unsteady compressible flow in Cartesian coordinates and Generalized coordinates. The numerical formulation (temporal and spatial discretization) and the time marching scheme used to solve the governing equations are given in section 2.2. Turbulence models and transition model used in the present study are discussed in section 2.3 and 2.4, respectively. Finally initial conditions, boundary conditions, tip and root vortices modeling, and jet slot boundary condition are all described in section 2.5.

2.1 Mathematical Formulation

The Navier-Stokes equations are a set of partial differential equations describing the conversation of mass, momentum, and energy. It is known that all the properties of a continuum flow system for a viscous fluid are approximated by the Navier-Stokes equations. The fluid is assumed to be Newtonian, which is air in this study. These equations are based on Stokes relations and assume that the normal and shear stresses are linear functions of the strain rate, and that the thermodynamic pressure is equal to the

negative of one-third the sum of normal stresses. In the present study, body forces, heat addition, and mass diffusion effects are all neglected.

For most fluid flow problems, especially those involving complex geometry such as horizontal axis wind turbines, the flow will experience effects of turbulence. Since a direct numerical simulation of turbulent flow is very costly, it is impractical to directly capture all turbulent length and time scales for such a flow. Therefore, the Reynolds averaged Navier-Stokes equations (RANS) are used in this study, where all fluctuating quantities such as velocity are captured in a time averaged manner - averaged over the eddy turnover time scales, while retaining the longer time scales associated with the unsteady flow. The effect of turbulence is modeled using a semi-empirical turbulence model.

2.1.1 Governing Equations in Cartesian Coordinates

For a deforming or moving control volume, the differential form of Navier-Stokes equations, without external body forces, no heat addition, and mass diffusion, may be written as:

$$\frac{\partial q}{\partial t}+\frac{\partial F}{\partial x}+\frac{\partial G}{\partial y}+\frac{\partial H}{\partial z}=\frac{\partial R}{\partial x}+\frac{\partial S}{\partial y}+\frac{\partial T}{\partial y} \tag{2.1}$$

Here q is the vector of unknown given by:

$$q=\begin{Bmatrix}\rho\\ \rho u\\ \rho v\\ \rho w\\ e\end{Bmatrix} \tag{2.2}$$

where ρ is fluid density, *u*,*v*,*w* are fluid velocity components in three Cartesian directions, and *e* is the total energy per unit volume (the sum of internal energy and kinetic energy per unit volume) defined by

$$e = \frac{p}{\gamma - 1} + \frac{1}{2}\rho(u^2 + v^2 + w^2) \tag{2.3}$$

Also, *p* is the static pressure and γ is the specific heat ratio of the fluid.

The inviscid flux terms shown in equation (2.1) are given by

$$F = \begin{Bmatrix} \rho \\ \rho u^2 + p \\ \rho uv \\ \rho uw \\ u(e+p) \end{Bmatrix},\ G = \begin{Bmatrix} \rho \\ \rho uv \\ \rho v^2 + p \\ \rho vw \\ v(e+p) \end{Bmatrix}, H = \begin{Bmatrix} \rho \\ \rho uw \\ \rho vw \\ \rho w^2 + p \\ w(e+p) \end{Bmatrix} \tag{2.4}$$

The viscous flux vectors in equation (2.1) are defined as:

$$R = \begin{Bmatrix} 0 \\ \tau_{xx} \\ \tau_{yx} \\ \tau_{zx} \\ E_x \end{Bmatrix},\quad S = \begin{Bmatrix} 0 \\ \tau_{xy} \\ \tau_{yy} \\ \tau_{zy} \\ E_y \end{Bmatrix},\quad T = \begin{Bmatrix} 0 \\ \tau_{xz} \\ \tau_{yz} \\ \tau_{zz} \\ E_z \end{Bmatrix} \tag{2.5}$$

where the stress terms are evaluated using Stokes' hypothesis in which the bulk viscosity λ is set equal to $-\frac{2}{3}\mu$:

$$
\begin{aligned}
\tau_{xx} &= (\lambda + 2\mu)u_x + \lambda v_y + \lambda w_z = \frac{2}{3}\mu(2u_x - v_y - w_z) \\
\tau_{xy} &= \mu(u_y + v_x) \\
\tau_{xz} &= \mu(u_z + w_x) \\
\tau_{yy} &= \lambda u_x + \mu(\lambda + 2\mu)v_y + \lambda w_z = \frac{2}{3}\mu(2v_y - u_x - w_z) \\
\tau_{yz} &= \mu(v_z + w_y) \\
\tau_{zz} &= \lambda u_x + \lambda v_y + (\lambda + 2\mu)w_z = \frac{2}{3}\mu(2w_z - u_x - v_y)
\end{aligned}
\tag{2.6}
$$

Using the Fourier's law to relate the heat transfer rates with the temperature gradient, and the equation of state, the viscous terms in the energy equation, E_x, E_y and E_z, may be written as:

$$
\begin{aligned}
E_x &= u\tau_{xx} + v\tau_{xy} + w\tau_{xz} + k\frac{\partial T}{\partial x} \\
E_y &= u\tau_{xy} + v\tau_{yy} + w\tau_{yz} + k\frac{\partial T}{\partial y} \\
E_z &= u\tau_{xz} + v\tau_{yz} + w\tau_{zz} + k\frac{\partial T}{\partial z}
\end{aligned}
\tag{2.7}
$$

where k is the thermal conductivity, related the molecular viscosity through:

$$
k = \frac{\mu C_p}{\mathrm{Pr}} = \frac{\mu\gamma R}{\mathrm{Pr}(\gamma - 1)} \tag{2.8}
$$

and Pr is the Prandtl number (≈ 0.72 for air).

For turbulent flow, the viscosity μ is replaced with the sum of the molecular viscosity and eddy viscosity, $\mu + \mu_T$, and the term $\frac{\mu}{\mathrm{Pr}}$ is replaced with the sum $\frac{\mu}{\mathrm{Pr}} + \frac{\mu_T}{\mathrm{Pr}_T}$, where Pr_T is the turbulent Prandtl number (≈ 0.80). Further details in the eddy viscosity models used in this study will be given in Section 2.3.

2.1.2 Non-dimensionalized Governing Equations

In numerical simulations, it is more convenient if the governing equations in non-dimensional form are used. All quantities in the Navier-Stokes equations should be normalized by their corresponding reference parameters. In this present work, the following reference parameters are used:

$L_{ref} = c_{75\%}$: Chord of the rotor blade at 75% radial station

$V_{ref} = a_\infty$: Freestream speed of sound

$\rho_{ref} = \rho_\infty$: Freestream density

$\mu_{ref} = \mu_\infty$: Freestream viscosity

$T_{ref} = T_\infty$: Freestream temperature

The non-dimensional flow variables are expressed as follows:

$$x^* = \frac{x}{L_{ref}} \qquad u^* = \frac{u}{a_\infty} \qquad t^* = \frac{t}{L_{ref}/a_\infty} \qquad \mu^* = \frac{\mu}{\mu_\infty}$$

$$y^* = \frac{y}{L_{ref}} \qquad v^* = \frac{v}{a_\infty} \qquad \rho^* = \frac{\rho}{\rho_\infty} \qquad T^* = \frac{T}{T_\infty}$$

$$z^* = \frac{z}{L_{ref}} \qquad w^* = \frac{w}{a_\infty} \qquad p^* = \frac{p}{\rho_\infty a_\infty^2} \qquad e^* = \frac{e}{\rho_\infty a_\infty^2}$$

where the asterisk denotes a dimensionless variable. When this non-dimensionalization procedure is applied to equation (2.1), a very similar equation with the non-dimensional state vector, inviscid and viscous fluxes is obtained.

$$\frac{\partial q^*}{\partial t^*} + \frac{\partial F^*}{\partial x^*} + \frac{\partial G^*}{\partial y^*} + \frac{\partial H^*}{\partial z^*} = \frac{M}{\mathrm{Re}}\left[\frac{\partial R^*}{\partial x^*} + \frac{\partial S^*}{\partial y^*} + \frac{\partial T^*}{\partial z^*}\right] \tag{2.9}$$

The difference between equations (2.1) and (2.9) is that there are the Reynolds number Re and Mach number M on the right hand side of equation (2.9). Using the tip

speed of the rotor, the Reynolds number and Mach number used in this study are defined as:

$$\mathrm{Re} = \frac{\rho_\infty \Omega R c_{75\%}}{\mu_\infty} \tag{2.10}$$

$$M = \frac{\Omega R}{a_\infty} \tag{2.11}$$

where Ω is the angular velocity of the rotor and R is the rotor radius.

In the analysis all the calculations were done using the non-dimensional form given above.

2.1.3 Governing Equations in Generalized Coordinates

For most engineering applications, solutions for the flow past arbitrary geometries and arbitrary motions are difficult to achieve using Cartesian coordinates. Therefore, a body-fitted coordinate system is used where the boundary surfaces in the physical domain are mapped onto planar surfaces in the computational domain. It is easy to apply boundary conditions on planar surfaces in a body-fitted grid.

The physical coordinate system (x, y, z, t) can be expressed in term of a generalized non-orthogonal curvilinear coordinate system (ξ, η, ζ, τ) as follows:

$$\begin{aligned} \tau &= \tau(t) \\ \xi &= \xi(x, y, z, t) \\ \eta &= \eta(x, y, z, t) \\ \zeta &= \zeta(x, y, z, t) \end{aligned} \tag{2.12}$$

This coordinate system is dependent on the grid topology. For the C-grid topology used in the present study, The symbols ξ, η, and ζ correspond to coordinate directions

along the chordwise, spanwise, and normal directions, respectively. The symbol τ represents the time in the transformed computational domain.

By applying the generalized transformation using the chain rule of differentiation to equation (2.1), the transformed non-dimensional governing equations in generalized curvilinear system can be expressed as:

$$\frac{\partial \hat{q}}{\partial \tau}+\frac{\partial \hat{F}}{\partial \xi}+\frac{\partial \hat{G}}{\partial \eta}+\frac{\partial \hat{H}}{\partial \zeta}=\frac{M}{\mathrm{Re}}\left[\frac{\partial \hat{R}}{\partial \xi}+\frac{\partial \hat{S}}{\partial \eta}+\frac{\partial \hat{T}}{\partial \zeta}\right] \tag{2.13}$$

in which the transformed vectors are related to their Cartesian counterparts through the metrics and Jacobians of the transformation. For details of the transformation, the reader is referred to Ref. [65].

In equation (2.13), the transformed conserved flow variable vector becomes

$$\hat{q}=\frac{q}{J}=\frac{1}{J}\begin{Bmatrix}\rho\\ \rho u\\ \rho v\\ \rho w\\ e\end{Bmatrix} \tag{2.14}$$

The transformed inviscid fluxes $\hat{F},\hat{G},\hat{H}$ and the transformed viscous fluxes $\hat{R},\hat{S},\hat{T}$ are related to their counterparts F,G,H and R,S,T as follows:

$$
\begin{aligned}
\hat{F} &= \frac{1}{J}(F\xi_x + G\xi_y + H\xi_z + q\xi_t) \\
\hat{G} &= \frac{1}{J}(F\eta_x + G\eta_y + H\eta_z + q\eta_t) \\
\hat{H} &= \frac{1}{J}(F\zeta_x + G\zeta_y + H\zeta_z + q\zeta_t) \\
\hat{R} &= \frac{1}{J}(R\xi_x + S\xi_y + T\xi_z) \\
\hat{S} &= \frac{1}{J}(R\eta_x + S\eta_y + T\eta_z) \\
\hat{T} &= \frac{1}{J}(R\zeta_x + S\zeta_y + T\zeta_z)
\end{aligned}
\tag{2.15}
$$

where J is the Jacobian of transformation defined by

$$
\begin{aligned}
J \equiv \frac{\partial(x,y,z)}{\partial(\xi,\eta,\zeta)} &\equiv \begin{vmatrix} x_\xi & y_\xi & z_\xi \\ x_\eta & y_\eta & z_\eta \\ x_\zeta & y_\zeta & z_\zeta \end{vmatrix} \\
&= \frac{1}{x_\xi(y_\eta z_\zeta - y_\zeta z_\eta) + x_\eta(y_\zeta z_\xi - y_\xi z_\zeta) + x_\zeta(y_\xi z_\eta - y_\eta z_\xi)}
\end{aligned}
\tag{2.16}
$$

Physically, the Jacobian is the ratio of the volume of a grid cell in the computational domain divided by its volume in the physical domain.

The quantities ξ_x, ξ_y, ξ_z, ξ_t etc. appearing in the equation (2.15) are called the metrics of transformation and are computed by:

$$
\begin{aligned}
&\xi_x = J(y_\eta z_\zeta - y_\zeta z_\eta) \qquad \eta_x = J(y_\zeta z_\xi - y_\xi z_\zeta) \qquad \zeta_x = J(y_\xi z_\eta - y_\eta z_\xi) \\
&\xi_y = J(x_\zeta z_\eta - x_\eta z_\zeta) \qquad \eta_y = J(x_\xi z_\zeta - x_\zeta z_\xi) \qquad \zeta_y = J(x_\eta z_\xi - x_\xi z_\eta) \\
&\xi_z = J(x_\eta y_\zeta - x_\zeta y_\eta) \qquad \eta_z = J(x_\zeta y_\xi - x_\xi y_\zeta) \qquad \zeta_z = J(x_\xi y_\eta - x_\eta y_\xi)
\end{aligned}
\tag{2.17}
$$

In numerical simulations, the contravariant velocities U, V, and W are defined in the generalized coordinates as:

$$
\begin{aligned}
U &= (u - x_\tau)\xi_x + (v - y_\tau)\xi_y + (w - z_\tau)\xi_z \\
&= \xi_t + u\xi_x + v\xi_y + w\xi_z \\
V &= (u - x_\tau)\eta_x + (v - y_\tau)\eta_y + (w - z_\tau)\eta_z \\
&= \eta_t + u\eta_x + v\eta_y + w\eta_z \\
W &= (u - x_\tau)\zeta_x + (v - y_\tau)\zeta_y + (w - z_\tau)\zeta_z \\
&= \zeta_t + u\zeta_x + v\zeta_y + w\zeta_z
\end{aligned}
\tag{2.18}
$$

where

$$
\begin{aligned}
\xi_t &= -x_\tau\xi_x - y_\tau\xi_y - z_\tau\xi_z \\
\eta_t &= -x_\tau\eta_x - y_\tau\eta_y - z_\tau\eta_z \\
\zeta_t &= -x_\tau\zeta_x - y_\tau\zeta_y - z_\tau\zeta_z
\end{aligned}
\tag{2.19}
$$

where x_τ, y_τ, and z_τ represent the velocity components of the grid in an inertial frame. For wind turbines, $x_\tau\vec{i} + y_\tau\vec{j} + z_\tau\vec{k} = \vec{\Omega}\times\vec{r}$. The contravariant velocities U, V, and W are in directions normal to the constant ξ, η, and ζ surfaces, respectively.

The transformed inviscid and viscous flux vectors in equation (2.15) can be rewritten as [66]:

$$
\hat{F} = \frac{1}{J}\begin{Bmatrix} \rho U \\ \rho uU + \xi_x p \\ \rho vU + \xi_y p \\ \rho wU + \xi_z p \\ (e+p)U - \xi_t p \end{Bmatrix} \quad
\hat{G} = \frac{1}{J}\begin{Bmatrix} \rho V \\ \rho uV + \eta_x p \\ \rho vV + \eta_y p \\ \rho wV + \eta_z p \\ (e+p)V - \eta_t p \end{Bmatrix} \quad
\hat{H} = \frac{1}{J}\begin{Bmatrix} \rho W \\ \rho uW + \zeta_x p \\ \rho vW + \zeta_y p \\ \rho wW + \zeta_z p \\ (e+p)W - \zeta_t p \end{Bmatrix}
\tag{2.20}
$$

$$\hat{R} = \frac{1}{J}\begin{Bmatrix} 0 \\ \xi_x\tau_{xx} + \xi_y\tau_{xy} + \xi_z\tau_{xz} \\ \xi_x\tau_{yx} + \xi_y\tau_{yy} + \xi_z\tau_{yz} \\ \xi_x\tau_{zx} + \xi_y\tau_{zy} + \xi_z\tau_{zz} \\ \xi_x E_x + \xi_y E_y + \xi_z E_z \end{Bmatrix} \quad \hat{S} = \frac{1}{J}\begin{Bmatrix} 0 \\ \eta_x\tau_{xx} + \eta_y\tau_{xy} + \eta_z\tau_{xz} \\ \eta_x\tau_{yx} + \eta_y\tau_{yy} + \eta_z\tau_{yz} \\ \eta_x\tau_{zx} + \eta_y\tau_{zy} + \eta_z\tau_{zz} \\ \eta_x E_x + \eta_y E_y + \eta_z E_z \end{Bmatrix}$$

$$\hat{T} = \frac{1}{J}\begin{Bmatrix} 0 \\ \zeta_x\tau_{xx} + \zeta_y\tau_{xy} + \zeta_z\tau_{xz} \\ \zeta_x\tau_{yx} + \zeta_y\tau_{yy} + \zeta_z\tau_{yz} \\ \zeta_x\tau_{zx} + \zeta_y\tau_{zy} + \zeta_z\tau_{zz} \\ \zeta_x E_x + \zeta_y E_y + \zeta_z E_z \end{Bmatrix} \tag{2.21}$$

where the stresses terms and heat transfer terms in the transformed coordinates can now be written as follows:

$$\begin{aligned}
\tau_{xx} &= \frac{2}{3}\mu\left[2(u_\xi\xi_x + u_\eta\eta_x + u_\zeta\zeta_x) - (v_\xi\xi_y + v_\eta\eta_y + v_\zeta\zeta_y) - (w_\xi\xi_z + w_\eta\eta_z + w_\zeta\zeta_z)\right] \\
\tau_{yy} &= \frac{2}{3}\mu\left[2(v_\xi\xi_y + v_\eta\eta_y + v_\zeta\zeta_y) - (u_\xi\xi_x + u_\eta\eta_x + u_\zeta\zeta_x) - (w_\xi\xi_z + w_\eta\eta_z + w_\zeta\zeta_z)\right] \\
\tau_{zz} &= \frac{2}{3}\mu\left[2(w_\xi\xi_z + w_\eta\eta_z + w_\zeta\zeta_z) - (u_\xi\xi_x + u_\eta\eta_x + u_\zeta\zeta_x) - (v_\xi\xi_y + v_\eta\eta_y + v_\zeta\zeta_y)\right] \\
\tau_{xy} &= \tau_{yx} = \mu(u_\xi\xi_y + u_\eta\eta_y + u_\zeta\zeta_y + v_\xi\xi_x + v_\eta\eta_x + v_\zeta\zeta_x) \\
\tau_{xz} &= \tau_{zx} = \mu(u_\xi\xi_z + u_\eta\eta_z + u_\zeta\zeta_z + w_\xi\xi_x + w_\eta\eta_x + w_\zeta\zeta_x) \\
\tau_{yz} &= \tau_{zy} = \mu(v_\xi\xi_z + v_\eta\eta_z + v_\zeta\zeta_z + w_\xi\xi_y + w_\eta\eta_y + w_\zeta\zeta_y)
\end{aligned} \tag{2.22}$$

$$\begin{aligned}
E_x &= u\tau_{xx} + v\tau_{xy} + w\tau_{xz} + \frac{\mu C_p}{\mathrm{Pr}}\left(\xi_x\frac{\partial T}{\partial\xi} + \eta_x\frac{\partial T}{\partial\eta} + \zeta_x\frac{\partial T}{\partial\zeta}\right) \\
E_y &= u\tau_{xy} + v\tau_{yy} + w\tau_{yz} + \frac{\mu C_p}{\mathrm{Pr}}\left(\xi_y\frac{\partial T}{\partial\xi} + \eta_y\frac{\partial T}{\partial\eta} + \zeta_y\frac{\partial T}{\partial\zeta}\right) \\
E_z &= u\tau_{xz} + v\tau_{yz} + w\tau_{zz} + \frac{\mu C_p}{\mathrm{Pr}}\left(\xi_z\frac{\partial T}{\partial\xi} + \eta_z\frac{\partial T}{\partial\eta} + \zeta_z\frac{\partial T}{\partial\zeta}\right)
\end{aligned} \tag{2.23}$$

The time derivative $\frac{\partial}{\partial\tau}$ in the computational domain is related to the time derivative in the physical domain $\frac{\partial}{\partial t}$ by:

$$\left.\frac{\partial}{\partial t}\right|_{x,y,z} = \left.\frac{\partial}{\partial \tau}\right|_{\xi,\eta,\zeta} + \xi_t \frac{\partial}{\partial \xi} + \eta_t \frac{\partial}{\partial \eta} + \zeta_t \frac{\partial}{\partial \zeta} \tag{2.24}$$

where ξ_t, η_t, and ζ_t are defined as shown in equation (2.23). As discussed in Ref. [67], if the body or the grid is not moving, $\frac{\partial}{\partial \tau} = \frac{\partial}{\partial t}$.

2.2 Numerical Formulation

The starting point for the numerical formulation is a semi-discrete finite difference approximation to equation (2.13) given by

$$\left(\frac{\partial \hat{q}}{\partial \tau}\right)_{i,j,k} + \frac{\hat{F}_{i+\frac{1}{2},j,k} - \hat{F}_{i-\frac{1}{2},j,k}}{\Delta\xi} + \frac{\hat{G}_{i,j+\frac{1}{2},k} - \hat{G}_{i,j-\frac{1}{2},k}}{\Delta\eta} + \frac{\hat{H}_{i,j,k+\frac{1}{2}} - \hat{H}_{i,j,k-\frac{1}{2}}}{\Delta\zeta} =$$
$$\frac{M}{\mathrm{Re}}\left(\frac{\hat{R}_{i+\frac{1}{2},j,k} - \hat{R}_{i-\frac{1}{2},j,k}}{\Delta\xi} + \frac{\hat{S}_{i,j+\frac{1}{2},k} - \hat{S}_{i,j-\frac{1}{2},k}}{\Delta\eta} + \frac{\hat{T}_{i,j,k+\frac{1}{2}} - \hat{T}_{i,j,k-\frac{1}{2}}}{\Delta\zeta} \right) \tag{2.25}$$

here,

$$\begin{aligned} \Delta\xi &= \xi_{i+\frac{1}{2},j,k} - \xi_{i-\frac{1}{2},j,k} = 1 \\ \Delta\eta &= \eta_{i,j+\frac{1}{2},k} - \eta_{i,j-\frac{1}{2},k} = 1 \\ \Delta\zeta &= \zeta_{i,j,k+\frac{1}{2}} - \zeta_{i,j,k-\frac{1}{2}} = 1 \end{aligned} \tag{2.26}$$

The central difference operator δ is now introduced such that:

$$\delta_\xi \hat{F}\Big|_{i,j,k} = \frac{\hat{F}_{i+\frac{1}{2},j,k} - \hat{F}_{i-\frac{1}{2},j,k}}{\Delta\xi}$$
$$\delta_\eta \hat{G}\Big|_{i,j,k} = \frac{\hat{G}_{i,j+\frac{1}{2},k} - \hat{G}_{i,j-\frac{1}{2},k}}{\Delta\eta} \tag{2.27}$$
$$\delta_\zeta \hat{H}\Big|_{i,j,k} = \frac{\hat{H}_{i,j,k+\frac{1}{2}} - \hat{H}_{i,j,k-\frac{1}{2}}}{\Delta\zeta}$$

For the viscous fluxes, $\delta_\xi \hat{R}\Big|_{i,j,k}, \delta_\eta \hat{S}\Big|_{i,j,k}, \delta_\zeta \hat{T}\Big|_{i,j,k}$ are also defined in a similar manner.

With this notation, the equation (2.25) then can be written as:

$$\frac{\partial \hat{q}}{\partial \tau} = -\left(\delta_\xi \hat{F} + \delta_\eta \hat{G} + \delta_\zeta \hat{H}\right) + \frac{M}{\mathrm{Re}}\left(\delta_\xi \hat{R} + \delta_\eta \hat{S} + \delta_\zeta \hat{T}\right) \tag{2.28}$$

Equation (2.28) is now an ODE in time for the flow properties *q*, that may advanced in time until a steady state solution (or a limit cycle periodic solution in time) is obtained.

2.2.1 Calculation of Inviscid Fluxes

The fluxes F, G, H represent fluxes of mass, momentum, and energy carried by acoustic, vortical, and entropy waves. While computing these terms, attention must be paid to the direction in which information is propagated. A simple averaging of properties [68] at the half points to compute fluxes does not take into consideration the wave propagation nature of the flow. To overcome this, a variety of flux-vector splitting [69]-[71], flux-difference splitting schemes [72]-[75] have been proposed that split the flux into contributions from the individual waves.

In the present work, Roe's approximate Riemann solver [74] is used. The flux $\hat{F}$ is computed as:

$$\hat{F}_{i+\frac{1}{2},j,k} = \frac{1}{2}\left\{(\hat{F}_L + \hat{F}_R) - \left|\tilde{A}\right|(q_R - q_L)\right\} \tag{2.29}$$

In equation (2.29), q_R and q_L may be considered as q at $(i+\frac{1}{2}, j, k)$ node just to the right and to the left sides of $(i \pm \frac{1}{2}$ or $j \pm \frac{1}{2}$ or $k \pm \frac{1}{2})$, respectively, and defined as:

$$q_L = \begin{bmatrix} \rho_L \\ u_L \\ v_L \\ w_L \\ p_L \end{bmatrix} \qquad q_R = \begin{bmatrix} \rho_R \\ u_R \\ v_R \\ w_R \\ p_R \end{bmatrix} \tag{2.30}$$

Notice that a primitive variable based form is used.

The quantities $\hat{F}_L$ and $\hat{F}_R$, the physical fluxes, are fluxes $\hat{F}$ evaluated at the half node $(i+\frac{1}{2}, j, k)$ using the flow properties from left and right of the cell face as shown in Figure 2.1.

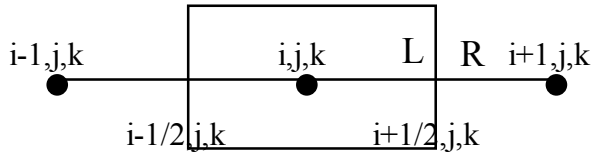

Figure 2.1 Nodes and half-node

The fluxes $\hat{F}_L$ and $\hat{F}_R$ can be evaluated as:

$$\hat{F}_L = \begin{bmatrix} \rho_L U_L \\ \rho_L U_L u_L + p_L n_x \\ \rho_L U_L v_L + p_L n_y \\ \rho_L U_L w_L + p_L n_z \\ \rho_L U_L h_{0L} - p_L n_t \end{bmatrix} \qquad \hat{F}_R = \begin{bmatrix} \rho_R U_R \\ \rho_R U_R u_R + p_R n_x \\ \rho_R U_R v_R + p_R n_y \\ \rho_R U_R w_R + p_R n_z \\ \rho_R U_R h_{0R} - p_R n_t \end{bmatrix} \tag{2.31}$$

Here, the quantities $U, h_0,$ and n_t are the contravaraint velocity, specific total enthalpy, and the grid velocity of the coordinate surface $(i+\frac{1}{2}, j, k)$ in the normal direction of the surface, respectively. These terms are defined as:

$$
\begin{aligned}
U &= (\vec{V} - \vec{V}_G) \cdot \frac{\vec{\nabla}\xi}{J} \\
h_0 &= \frac{e+p}{\rho} \\
n_t &= -(\vec{V}_G \cdot \frac{\vec{\nabla}\xi}{J})
\end{aligned}
\tag{2.32}
$$

where $\vec{V}_G$ is the grid velocity at the cell face $(i+\frac{1}{2}, j, k)$ defined by $\vec{V}_G = x_\tau \vec{i} + y_\tau \vec{j} + z_\tau \vec{k}$. The fluxes at other half-points $(i, j+\frac{1}{2}, k)$ etc may similarly be defined.

The term $\left|\tilde{A}\right|(q_R - q_L)$ on the right hand side of equation (2.29) is referred to as a "numerical viscosity" or "diffusion term". The numerical viscosity term, calculated as a sum of simple wave contributions depending on their wave speeds, is needed to filter out high frequency non-physical oscillations in the solution. The term $\left|\tilde{A}\right| = \left|\partial \hat{F} / \partial \hat{q}\right|$, the flux Jacobian matrix, is evaluated using "Roe-averaged" flow properties from left and right of the cell face.

To simplify the numerical computations, the matrix elements of the numerical term $\left|\tilde{A}\right|(q_R - q_L)$ are computed by an approach presented by Vinokur and Liu [76]:

$$
\left|\tilde{A}\right|(q_R - q_L) = \left|\tilde{\lambda}_1\right| \begin{Bmatrix} \Delta\rho \\ \Delta\rho u \\ \Delta\rho v \\ \Delta\rho w \\ \Delta e \end{Bmatrix} + \delta_1 \begin{Bmatrix} \tilde{\rho} \\ \tilde{\rho}\tilde{u} \\ \tilde{\rho}\tilde{v} \\ \tilde{\rho}\tilde{w} \\ \tilde{\rho}\tilde{h}_0 \end{Bmatrix} + \delta_2 \begin{Bmatrix} 0 \\ n_x \\ n_y \\ n_z \\ \tilde{U}_c \end{Bmatrix}
\tag{2.33}
$$

where

$$
\begin{aligned}
\delta_1 &= C_1 \frac{\Delta p}{\tilde{\rho}\tilde{a}^2} + 0.5 C_2 \frac{\Delta U_c}{\tilde{a}} \\
\delta_2 &= C_1 \tilde{\rho} \Delta U_c + 0.5 C_2 \frac{\Delta p}{\tilde{a}} \\
C_1 &= -\left|\tilde{\lambda}_1\right| + 0.5\left(\left|\tilde{\lambda}_2\right| + \left|\tilde{\lambda}_3\right|\right) \\
C_2 &= \left|\tilde{\lambda}_2\right| - \left|\tilde{\lambda}_3\right|
\end{aligned}
\tag{2.34}
$$

Here the operator Δ is defined as jump across the cell face, i.e. $\Delta(\bullet) = (\bullet)\big|_R - (\bullet)\big|_L$. The characteristic wave speeds and the contravariant velocity are defined by

$$
\begin{aligned}
\tilde{\lambda}_1 &= \tilde{U} \\
\tilde{\lambda}_2 &= \tilde{U} + \tilde{a} \\
\tilde{\lambda}_3 &= \tilde{U} - \tilde{a} \\
\tilde{U} &= n_t + n_x \tilde{u} + n_y \tilde{v} + n_z \tilde{w} = (\vec{V} - \vec{V}_G) \cdot \vec{n} \\
\tilde{U}_c &= n_x \tilde{u} + n_y \tilde{v} + n_z \tilde{w} = \vec{V} \cdot \vec{n} \\
\Delta U_c &= U_c\big|_R - U_c\big|_L = n_x (u_R - u_L) + n_y (v_R - v_L) + n_z (w_R - w_L)
\end{aligned}
\tag{2.35}
$$

Again, $\vec{n} = n_x \vec{i} + n_y \vec{j} + n_z \vec{k} = \dfrac{\vec{\nabla}\xi}{J}$, is a unit normal vector to the surface $\xi =$ constant times a cell face area associated with the cell interface $(i + \frac{1}{2}, j, k)$, at which the flux is calculated. All the quantities with a tilde sign over represent the "Roe-averaged" quantities [77], which are given by:

$$
\begin{aligned}
R &= \sqrt{\rho_R / \rho_L} \\
\widetilde{\rho} &= \sqrt{\rho_R \rho_L} \\
\widetilde{u} &= u_L\left(\frac{1}{1+R}\right) + u_R\left(\frac{R}{1+R}\right) \\
\widetilde{v} &= v_L\left(\frac{1}{1+R}\right) + v_R\left(\frac{R}{1+R}\right) \\
\widetilde{w} &= w_L\left(\frac{1}{1+R}\right) + w_R\left(\frac{R}{1+R}\right) \\
\widetilde{e} &= e_L\left(\frac{1}{1+R}\right) + e_R\left(\frac{R}{1+R}\right) \\
\widetilde{a} &= \sqrt{\gamma(\gamma-1)\left[\frac{\widetilde{e}}{\widetilde{\rho}} - \frac{1}{2}(\widetilde{u}^2 + \widetilde{v}^2 + \widetilde{w}^2)\right]}
\end{aligned}
\tag{2.36}
$$

van Leer [78] showed that the accuracy of the evaluating primitive variables at the left and right of the cell face determines the spatial accuracy of the solution. For example, a first order accuracy in space can be achieved by using the simplest approach: $q_L = q_i$ and $q_R = q_{i+1}$.

In this present work, an interpolation method called the Monotone Upstream-centered Scheme for Conservation Laws (MUSCL) is used. In general, the MUSCL scheme [79] can be written as:

$$
\begin{aligned}
q_L &= \{1 + [(1-k)\nabla + (1+k)\Delta]/4\} q_i \\
q_R &= \{1 - [(1+k)\nabla + (1-k)\Delta]/4\} q_{i+1}
\end{aligned}
\tag{2.37}
$$

Here Δ and ∇ are the forward- and backward-difference operators, respectively, defined as:

$$
\Delta(\bullet)_i = (\bullet)_{i+1} - (\bullet)_i \quad , \quad \nabla(\bullet)_i = (\bullet)_i - (\bullet)_{i-1}
$$

The choice of k determines the spatial accuracy of the scheme. For example, $k = -1$ yields second-order fully upwind scheme, while $k = 1$ yields second-order central

difference scheme. In the present work, $k = \frac{1}{3}$ is chosen, and a third-order accurate upwind scheme is obtained. Equation (2.37) can be rewritten as:

$$q_L = q_i + \frac{1}{6}(q_i - q_{i-1}) + \frac{1}{3}(q_{i+1} - q_i)$$
$$q_R = q_{i+1} - \frac{1}{3}(q_{i+1} - q_i) - \frac{1}{6}(q_{i+2} - q_{i+1}) \tag{2.38}$$

Figure 2.2 shows the three-point stencils for computing left and right primitive variables in the third-order MUSCL scheme.

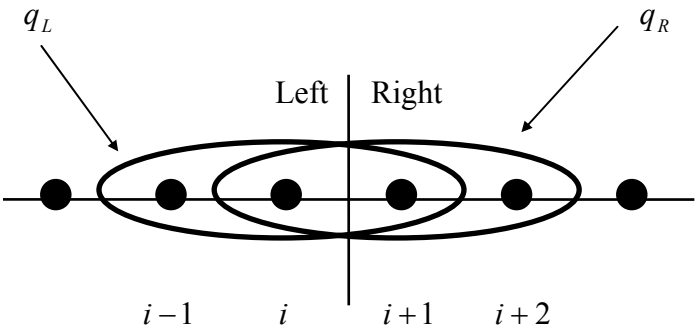

Figure 2.2 Three-point stencil

In regions with large flow gradients and discontinuities (e.g. shocks), the high-order scheme must be reduced to a lower order to maintain stability and to eliminate spurious numerical oscillations in the solution. This can be accomplished by using of a flux limiter. A limiter is a non-linear algorithm that reduces the high-derivative content of a subgrid interpolant in order to make it non-oscillatory. It yields the interface reconstructions which are within the bounds of the adjacent cell averages. By applying the flux limiter ϕ, equation (2.37) can be expressed generally as:

$$
\begin{aligned}
q_L &= \left\{1 + \phi^l[(1-k)\nabla + (1+k)\Delta]/4\right\} q_i \\
q_R &= \left\{1 - \phi^r[(1+k)\nabla + (1-k)\Delta]/4\right\} q_{i+1}
\end{aligned}
\tag{2.39}
$$

where ϕ^l and ϕ^r are designed such that they become zero in the vicinity of the high gradients.

In the present methodology, the modified van Albada flux limiter [80] is used, which is defined by:

$$
\begin{aligned}
\phi^l &= \frac{2(\nabla q_i)(\Delta q_i) + \varepsilon}{(\nabla q_i)^2 + (\Delta q_i)^2 + \varepsilon} \\
\phi^r &= \frac{2(\nabla q_{i+1})(\Delta q_{i+1}) + \varepsilon}{(\nabla q_{i+1})^2 + (\Delta q_{i+1})^2 + \varepsilon}
\end{aligned}
\tag{2.40}
$$

Also, ε is a small parameter that prevents indeterminacy in regions of zero gradients, i.e. where $(\nabla q_i) = (\Delta q_i) = 0$. This limiter has been reported and implemented in various forms in the literature, and has been shown to prevent spurious numerical oscillations and give better convergence [81]-[83].

2.2.2 Calculation of Viscous Fluxes

At each time step the viscous fluxes $(\hat{R}, \hat{S}, \hat{T})$ in equation (2.25) are computed and added to the inviscid flux contributions on the right hand side of the equation. Unlike the invisvid fluxes, these viscous fluxes are computed using a symmetric second order central difference scheme. As given earlier in equation (2.21-2.23), the viscous fluxes contain derivatives of the velocities, such as u_ξ, which can be computed as:

$$
u_\xi\Big|_{i+\frac{1}{2},j,k} = \frac{u_{i+1,j,k} - u_{i,j,k}}{\Delta\xi} \qquad u_\xi\Big|_{i-\frac{1}{2},j,k} = \frac{u_{i,j,k} - u_{i-1,j,k}}{\Delta\xi} \tag{2.41}
$$

and the metrics needed at the half point can be directly calculated.

As stated earlier, for turbulent flow, the viscosity μ in the equations (2.22) and (2.23) is augmented by the eddy viscosity μ_T. Further details in the eddy viscosity models used in this study will be given in Section 2.3.

2.2.3 Time Marching Scheme

Since the governing equations are parabolic in time, a stable dissipative time marching scheme is needed to advance the solution. In this study, the following semi-implicit scheme is used to achieve second order accuracy in time.

$$\left.\frac{\partial \hat{q}}{\partial \tau}\right|^{n+1} = -(\delta_\xi \hat{F} + \delta_\eta \hat{G} + \delta_\zeta \hat{H})\Big|^{n+1} + \frac{M}{\mathrm{Re}}(\delta_\xi \hat{R} + \delta_\eta \hat{S} + \delta_\zeta \hat{T})\Big|^{n} \tag{2.42}$$

where the superscripts refer to time step n and $n+1$. Here, δ_ξ, δ_η, δ_ζ are standard central difference operators. The inviscid fluxes and viscous fluxes are computed at the half-point $(i \pm \frac{1}{2}, j \pm \frac{1}{2}, k \pm \frac{1}{2})$ as discussed earlier.

The discretization of term $\dfrac{\partial \hat{q}}{\partial \tau}$ in equation (2.42) is given by:

$$\left.\frac{\partial \hat{q}}{\partial \tau}\right|^{n+1} = \frac{\hat{q}^{n+1} - \hat{q}^{n}}{\Delta \tau} + O(\Delta \tau) \tag{2.43}$$

As a result, equation (2.42) can be expressed as:

$$\hat{q}^{n+1} = \hat{q}^{n} - \Delta\tau(\delta_\xi \hat{F}^{n+1} + \delta_\eta \hat{G}^{n+1} + \delta_\zeta \hat{H}^{n+1}) + \Delta\tau \frac{M}{\mathrm{Re}}(\delta_\xi \hat{R}^{n} + \delta_\eta \hat{S}^{n} + \delta_\zeta \hat{T}^{n}) \tag{2.44}$$

Equation (2.42) gives a system of non-linear algebraic equations. It is difficult to solve because the inviscid terms being handled implicitly. Therefore, to obtain a linear system of equations, the implicit inviscid terms must be linearized. A linearization procedure proposed by Beam and Warming [84] is utilized as follows:

$$\begin{aligned}
\hat{F}^{n+1} &= \hat{F}^{n} + [A^{n}](\hat{q}^{n+1} - \hat{q}^{n}) + O(\Delta\tau^{2}) \\
\hat{G}^{n+1} &= \hat{G}^{n} + [B^{n}](\hat{q}^{n+1} - \hat{q}^{n}) + O(\Delta\tau^{2}) \\
\hat{H}^{n+1} &= \hat{H}^{n} + [C^{n}](\hat{q}^{n+1} - \hat{q}^{n}) + O(\Delta\tau^{2})
\end{aligned} \tag{2.45}$$

where $[A^n]$, $[B^n]$ and $[C^n]$ are the 5x5 Jacobian matrices defined as:

$$[A] = \hat{A} = \frac{\partial \hat{F}}{\partial \hat{q}} \qquad [B] = \hat{B} = \frac{\partial \hat{G}}{\partial \hat{q}} \qquad [C] = \hat{C} = \frac{\partial \hat{H}}{\partial \hat{q}} \tag{2.46}$$

The viscous terms are treated explicitly, and no linearization is needed.

The Jacobian matrices can be evaluated analytically and are given by Pulliam and Chaussee [85]. The detailed forms of these matrices are shown below:

$$[A] = \begin{bmatrix}
\xi_t & \xi_x & \xi_y & \xi_z & 0 \\
\xi_x\phi^2 - u\theta & \Theta - \xi_x(\gamma-2)u & \xi_y u - \sigma\xi_x v & \xi_z u - \sigma\xi_x w & \xi_x\sigma \\
\xi_y\phi^2 - v\theta & \xi_x v - \sigma\xi_y u & \Theta - \xi_y(\gamma-2)v & \xi_z v - \sigma\xi_y w & \xi_y\sigma \\
\xi_z\phi^2 - w\theta & \xi_x w - \sigma\xi_z u & \xi_y w - \sigma\xi_z v & \Theta - \xi_z(\gamma-2)w & \xi_z\sigma \\
\theta(\phi^2 - E) & \xi_x E - \sigma u\theta & \xi_y E - \sigma v\theta & \xi_z E - \sigma w\theta & \xi_t + \sigma\theta
\end{bmatrix} \tag{2.47}$$

where

$$\begin{aligned}
\phi^2 &= (\gamma-1)(u^2 + v^2 + w^2)/2 \\
\theta &= \xi_x u + \xi_y v + \xi_z w \\
\sigma &= \gamma - 1 \\
\Theta &= \xi_t + \theta \\
E &= \frac{\gamma e}{\rho} - \phi^2
\end{aligned} \tag{2.48}$$

The matrices $[B]$ and $[C]$ can be similarly evaluated by using η and ζ in the above equations, respectively, instead of ξ.

After substituting equation (2.45) into equation (2.44) and arranging all of the known quantities at time step *n* to the right hand side, the following system of linear equations for $\Delta\hat{q}$ can be obtained,

$$[I + \Delta\tau(\delta_\xi \hat{A}^n + \delta_\eta \hat{B}^n + \delta_\zeta \hat{C}^n)]\Delta\hat{q}^{n+1} = [RHS]^n \tag{2.49}$$

where $\Delta\hat{q}^{n+1} = \hat{q}^{n+1} - \hat{q}^n$, I is the identity matrix. The term [*RHS*], referred as the residual, is given by:

$$[RHS]^n = -\Delta\tau(\delta_\xi \hat{F}^n + \delta_\eta \hat{G}^n + \delta_\zeta \hat{H}^n) + \Delta\tau \frac{M}{\mathrm{Re}}(\delta_\xi \hat{R}^n + \delta_\eta \hat{S}^n + \delta_\zeta \hat{T}^n) \tag{2.50}$$

In steady-state problems, the residual should be reduced to an acceptable small value for the calculation to be considered converged. In time dependent or unsteady problems, however, the residual does not need to reach a minimum value and may vary with time depending on the flow situation.

Equation (2.49) may be viewed as a matrix system

$$[M]\{\Delta\hat{q}\} = [RHS] \tag{2.51}$$

Solution of equation (2.49) is computationally expensive because the unfactored coefficient matrix [*M*], which is a seven-diagonal matrix, requires vast computer storage and computing time to invert. In order to reduce the computational work, this sparse matrix [*M*] is approximately factored into three sparse matrices using a Lower-Upper Symmetric Gauss-Seidel (LU-SGS) implicit scheme proposed by Yoon and Jameson [86],[87]. The LU-SGS method ensures that the matrix is diagonally dominant. Rieger and Jameson [88] extended the LU-SGS scheme to three dimensions. This scheme is widely used to solve the compressible Navier-Stokes equations.

In this method, equation (2.51) is first expressed as

$$(L + D + U)\Delta\hat{q}^{n+1} = [RHS]^n \tag{2.52}$$

where L is a lower block triangular matrix with null matrices on the diagonal, D is a block diagonal matrix formed out of both positive and negative flux Jacobian matrices, and U is an upper block triangular matrix with null matrices on the diagonal. For the case of non-singular matrix D, equation (2.50) may be written as:

$$D(D^{-1}L + I + D^{-1}U)\Delta\hat{q}^{n+1} = [RHS]^n \tag{2.53}$$

Using LU- factorization, equation (2.52) can be approximated as

$$D(I + D^{-1}L)(I + D^{-1}U)\Delta\hat{q}^{n+1} = [RHS]^n \tag{2.54}$$

or

$$(D + L)D^{-1}(D + U)\Delta\hat{q}^{n+1} = [RHS]^n \tag{2.55}$$

These matrices may be expressed as

$$\begin{aligned}
(D+L) &= I - \Delta\tau\left(\frac{\hat{A}^-}{\Delta\xi} - \delta_\xi^-\hat{A}^+ + \frac{\hat{B}^-}{\Delta\eta} - \delta_\eta^-\hat{B}^+ + \frac{\hat{C}^-}{\Delta\zeta} - \delta_\zeta^-\hat{C}^+\right) \\
D &= I + \frac{\Delta\tau}{\Delta\xi}\left(\hat{A}^+ - \hat{A}^-\right) + \frac{\Delta\tau}{\Delta\eta}\left(\hat{B}^+ - \hat{B}^-\right) + \frac{\Delta\tau}{\Delta\zeta}\left(\hat{C}^+ - \hat{C}^-\right) \\
(D+U) &= I + \Delta\tau\left(\frac{\hat{A}^+}{\Delta\xi} + \delta_\xi^+\hat{A}^- + \frac{\hat{B}^+}{\Delta\eta} + \delta_\eta^+\hat{B}^- + \frac{\hat{C}^+}{\Delta\zeta} - \delta_\zeta^+\hat{C}^-\right)
\end{aligned} \tag{2.56}$$

Here, δ_ξ^-, δ_η^- and δ_ζ^- are the first-order backward differences, while δ_ξ^+, δ_η^+ and δ_ζ^+ are the first-order forward difference operators.

In the LU scheme, the matrices $\hat{A}^\pm, \hat{B}^\pm, \hat{C}^\pm$ may be computed as [89]

$$\hat{A}^\pm = T_A\Lambda_A^\pm T_A^{-1} \quad , \quad \hat{B}^\pm = T_B\Lambda_B^\pm T_B^{-1} \quad , \quad \hat{C}^\pm = T_C\Lambda_C^\pm T_C^{-1} \tag{2.57}$$

where T_A, T_B, T_C are the matrices whose columns are the right eigenvectors of $\hat{A}$, $\hat{B}$ and $\hat{C}$, respectively. Λ_A^+, Λ_B^+ and Λ_C^+ are the positive eigenvalues, while Λ_A^-, Λ_B^- and Λ_C^-

are the negative eigenvalues of $\hat{A}$, $\hat{B}$ and $\hat{C}$, respectively. However, computing the matrices $\hat{A}^{\pm}$, $\hat{B}^{\pm}$ and $\hat{C}^{\pm}$ directly is very expensive.

There are many ways to approximate the matrices $\hat{A}^{\pm}$, $\hat{B}^{\pm}$ and $\hat{C}^{\pm}$. In this present work, the following approach by Yoon and Jameson [87] is used.

$$\begin{aligned}\hat{A}^{\pm} &= \frac{1}{2}(\hat{A} \pm r_A I) \\ \hat{B}^{\pm} &= \frac{1}{2}(\hat{B} \pm r_B I) \\ \hat{C}^{\pm} &= \frac{1}{2}(\hat{C} \pm r_C I)\end{aligned} \tag{2.58}$$

where r_A, r_B, r_C are called the spectral radii or the largest eigenvalues of the flux Jacobian matrices $\hat{A}$, $\hat{B}$ and $\hat{C}$, respectively, and defined as:

$$\begin{aligned}r_A &= k_A \max\left(\left|\lambda_A\right|\right) \\ r_B &= k_B \max\left(\left|\lambda_B\right|\right) \\ r_C &= k_C \max\left(\left|\lambda_C\right|\right)\end{aligned} \tag{2.59}$$

Here, λ_A, λ_B and λ_C represent the eigenvalues of the matrices $\hat{A}$, $\hat{B}$ and $\hat{C}$, respectively. k_A, k_B and k_C are user-input constants, which are greater than or equal to 1 for stability. In this study, $k_A = k_B = k_C = 1$ is used, and equation (2.59) can be evaluated as follows [90]:

$$\begin{aligned}r_A &= \left|U\right| + a(\xi_x^2 + \xi_y^2 + \xi_z^2)^{1/2} \\ r_B &= \left|V\right| + a(\eta_x^2 + \eta_y^2 + \eta_z^2)^{1/2} \\ r_C &= \left|W\right| + a(\zeta_x^2 + \zeta_y^2 + \zeta_z^2)^{1/2}\end{aligned} \tag{2.60}$$

By substituting equation (2.58) into (2.56), equation (2.56) may be rewritten as:

$$
\begin{aligned}
(D+L) &= \left[1 + r_A \frac{\Delta\tau}{\Delta\xi} + r_B \frac{\Delta\tau}{\Delta\eta} + r_C \frac{\Delta\tau}{\Delta\zeta}\right] I - \frac{\Delta\tau}{\Delta\xi} A^{+}_{i-1,j,k} - \frac{\Delta\tau}{\Delta\eta} B^{+}_{i,j-1,k} - \frac{\Delta\tau}{\Delta\zeta} C^{+}_{i,j,k-1} \\
D &= \left[1 + r_A \frac{\Delta\tau}{\Delta\xi} + r_B \frac{\Delta\tau}{\Delta\eta} + r_C \frac{\Delta\tau}{\Delta\zeta}\right] I \\
(D+U) &= \left[1 + r_A \frac{\Delta\tau}{\Delta\xi} + r_B \frac{\Delta\tau}{\Delta\eta} + r_C \frac{\Delta\tau}{\Delta\zeta}\right] I + \frac{\Delta\tau}{\Delta\xi} A^{-}_{i+1,j,k} + \frac{\Delta\tau}{\Delta\eta} B^{-}_{i,j+1,k} + \frac{\Delta\tau}{\Delta\zeta} C^{-}_{i,j,k+1}
\end{aligned}
\tag{2.61}
$$

From equation (2.55), each of the factored matrices can be inverted and the system of equations can be solved to obtain $\Delta\hat{q}^{n+1}$ is detailed below:

$$
\begin{aligned}
(D+L)X &= [RHS]^n \\
D^{-1}Y &= X \\
(D+U)\Delta\vec{\hat{q}}^{n+1} &= Y
\end{aligned}
\tag{2.62}
$$

where each matrix has either lower, or diagonal, or upper part only. The inversion of these matrices can be accomplished by backward or forward substation, which requires less computational work than solving equation (2.51). Finally, the new $\hat{q}^{n+1}$ can be obtained from $\hat{q}^{n+1} = \hat{q}^{n} + \Delta\hat{q}^{n+1}$.

2.3 Turbulence Models

The time-averaged Navier-Stokes equations lead to the Reynolds stress terms $\overline{u_i' u_j'}$, which cannot be solved directly and must be modeled. The Reynolds stresses, in tensor form, can be modeled using an eddy viscosity concept:

$$
-\rho\overline{u_i' u_j'} = \mu_T \left[\frac{\partial \overline{u}_i}{\partial x_j} + \frac{\partial \overline{u}_j}{\partial x_i}\right] \qquad \text{for } i,j = 1,2,3 \tag{2.63}
$$

where u_i', u_j' are the instantaneous velocity fluctuations about the mean velocities $\overline{u}_i$ and $\overline{u}_j$, respectively, and $\overline{u_i' u_j'}$ is the time-averaged value of the product u_i' and u_j'.

In the present RANS simulation, as discussed earlier, the eddy viscosity μ_T is used to account for the effect of turbulent flow.

Though there are many presently known turbulence models, it is an unfortunate fact that there is no single turbulence model that is universally accepted as being superior (accurate, general, and easy-to-solve) for all classes of flow problems. The choice of turbulence model will depend on several considerations such as the physics of the flow, the level of accuracy required, the availability of computer resources, and the amount of time for the simulations.

In the present work, the Spalart-Allmaras (One-Equation) model [91] is used as a baseline model. The SA model has been extensively validated and proved to work well with attached wall-bounded viscous flows, but is not suitable to handle separated flow conditions. The Spalart-Allmaras based Detached Eddy Simulation (SA-DES) proposed by Spalart et al. [92] and implemented by Benjanirat [93] is used to enhance capability of the solver to handle such complex flows.

2.3.1 Spalart-Allmaras Model

In Spalart-Allmaras (SA) turbulence model, a partial differential equation is solved for the production, dissipation, and transport of a turbulent eddy viscosity-like quantity $\tilde{\nu}$ at each time step. Since it requires solving one equation, this model is a one-equation model.

The eddy viscosity μ_T is computed from:

$$\mu_T = \rho \tilde{\nu} f_{v1} \tag{2.64}$$

where the viscous damping function, f_{v1}, is given by

$$f_{v1} = 1 - \frac{\chi^3}{\chi^3 + c_{v1}^3}, \quad \chi \equiv \frac{\tilde{\nu}}{\nu} \tag{2.65}$$

This damping function is used to force the eddy viscosity to be zero at the wall and gradually rises to unity as the distance from wall increases.

The transported variable $\tilde{\nu}$ is determined by the transport equation as follows:

$$\begin{aligned} \frac{D\tilde{\nu}}{Dt} &= c_{b1}[1 - f_{t2}]\tilde{S}\tilde{\nu} + \frac{1}{\sigma}\left[\nabla \cdot ((\nu + \tilde{\nu})\nabla\tilde{\nu}) + c_{b2}(\nabla\tilde{\nu})^2\right] \\ &\quad - \left[c_{w1}f_w - \frac{c_{b1}}{\kappa^2}f_{t2}\right]\left[\frac{\tilde{\nu}}{d}\right]^2 + f_{t1}\Delta U^2 \end{aligned} \tag{2.66}$$

The four terms on the right hand side of equation (2.66) represent the production, the diffusion, the destruction, and the source/trip terms of the eddy viscosity, respectively. Here, $\tilde{S}$ in the production term is defined as:

$$\tilde{S} \equiv S + \frac{\tilde{\nu}}{\kappa^2 d^2} f_{v2} \tag{2.67}$$

and

$$f_{v2} = 1 - \frac{\chi}{1 + \chi f_{v1}} \tag{2.68}$$

where S is the magnitude of the vorticity, and d is the distance to the nearest wall.

In the destruction term, the function f_w is given by

$$\begin{aligned} f_w &= g\left[\frac{1 + c_{w3}^6}{g^6 + c_{w3}^6}\right]^{\frac{1}{6}} \\ g &= r + c_{w2}(r^6 - r) \\ r &\equiv \frac{\tilde{\nu}}{\tilde{S}\kappa^2 d^2} \end{aligned} \tag{2.69}$$

The value of f_w will asymptotically reaches a constant value as *r* increases; therefore, the large value of r can be limited to 10, to avoid floating point overflow [91].

In most simple algebraic (zero-equation) models, the transition is abruptly modeled or computed in a shot ramp based on the grid index. To better represent the transition from laminar to turbulent flow, two trip terms are added to the SA model. The first term is the trip function f_{t2}, which goes to unity upstream of the transition point.

$$f_{t2} = c_{t3} \exp(-c_{t4} \chi^2) \tag{2.70}$$

Another trip function in the source term, f_{t1}, is defined as:

$$f_{t1} = c_{t1} g_t \exp\left[-c_{t2} \frac{\omega_t^2}{\Delta U^2} \left(d^2 + g_t^2 d_t^2 \right) \right] \tag{2.71}$$

where:

$g_t \equiv \min(0.1, \Delta U / \omega_t \Delta x_t)$

ΔU is the difference between velocity at the field point and that at the trip

ω_t is the wall vorticity at the trip point

Δx_t is the grid spacing along the wall at the trip

d_t is the distance from the field point to the trip point on the wall, a user specified transition location.

Use of the trip function allows the eddy viscosity to gradually vary in the transition region. However, the user still needs to specify the transition location, or compute it using a criterion, such as Eppler's [94] or Michel's [95] transition model. In this study, the Eppler's transition model is used (see Section 2.4).

The constants in the SA turbulence model are given by Spalart et al., based on many successfully numerical tests [91]. The constant values used in this work are:

$$\sigma = 2/3 \qquad \kappa = 0.41 \qquad c_{b1} = 0.1335 \qquad c_{b2} = 0.622$$

$$c_{w1} = \frac{c_{b1}}{\kappa^2} + \frac{(1 + c_{b2})}{\sigma} \qquad c_{w2} = 0.3 \qquad c_{w3} = 2 \qquad c_{v1} = 7.1$$

$$c_{t1} = 1 \qquad c_{t2} = 2 \qquad c_{t3} = 1.2 \qquad c_{t4} = 0.5$$

The above recommended values from the original work of Spalart and Allmaras are used in this work, except the last two constants (c_{t3}, c_{t4}) which are modified values in the later version of the SA model [96].

The wall boundary condition in this model is $\tilde{\nu} = 0$. For the freestream boundary condition, ideally $\tilde{\nu}$ should be 0, but a small value $\tilde{\nu} \le \frac{\nu}{2}$ can be used. The value of $\tilde{\nu} = \frac{\nu}{10}$ is recommended, and this value is also used as the initial condition.

In the above discussion, the dimensional from of the SA model has been given. In the actual numerical implementation, all parameters in equation (2.66) were non-dimensionalized accordingly using reference values shown in Section 2.1.2. For example,

$$\begin{aligned}
&\tilde{S} = S + \frac{\tilde{\nu}}{\kappa^2 d^2} f_{v2} \\
&\Rightarrow \tilde{S}^*\left(\frac{a_\infty}{L_{ref}}\right) = S^*\left(\frac{a_\infty}{L_{ref}}\right) + \frac{\tilde{\nu}^*(\nu_\infty)}{\kappa^2 d^2 \left(L_{ref}^2\right)} f_{v2} \\
&\Rightarrow \tilde{S}^* = S^* + \frac{\tilde{\nu}^*}{\kappa^2 d^2} f_{v2}\left(\frac{\nu_\infty M}{L_{ref}(\Omega R)}\right) \\
&\Rightarrow \tilde{S}^* = S^* + \frac{\tilde{\nu}^*}{\kappa^2 d^2} f_{v2}\left(\frac{M}{\mathrm{Re}}\right)
\end{aligned} \tag{2.72}$$

Hereafter, all flow variables are non-dimensional and the asterisk denoting non-dimensional quantities will be dropped for convenience. After non-dimensionalization and mathematical manipulation, the transport equation can be rewritten as:

$$\frac{D\tilde{\nu}}{Dt} = c_{b1}\left[1 - f_{t2}\right]S\tilde{\nu} + \frac{M}{\mathrm{Re}}\frac{1}{\sigma}\frac{\partial}{\partial x_j}\left[\left(\nu + (1 + c_{b2})\tilde{\nu}\right)\frac{\partial \tilde{\nu}}{\partial x_j}\right] - \frac{M}{\mathrm{Re}}\frac{c_{b2}}{\sigma}\tilde{\nu}\frac{\partial^2 \tilde{\nu}}{\partial x_j^2} - \frac{M}{\mathrm{Re}}\left[c_{w1}f_w - \frac{c_{b1}}{\kappa^2}\left[(1 - f_{t2})f_{v2} + f_{t2}\right]\right]\left[\frac{\tilde{\nu}}{d}\right]^2 + f_{t1}\Delta U^2(a_\infty^2) \tag{2.73}$$

Equation (2.73) is a transport equation, and may be solved using an LU scheme similar to the mean flow RANS equations. A first order upwind scheme was used to convect the eddy viscosity. For more detail in numerical solution procedure, the reader is referred to Ref. [93],[96]-[98].

2.3.2 Spalart-Allmaras Detached Eddy Simulation (SA-DES) Model

The Detached Eddy Simulation (DES) methodology usually referred to as a RANS/LES coupling approach. The main idea of this approach is to combine RANS and LES methodologies for applications in which classical LES simulation is not affordable. The DES method attempts to combine the best aspects of RANS and LES in s single solution strategy. This method can be considered as a three-dimensional unsteady numerical simulation using a single turbulence model in regions where the grid density fine enough for a large eddy simulation (LES), and as a RANS simulation in region where it is not.

The DES method uses the idea that if the grid is fine enough, it is possible for the RANS to capture the turbulence by itself. This is possible in an area far away from the surface where turbulent eddy length scale is comparable to the grid size. Therefore, this method aims to better capture the complexities of the massively separated flows. Though

the DES approach may require more computational time than the RANS approach, it still requires much less computational time than a pure LES approach.

SA-DES approach combines a RANS version of the Spalart-Allmaras model and the filtered version of the same model to create two separate regions within the flow domain: one that is near the surface and another that is far away from the surface. The standard SA model will be used in the area close to the wall where the viscous effect prevails and the modeling is dominated by the RANS-based approach. In the high-Re turbulent regions far away from the wall, where large turbulence scales play a dominant role, the LES approach based on a one-equation subgrid model will be used.

This method simulates the turbulence kinetic energy transfer from large turbulence scale to smaller scale, instead of dissipation. This leads to the modification of the production and destruction terms in the transport equation of the standard SA model. As proposed by Shur et al. [99], the modification can be done by substituting the nearest distance to the wall *d*, everywhere in the transport equation, by the new DES length scale $\tilde{d}$, which is defined as:

$$\tilde{d} \equiv \min(d, C_{DES}\Delta) \tag{2.74}$$

where C_{DES} is an adjustable model constant, and Δ is based on the largest grid spacing in the x, y, or z directions forming the computation cell

$$\Delta \equiv \max(\Delta x, \Delta y, \Delta z) \tag{2.75}$$

The model constant $C_{DES} = 0.65$ was set in the homogeneous turbulence [99], and is also used in this study.

In general, the distance *d* is much smaller than the modified length scale $C_{DES}\Delta$ in regions close to the wall. This causes the model to behave as the original SA model. In

the area away from the wall, $C_{DES}\Delta$ becomes smaller than the distance *d*. The length scale $\tilde{d} = C_{DES}\Delta$ in the LES region yields a Smagorinsky-like eddy viscosity $\tilde{\nu} \propto S\Delta^2$ and causes the model to behave LES-like manner. Analogous to classical LES, the role of Δ is to allow the energy cascade down to the grid size.

2.4 Transition Model

In this study, the effects of transition are modeled using Eppler's transition criterion [94]. The Eppler's transition model is used in many NREL airfoil analysis and design procedures, and is known to give accurate prediction of the transition location and airfoil drag characteristics.

This model was implemented as follows. First, the streamwise growth of laminar boundary layer quantities such as the momentum thickness, shape factor H, energy thickness δ_3, and the factor $H_{32}= \delta_3/\theta$ are empirically computed using an integral equation technique. Transition is predicted to occur if the Reynolds number based on the momentum thickness becomes large so that:

$$\log\left(\frac{u_e\theta}{\nu}\right) > 18.4H_{32} - 21.74 - 0.34r \tag{2.76}$$

Here '*r*' is a roughness factor. For highly polished surfaces, *r* may be taken to be zero. A value of 4 is used for insect contaminated surfaces, and value of *r* = 6 is considered a very rough surface.

It must be emphasized that Eppler's model is intended for viscous flows where the boundary layer is steady, at least in a Reynolds time-averaged sense. Flow around wind turbines is highly unsteady, and the Eppler's criterion will, at best, give only a first order estimate of the transition location. This model also predicts that transition has

occurred if the laminar boundary layer separates, causing a separation bubble near the leading edge of the rotor.

Another widely used transition model is Michel's model [95]. This model can predict a transition region based on the extension proposed by Chen and Thyson [100]. This model is used in many aircraft industry boundary layer codes, for example the boundary layer codes developed by Cebeci [101] for the Douglas Aircraft Co.

Benjanirat [93] has tested both Eppler's and Michel's models for limited number wind conditions. The transition locations predicted by both models are nearly the same. For more detail of Michel's transition model, the reader is referred to Ref. [12],[93],[95]. All the simulations reported in this study were done using Eppler's transition model.

2.5 Initial and Boundary Conditions

Since the governing equations are parabolic with respect to time, initial and boundary conditions are needed to solve these equations. In general, the initial conditions are set to be equal to the properties of the freestrem flow condition. In the present work, calculations involve moving grids. Thus, an inertial coordinate system (i.e. a stationary observer) is adopted. The coordinate system is fixed to the blade, and the blade rotates with respect to the surrounding flow.

The boundary conditions must be carefully specified to obtain the solutions, and the implementation is usually based on physics. For example, the no-slip condition should be used for the viscous surface, while the slip condition may be used in an inviscid simulation. For the CCW application, jet slot exit boundary condition must be properly specified for accurate simulation of the effects of the jet flow.

2.5.1 Initial Conditions

In this study, the rotor blade is impulsively started from rest at the start of the computation. The flow properties everywhere inside the flow field are assumed to be uniform and set to the freestream values. The following initial values are used:

$$\begin{aligned} u &= u_\infty \\ v &= v_\infty \\ w &= w_\infty \\ \rho &= \rho_\infty \\ p &= p_\infty \\ T &= T_\infty \end{aligned} \tag{2.77}$$

2.5.2 Boundary Conditions

Blade Surface

For all solid surfaces, the no-slip condition is applied for the viscous flow.

$$\vec{V} = \vec{V}_{grid} \quad \text{or} \quad u = x_\tau, v = y_\tau, w = z_\tau \tag{2.78}$$

where $\vec{V}_{grid}$ is the velocity of the blade surface.

All the solid surfaces are also assumed to be adiabatic walls, $\frac{\partial T}{\partial n} = 0$. The pressure at the surface, except the jet slot, is determined from the specification that the pressure gradient at the surfaces be zero. That is:

$$\frac{\partial p}{\partial n} = 0 \quad \text{or} \quad p_{i1} = (4p_{i2} - p_{i3})/3 \tag{2.79}$$

where subscript ‘i1’ represents the point on the surface, and ‘i2’, ‘i3’ is one point and two points next to the surface in normal direction, respectively.

Similarly, the density at the surface is also extrapolated from the interior field points using the following expression:

$$\frac{\partial \rho}{\partial n} \approx 0 \quad \text{or} \quad \rho_{i1} = (4\rho_{i2} - \rho_{i3})/3 \tag{2.80}$$

The total energy is computed from the equation of state.

Inboard, Outboard and Downstream

At the inboard and outboard boundaries, it is assumed that the gradients along the spanwise direction are negligible. The downstream boundary condition is defined at the downstream boundary where the wake from the blade leaves the computational domain. Flow properties (density, velocities) on these surfaces are extrapolated from the interior field points, except for pressure which is specified at its freestream value.

Branch/Wake Cut

For a multiple connected domains, there will be necessity to introduce a branch cut across the wake region to obtain a simply connected region. Since the flow properties must be physically continuous across this cut, the flow properties here are simply specified as averages of the variables using the properties one point above and one point below the cut line.

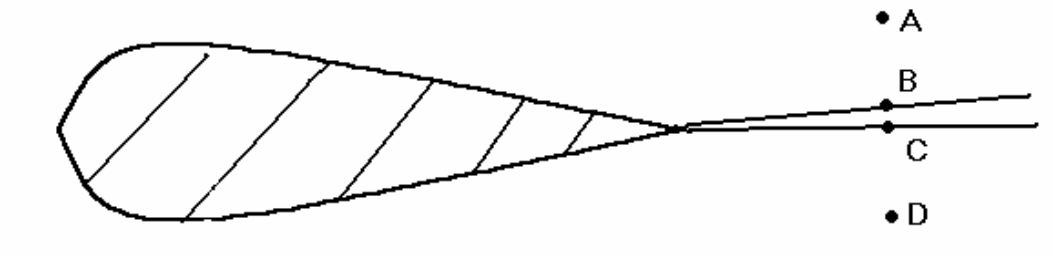

Figure 2.3 Wake cut boundary condition for C grid

As shown in Figure 2.3, point B and point C are at the same location that happens to be on both sides of the cut line. Thus, $q_B = q_C$. Continuity of properties is ensured by setting $q_B = q_C = \frac{1}{2}(q_A + q_D)$.

Outer Boundary

The outer boundary is usually placed far away from the blade surface, at least 6 chords, to avoid reflections from outer boundary into the interior domain and to allow the disturbances to leave the domain. In this study, the flow density is extrapolated from the interior field points while other properties (velocities, pressure) are specified to the freestream values.

Tip and Root Vortices Modeling

Because the grid surrounding the rotor blade is finite, it can not capture the details of the tip vortex (and vortices from other blades) once the vortex leaves the domain, as shown in Figure 2.4. A prescribed wake trajectory proposed by Kocurek [102],[103] is assumed for these vortex structures, once they leave the computational domain. Their strength is assumed to the peak bound circulation on the blade at the time the vortex was generated. The presence of other blades and the effect of the tip and root vortices not captured by the computational grid are accounted with an induced velocity flow field at this outer boundary. The vortices from all the blades are included with the phase lag ($2\pi/N$, where N is the number of blades) properly taken into account.

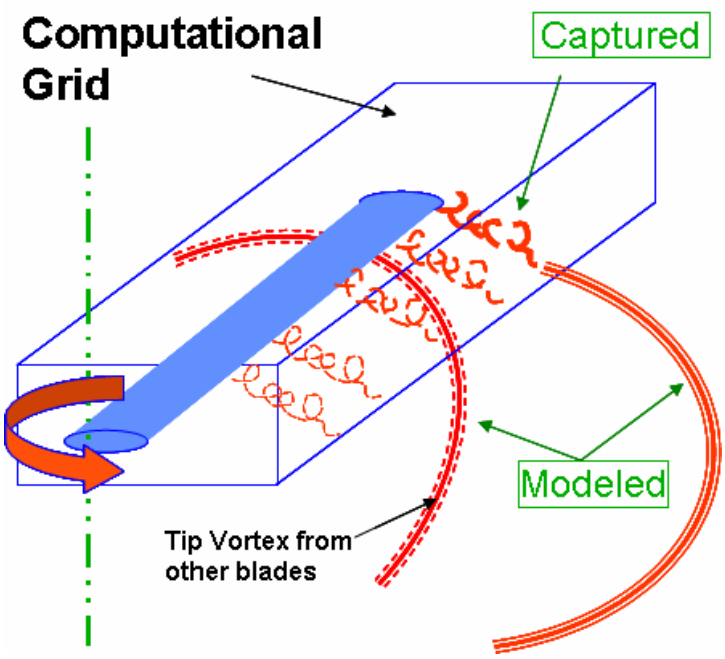

Figure 2.4 Sketch of the hybrid methodology

The velocity at the outer boundary can be prescribed as follows:

$$\vec{V} = \vec{V}_{wind} + \vec{V}_{induced} \tag{2.81}$$

where $\vec{V}_{wind}$ is the wind velocity and $\vec{V}_{induced}$ represents the induced velocities from the tip and root vortices. The induced velocities are computed using Biot-Savart law and then fed back to the computational grid through the outer boundary (Figure 2.5). The vortices are represented by a series of straight-line segments, on each of which the vortex strength is assumed to be constant. The end points of these segments (markers) and the strength of all segments are computed and updated at every 10 degree increments of azimuth. Because a Lagrangean, rather than an Eulerian, representative of the vortices is used, the details of the flow field in the immediate vicinity of the vortex will not be captured. However, the global effects of the vortex (i.e. the induced inflow) will be captured well.

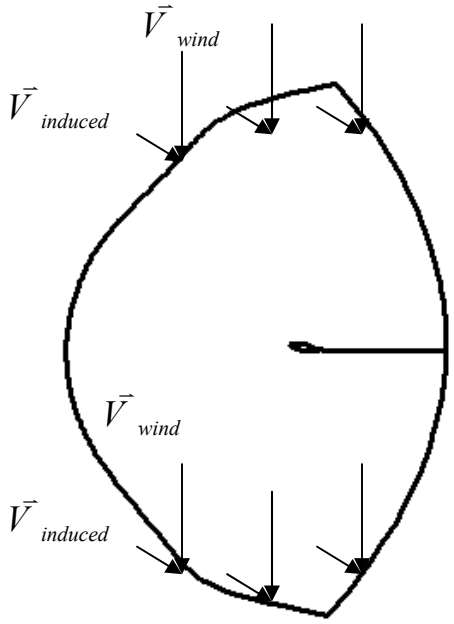

Figure 2.5 Induced velocities and wind velocities at the boundary

Jet Slot Exit

In most circulation control studies, the driving parameter of the jet is the momentum coefficient, C_μ , which is defined as follows:

$$C_\mu = \frac{\dot{m} V_{jet}}{\frac{1}{2}\rho_\infty V_{ref}^2 A_{ref}} \tag{2.82}$$

where $\dot{m} = \rho_{jet} V_{jet} A_{jet}$ is the jet mass flow rate. In the present study, the reference velocity V_{ref} is the rotor tip speed, and the reference area A_{ref} is the plan form area of the rotor blade.

At the jet slot exit, the following boundary conditions are specified: the total pressure and total temperature of the jet are specified. These were estimated assuming a jet Mach number and isentropic relations. The jet is assumed to emanate in a direction tangential to the blade surface, and the pressure values at the jet are extrapolated from the pressure values in the outer flow over the airfoil. The jet velocity profile is specified to be

parabolic at the jet exit. The physics of the jet slot boundary conditions are shown in Figure 2.6.

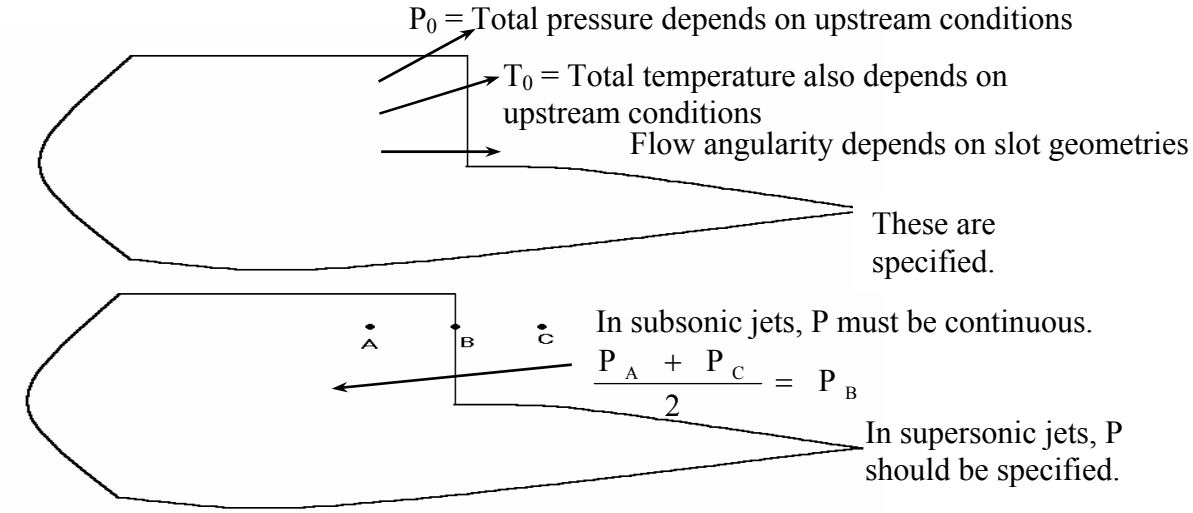

Figure 2.6 Jet slot boundary conditions

For subsonic jets, one characteristic can propagate upwind into the slot. Thus the pressure at the jet exit is extrapolated from the outside values using the same constraints as equation (2.79). Then the static pressure at the jet slot exit can be obtained as:

$$p_{jet} = p_{i1} = (4p_{i2} - p_{i3})/3 \tag{2.83}$$

From equation (2.82), the momentum coefficient can also be expressed as:

$$C_\mu = \frac{\rho_{jet} V_{jet}^2 A_{jet}}{\frac{1}{2}\rho_\infty V_{ref}^2 A_{ref}} \tag{2.84}$$

From the ideal gas law and the equation of state, the following relations can be obtained:

$$V_{jet}^2 = \frac{2\gamma}{\gamma - 1} R(T_{0,jet} - T_{jet}) \quad \text{and} \quad \rho_{jet} = \frac{p_{jet}}{RT_{jet}} \tag{2.85}$$

Substituting equation (2.85) into (2.84), the expression for C_μ with only one unknown variable can be obtained:

$$C_\mu = \frac{2\gamma}{\gamma - 1}\left(\frac{A_{jet}}{\frac{1}{2}\rho_\infty V_{ref}^2 A_{ref}}\right)\frac{p_{jet}(T_{0,jet} - T_{jet})}{T_{jet}} \tag{2.86}$$

The only one unknown variable is T_{jet}, which can be easily solved from the above equation.

After the T_{jet} is calculated, the other jet flow variables, such as V_{jet} and ρ_{jet}, can be obtained from equation (2.85). These parameters are also non-dimensionalized by corresponding reference values before used in the solver as the boundary conditions.

For supersonic jets, no information can be propagated upstream into the slot, thus the extrapolation of jet exit pressure from the outside points is not correct. Because the jet slot is assumed to be the throat of the nozzle, the local Mach number at the jet slot should be unity. And the jet velocity at the exit should be equal to the local speed of sound.

From the isentropic relations for the total temperature and jet exit temperature

$$\frac{T_{0,jet}}{T_{jet}} = 1 + \frac{\gamma - 1}{2} M_{jet}^2 \tag{2.87}$$

where $M_{jet} = 1$, and the T_{jet} can be easily solved as the $T_{0,jet}$ is known.

After the T_{jet} is obtained, other jet flow quantities could be determined for the supersonic flow from the equations (2.84) and (2.85).

CHAPTER 3

WIND TURBINE PERFORMANCE UNDER YAWED FLOW CONDITIONS

As discussed earlier, the aerodynamics of the HAWT is more complex for yawed flow than for axial flow conditions as a consequence of the azimuthal variation in the relative velocity between the blade sections and the fluid. The skewed wake shed from the blade tips causes unsteady, spatially non-uniform inflow through the rotor. Under certain conditions, flow separation, blade-vortex interactions, and dynamic stall can occur. An improved understanding in such complicated flow and the ability to accurately predict the unsteady airloads can greatly help wind turbine designer to efficiently design the rotor to meet the aerodynamic and structure requirements.

In this chapter, the viscous flow solver based on the numerical formulation and boundary conditions described in Chapter 2 is used to study the performance of the wind turbine under yawed flow conditions. The wind speed in yawed flow conditions are divided into three regimes (low, moderate, high wind speeds), and the results are discussed in the following sections. Computational grid, grid sensitivity study, and the effect of turbulence model are also presented.

Calculations have been obtained for the NREL Phase VI rotor at four wind speeds (5, 7, 10, and 15 m/s); at four yaw angles (10, 30, 45, and 60 degrees). As stated earlier, an excellent experimental database is available for this rotor, and has been used to calibrate a variety of solution techniques ([57],[58],[104],[105]). The assessment of the present method was done by comparing the predictions with the following measurements:

(a) radial variation of the normal force coefficient C_N and tangential force coefficient C_T; (b) variation of time-averaged torque generated by the rotor as a function of yaw angle and wind speed; (c) time-averaged root flap moment variation as a function of wind speed and yaw angle; (d) surface pressure distributions at selected radial sections. The error bars show the uncertainties in measured data at one standard deviation.

Because the flow over a rotor in yaw is inherently unsteady, the aerodynamic loads fluctuate about time averaged (mean) values. The experimental database contains both unsteady (raw) data and time averaged data. Comparisons with the time averaged data are mostly presented. Only the results of yawed flow conditions are discussed. For further results of axial flow conditions, the reader is referred to Ref. [93].

3.1 Computation Setting

3.1.1 Computational Grid

The NREL Phase VI rotor geometry is based on an S809 airfoil. More details of the rotor can be found in Ref. [57]. In the present work, all calculations were done on a C-H grid generated using a hyperbolic single-block structured grid generator. The three-dimensional computational domain is constructed from a series of 2-D C-grid with H-type topology in the spanwise direction. The computational domain and the grid in vicinity of rotor surface are shown in Figure 3.1. In this figure, the rotor was moving from the right to the left, and the wind direction is directed upwards perpendicular to the rotor disk.

The grid is clustered near the rotor leading edge and trailing edge, and the root and the tip of rotor in order to accurately capture the suction peak and the effect of tip and root vortices. There are about 1.2 million grid points in a single block. There are 181

points in the C- or wraparound direction, 100 points in the radial direction including 70 radial stations on the rotor blade, and 65 points in the normal direction. The first point off the wall is placed at 2.5×10^{-4} of chord. The associated y^+ values vary approximately from 5 near the leading edge to 1 near the trailing edge. The higher value of y^+ near the leading edge will create local errors in the eddy viscosity levels. These are expected to be small, given the laminar behavior of the flow near the leading edge. The far field boundaries are placed approximately six chords upstream and downstream the rotor blade. The far field boundary in spanwise direction is located approximately one radius of the rotor away from the tip.

The computational domain used in this present work is called the free configuration, where the rotor is modelled without the presence of wind tunnel walls. The compared experimental data of NREL Phase VI rotor, however, were obtained from wind tunnel tests. Sørensen et al. [106] have done a series of computations of the NREL Phase VI rotor using two different configurations; free configuration (rotor only), and tunnel configuration (tunnel wall included). Their results indicated that the differences between the results from the free configuration and the tunnel configuration are very small for all integrated quantities and surface pressures.

3.1.2 Computer Time

At the low wind speed, 18000 time steps are needed per blade revolution, representing the rotational movement of the blade by 1/50 degree of azimuth every time step. At higher wind speeds, where unsteady effects are more dominant, a smaller time step equivalent to a 1/100 degree azimuth is used. The time step used in this study is approximately 5×10^{-5} s, which is very small compared to the vortex passage time constant

for dynamic stall ($c/\Omega R$) [107],[108] for an S809 airfoil which is approximately 0.01 s. Therefore the time step chosen should be able to resolve dynamic stall.

All computations in the present study were performed on a desktop computer with a single 3.40GHz Intel Pentium IV processor and 1 GB of RAM. For low wind speed conditions, each revolution of the rotor (18000 time steps) took approximately 26 hours of wall clock time. Calculations were done for 3 to 4 rotor revolutions. The solutions from the final revolution were used in the following discussions.

As stated earlier, the solution is made of two parts: the immediate flow field over the rotor that is modeled using Navier-Stokes equations, an initial helical geometry is assumed for the tip vortex. When the solution is started, the inflow effects of the far field vortex structure are already accounted for in the calculation. Thus only 3 to 4 revolutions are needed to establish the near wake behind the blade that is captured by the Navier-Stokes analysis, and to adjust the time-dependent strength of the tip vortex filaments. For further details of this procedure, the reader is referred to Ref. [12].

3.2 Code Validation with NREL Phase VI Rotor

Prior its use to study rotor performance under yawed flow condition, the Navier-Stokes solver is validated by modeling the flow field over the NREL Phase VI rotor under axial flow (zero yaw) conditions and comparing the computed results with experimental data from NREL. Only a comparison of the power output data is shown here. For more detailed study of the wind turbine under axial flow conditions and further validations, the reader is referred to Ref. [12] and [93].

Figure 3.2 shows the computed and measured power output at wind speed ranged from 7 to 20 m/s with zero yaw conditions. Reasonable good agreement with measurements is observed.

3.3 Grid Sensitivity Study

A grid sensitivity study has been performed to investigate the effect of grid density on the force coefficients under a yawed flow condition. Three grids, ~ 0.6×10^6 (0.6M), 1.2×10^6 (1.2M) and 2.4×10^6 (2.4M) cells, were used in this investigation. As shown in Figure 3.3, the grid density has a negligible effect on the computed normal force coefficient C_N. It is also seen that grid density has a comparatively small effect on the tangential force coefficient C_T. Even though the 2.4M grid gave better result in C_T than the 1.2M grid (approximately 5% more accurate), the 1.2M grid described in Section 3.1 was used in the present work for all calculations due to its 50% smaller computation time per simulation.

3.4 Low Wind Speed: Attached Flow Conditions

We first present results at selected low wind speeds of 5 and 7 m/s for yaw angles up to 60 degrees. At these conditions, the angle of attack observed by the turbine blade is comparatively small. The airflow around the blade is attached to the blade surface and no separation is observed. A visualization of the computed flow indicates that the flow is well-behaved and attached over much of the rotor. Under these conditions, on the present grid and the baseline turbulence model, one can expect the results to be in reasonable agreement with measurements. This indeed turns out to be the case.

Figure 3.4 and 3.5 show the radial distribution of the pressure force normal to the chord at 5 and 7 m/s respectively. A reasonable agreement with measurements is

observed. Figure 3.6 and 3.7 show the corresponding tangential forces at 5 and 7 m/s respectively. It should be noted that the tangential forces are quite sensitive to the pressure distribution in the leading edge stagnation region, and trailing edge recompression region. Since the experiments had only a few pressure taps in these regions, it is difficult to measure C_T value due to the sparseness of the pressure taps. Due to the small of C_T, approximately 1/10 of C_N, any small deviation in either lift or drag can cause a significant error in C_T. One cannot expect the measured C_T values to be as accurate as the C_N values. The qualitative agreement between the measurements and the predictions is reasonable when this uncertainty in the measurements of C_T is factored in. The prediction of transition influences the prediction of skin friction drag, and can also affect the tangential force at these low wind speeds.

Figure 3.8 shows the variation of shaft torque with yaw angle at these wind speeds. While the trend is correctly predicted, the computed torque shows approximately 15% discrepancy at the lower wind speed of 5 m/s. The shaft torque at these low wind speeds is dominated by the radial distribution of the tangential forces, which could not be predicted well, especially in high yaw condition. At the higher wind speed of 7 m/s, the discrepancy between prediction and measurements is within 10%.

Figure 3.9 shows the root flap moment as a function of yaw angle. This quantity is dominated by the normal force effects. The root flap moment is weighted with the radius and therefore the relatively large errors at the inboard section contribute relatively small. Good agreement with experiment is observed. Figures 3.10-3.17 show surface pressure distributions at five radial locations and four yaw angles, at wind speed 5 and 7

m/s respectively. A reasonable agreement between prediction and measurements is observed for all yaw angles.

It should be noted that the computations show a better agreement with the measurements for the shaft torque and root flap moment than for the computed C_T values. This is due to the fact that C_T are obtained from the pressure taps on the blade surface, while the shaft torque and the root flap moment are measured directly by the strain gauges located near the rotor hub.

3.5 Moderate Wind Speed: Partially Separated Flow Conditions

We next look at the flow conditions, where the flow over the rotor is partially separated. As wind speed increase, stall occurs at some inboard radial locations where the angle of attack observed by the rotor blade is relatively high. However, higher power is still generated at other outboard radial locations where the flow is still attached. This results in a comparatively constant power output in the moderate wind. This concept to limit the maximum power output by allowing part of the blade to stall is called “Stall Regulation”. The stall regulation provides the simplest passive power regulation, ensuring that the installed generator and gearbox are not overloaded as the wind speed increases.

Results from Benjanirat [93] indicated that, for the NREL Phase VI rotor, stall occurs from 9 m/s onward, and it can be seen from the root of the rotor up to around mid-span location. The effect of stall is also observed in Figure 3.2 as a small drop in power output at wind speed 13 m/s.

Results at 10 m/s and 13 m/s winds are selected to represent this wind speed regime. Calculations have been done at four yaw angles (10°, 30°, 45° and 60°) for 10 m/s, and at two yaw angle (10°and 30°) for 13 m/s.

In this regime where the flow is inherent partially separated, transition plays a critical role in where flow separation occurs. In order to simulate the flow accurately, accurate prediction of the transition location is needed. In the present study, Eppler's transition model was used. The combinations (Eppler's transition model, SA turbulence model) gave acceptable results for C_N and for torque, although C_T distributions and root flap moments were reasonable (see Figures 3.18-3.23). The C_T distributions also show that when the wind speed reaches approximately 10 m/s, the separation point is moved close the r/R = 0.47 section. As the wind speed increases to 13 m/s, the separated flow area spreads, as seen by the widening of the dip of C_T in Figure 3.21. Separation prediction affects the pressure distribution (Figures 3.24-3.29), particularly in the leading edge suction region. The tangential force C_T is sensitive to these effects and could not be predicted well. Partially separation over the upper surface is clearly seen in Figure 3.28. It is obvious that measurements show a leading edge separation from r/R = 0.30 section to r/R=0.63 section, while the computations are preserve a sharp suction peak.

3.6 High Wind Speed: Fully Separated Flow Conditions

Another extreme case is where the wind velocity is high enough (≥15 m/s) to cause flow separation over the entire upper surface of the turbine blade. Because the flow was fully separated, more advance turbulence model may be required to simulate the separation more accurately. For the following computations, the baseline SA turbulence model was used. Some of these simulations were repeated with implementation of

advance turbulence model, Spalart-Allmaras Detached Eddy Simulation (SA-DES), and the SA-DES results are presented in Section 3.6.

Figure 3.30 and 3.31 show the radial distribution of the normal and tangential forces at four yaw angles. The normal force was again in reasonable agreement, except at 60° yaw. Under high wind conditions, the torque generation and root flap bending moment are influenced more by their in-plane and normal-to-plane component of the lift force (Figure 3.32 and 3.33).

Figures 3.34-3.37 show the pressure distribution at 15 m/s wind with four yaw angles. The agreement is reasonable except at the inboard stations where the present approach does not capture the pressure plateau seen in experiments, cause by the leading edge separation.

3.7 Variation of Power as a Function of Wind Speed

We next look at the power generated by rotor in Figure 3.38. At low wind speed conditions (5 and 7 m/s), where the flow remains attached over much of the rotor, the computed results show good agreement with the experiments. The agreement is observed in the high yawed flow conditions as well. At wind speeds greater than 10 m/s and at low yaw angles the present study does not properly model the partially separated flow over the rotor, the predictions exhibit some discrepancies. At high yaw angles (45° and 60° yaw), the computed results are again reasonable agreement even at high wind speeds. This is because the in-plane component of the relative wind is increased due to the high yaw angle. The rotor blade sections operate in lower angles of attack, which lead to reduced flow separation over the upper surface.

3.8 Effect of Advanced Turbulence Model (SA-DES)

At extreme wind conditions and high yaw angle, the flow is separated over the entire upper surface of the blade. Results as discussed earlier show that the present approach, with the use of the Spalart-Allmaras (SA) turbulence model, does not capture the flow separation accurately. The SA model has been known to work well with attached wall-bounded viscous flows, but is not suitable to handle separated flow conditions. Therefore, for this present approach to accurately predict the wind turbine performance, the ability to predict the extent of flow separation is needed. Benjanirat [93] has implemented SA-DES and k-ω SST turbulence models and applied them to HAWTs for axial flow conditions. Based on his study, the SA-DES model is implemented in the present work to investigate the case at high wind speed and high yaw angle.

Calculations have been done for selected conditions at high wind speed and high yaw angle; 15 m/s wind with 10° and 60° yaw. It is seen that the normal forces (Figure 3.39), and the tangential forces (Figure 3.40), are both better predicted with the SA-DES turbulence model. The surface pressure distributions were also better predicted with the SA-DES. The SA model based simulations tend to overpredict both the normal and the tangential forces. For 10° yaw case, the SA-DES model performs better in capturing the leading edge stall than the SA model leading to less normal force and tangential forces predicted. Also, for 60° yaw case, the SA-DES model once again performs better in predicting the suction peak than the SA model yielding larger predicted normal and tangential forces.

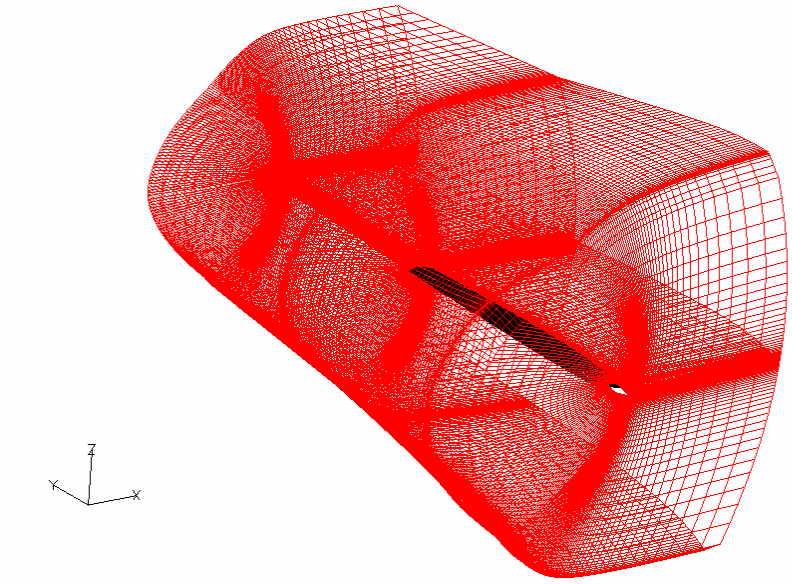

(a) 3-D Computational domain

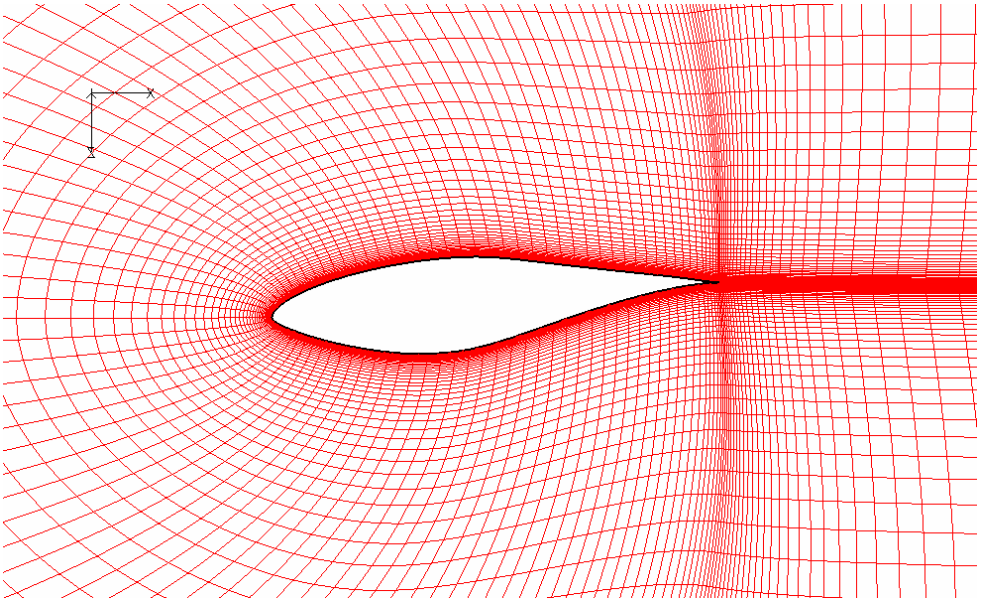

(b) Mesh in vicinity of rotor surface

Figure 3.1 Body-fitted C grid of the rotor

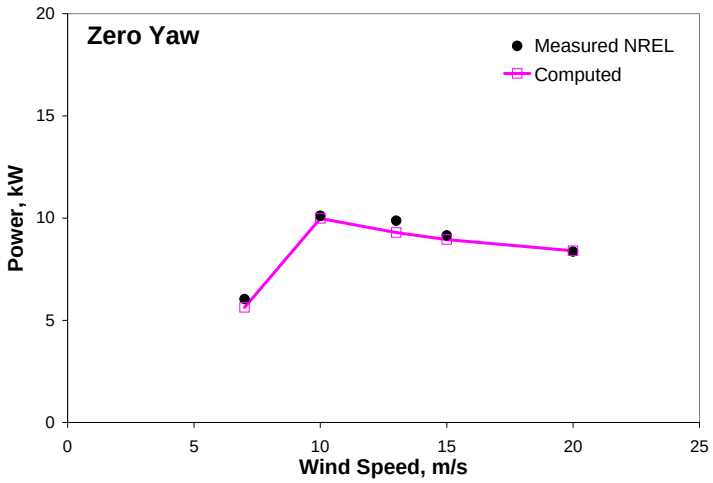

Figure 3.2 Comparison of computed and measured rotor power output

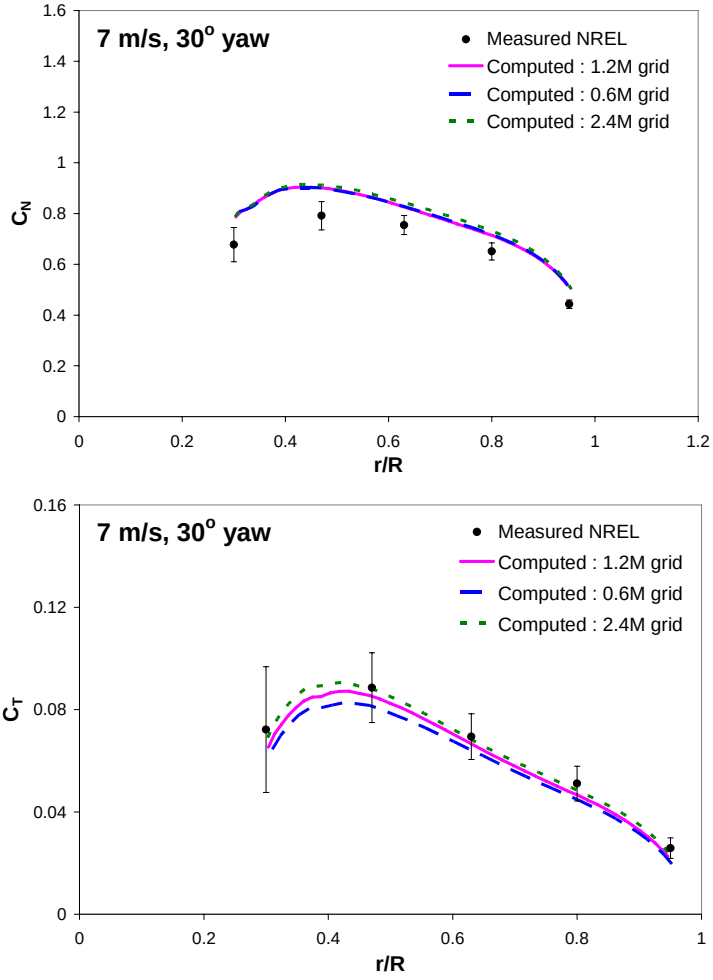

Figure 3.3 Effect of grid density on computed force coefficients

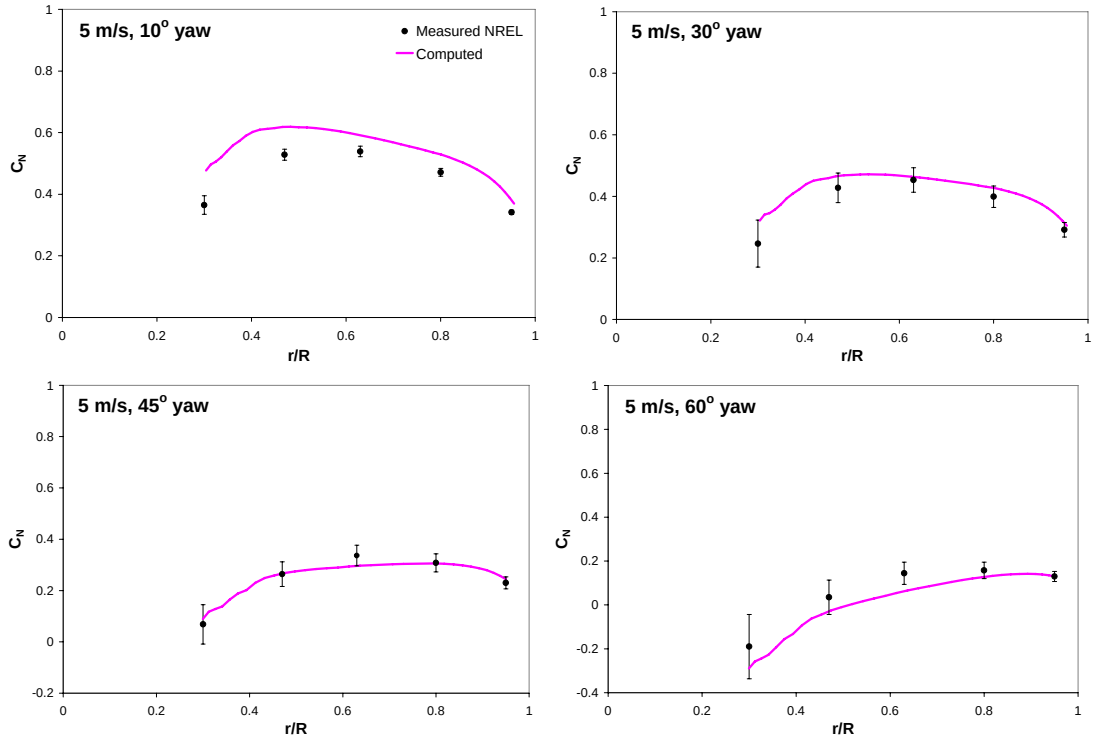

Figure 3.4 Radial distribution of the normal force coefficient C_N at 5 m/s

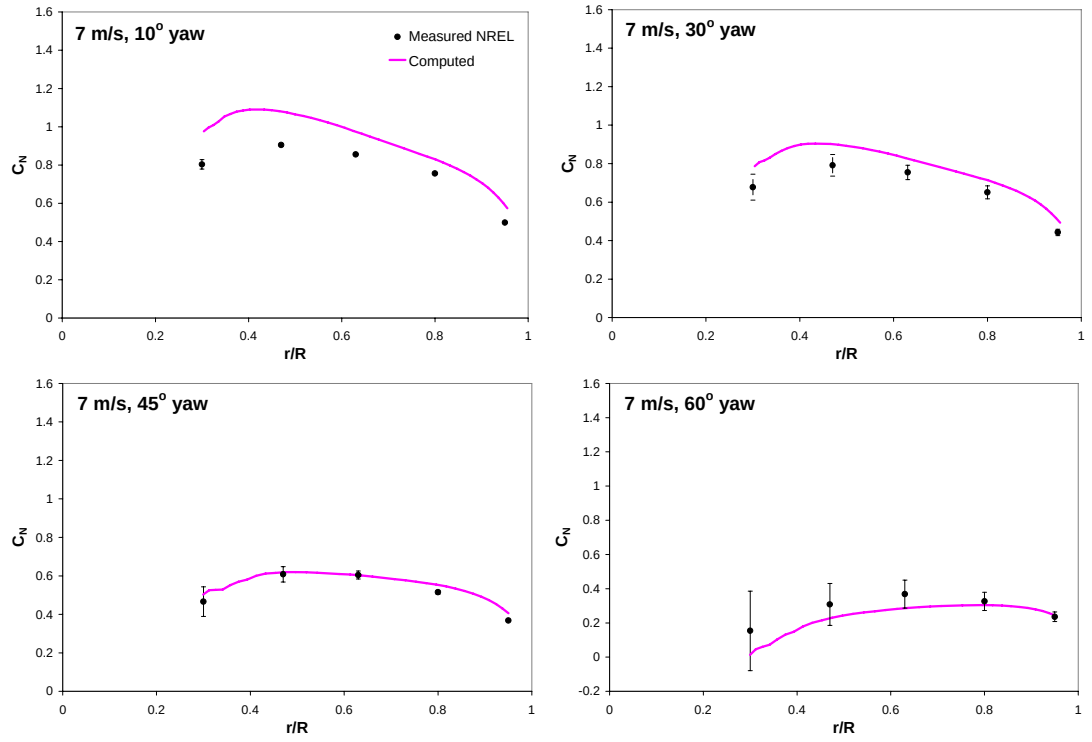

Figure 3.5 Radial distribution of the normal force coefficient C_N at 7 m/s

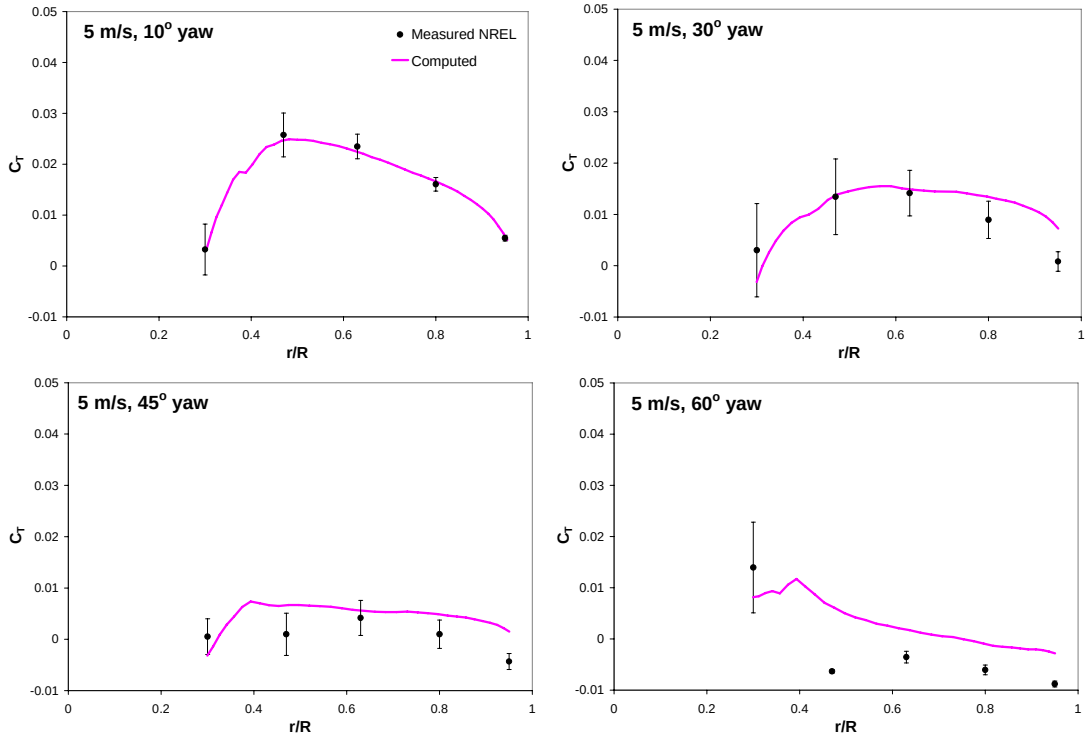

Figure 3.6 Radial distribution of the tangential force coefficient C_T at 5 m/s

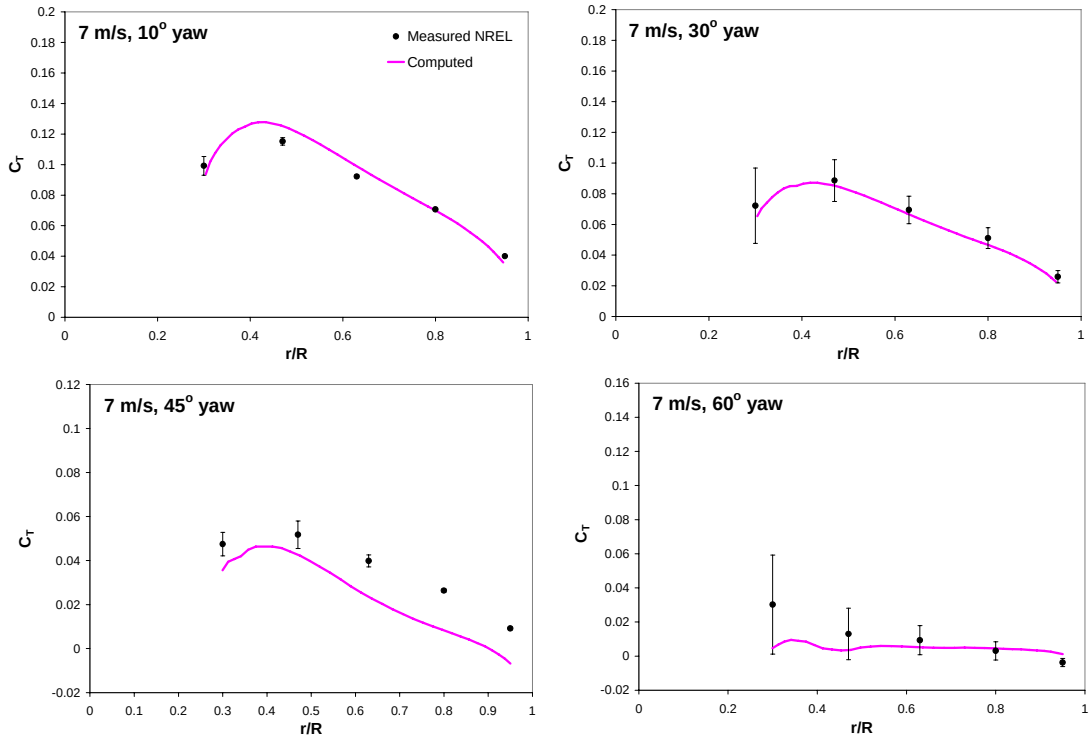

Figure 3.7 Radial distribution of the tangential force coefficient C_T at 7 m/s

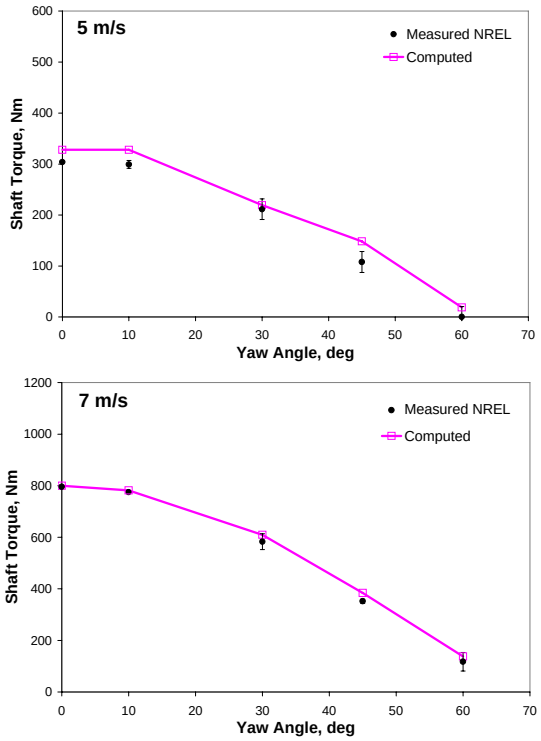

Figure 3.8 Variation of the torque generated by the rotor as a function of yaw angle

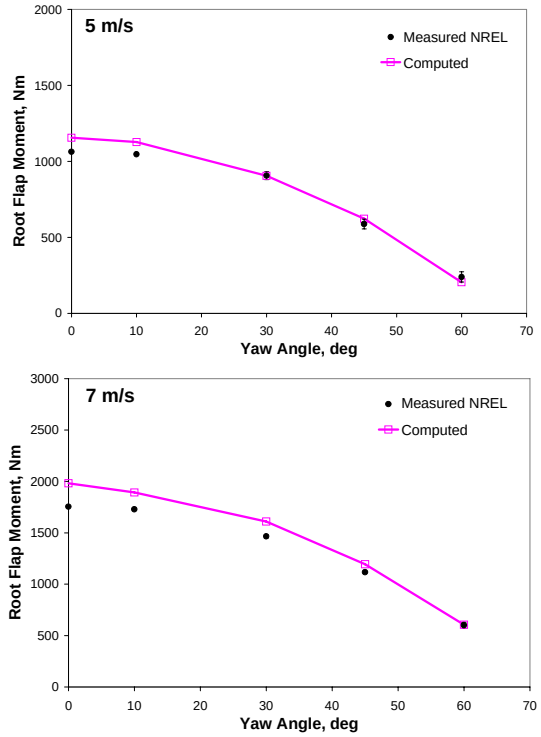

Figure 3.9 Variation of the root flap moment as a function of yaw angle

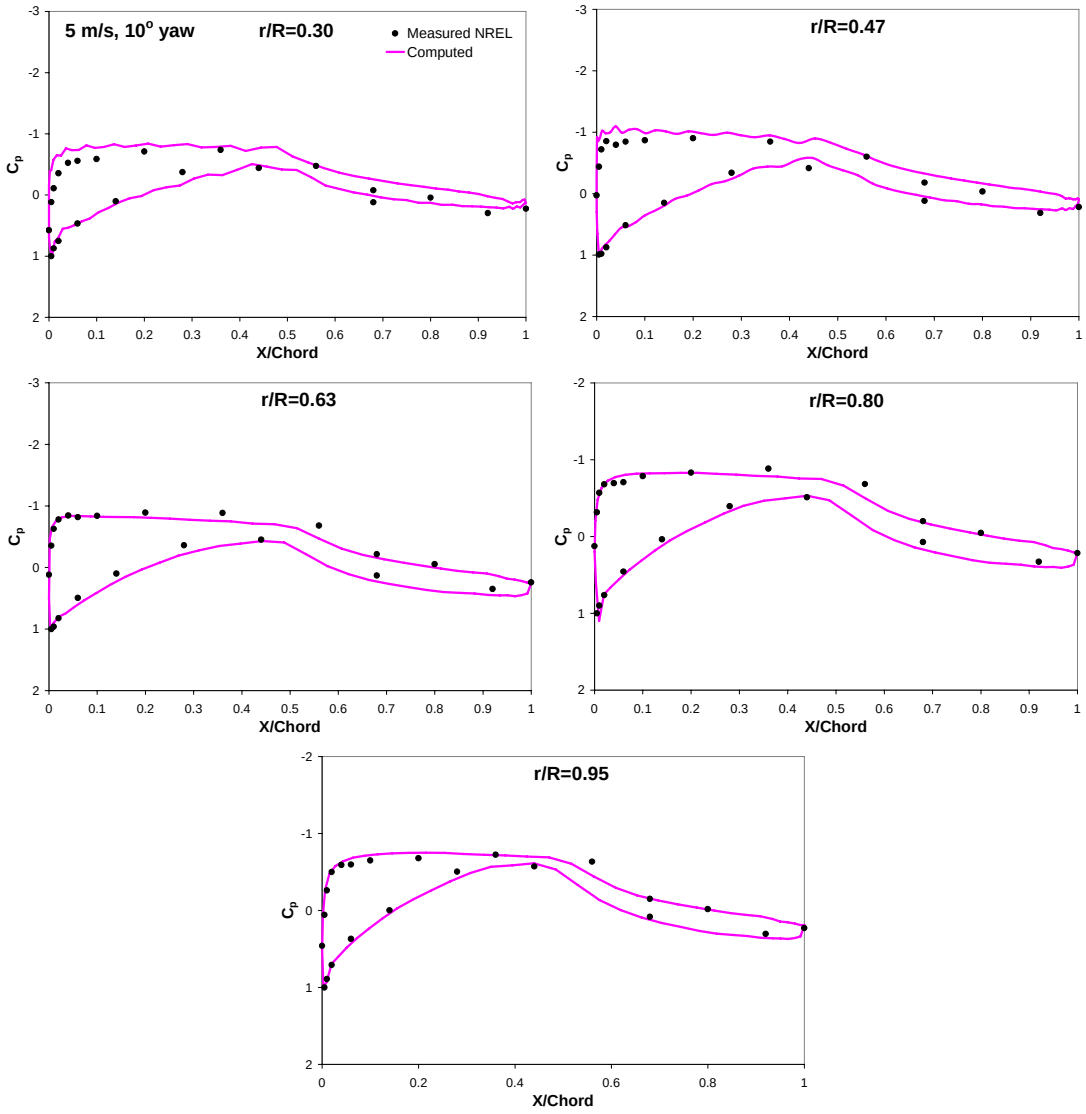

Figure 3.10 Pressure distribution of the 5 m/s and 10° yaw case

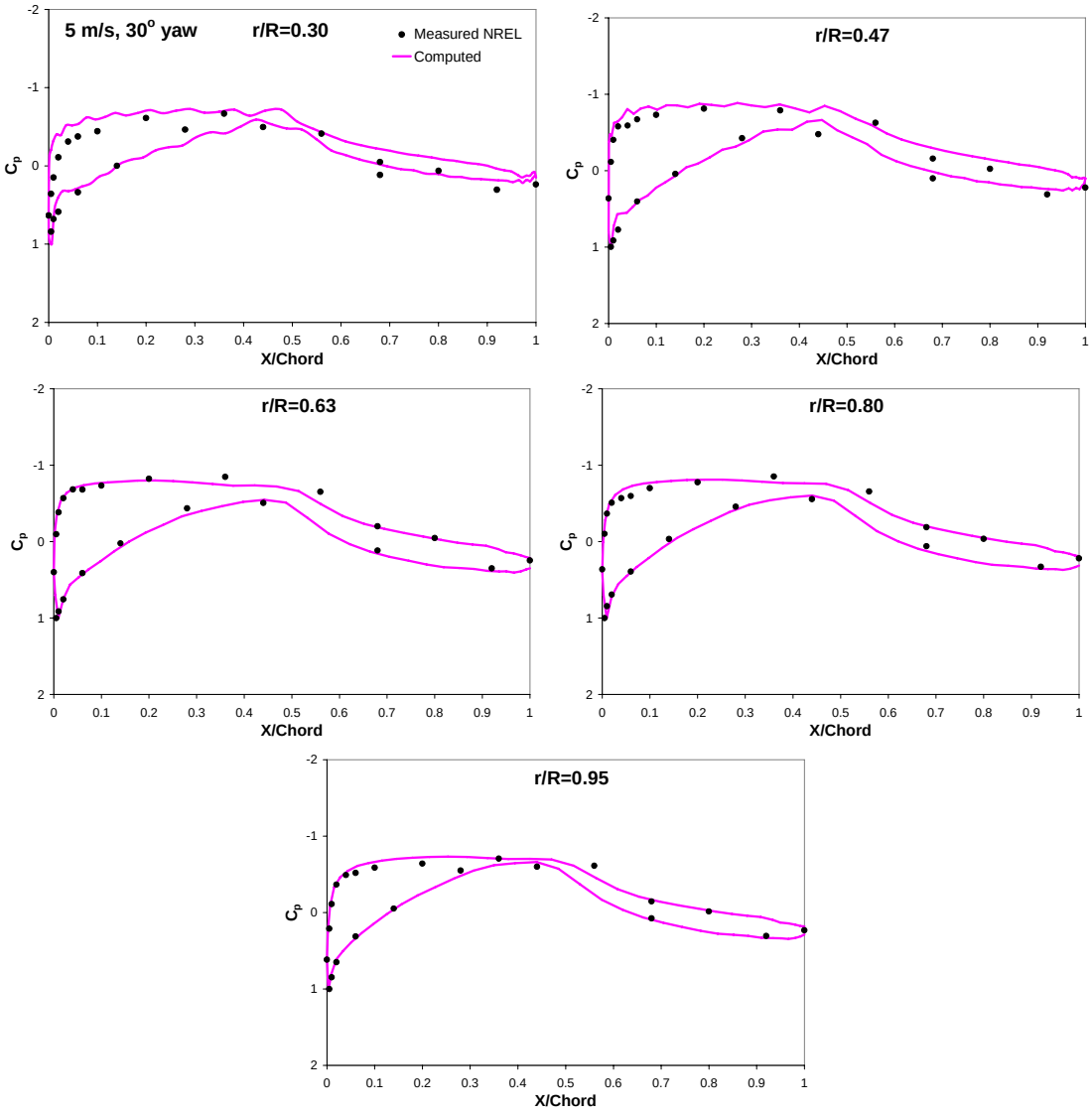

Figure 3.11 Pressure distribution of the 5 m/s and 30° yaw case

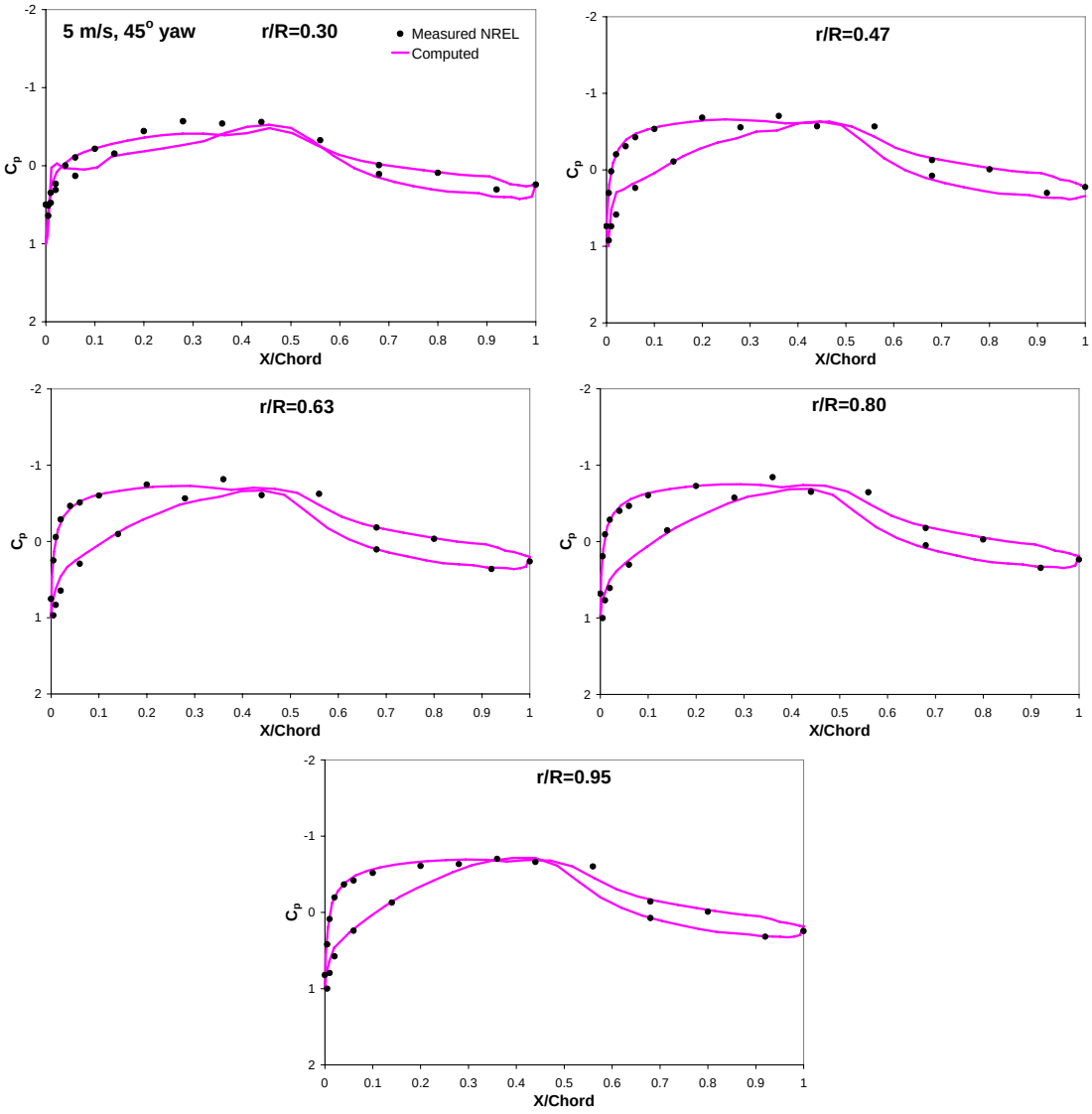

Figure 3.12 Pressure distribution of the 5 m/s and 45° yaw case

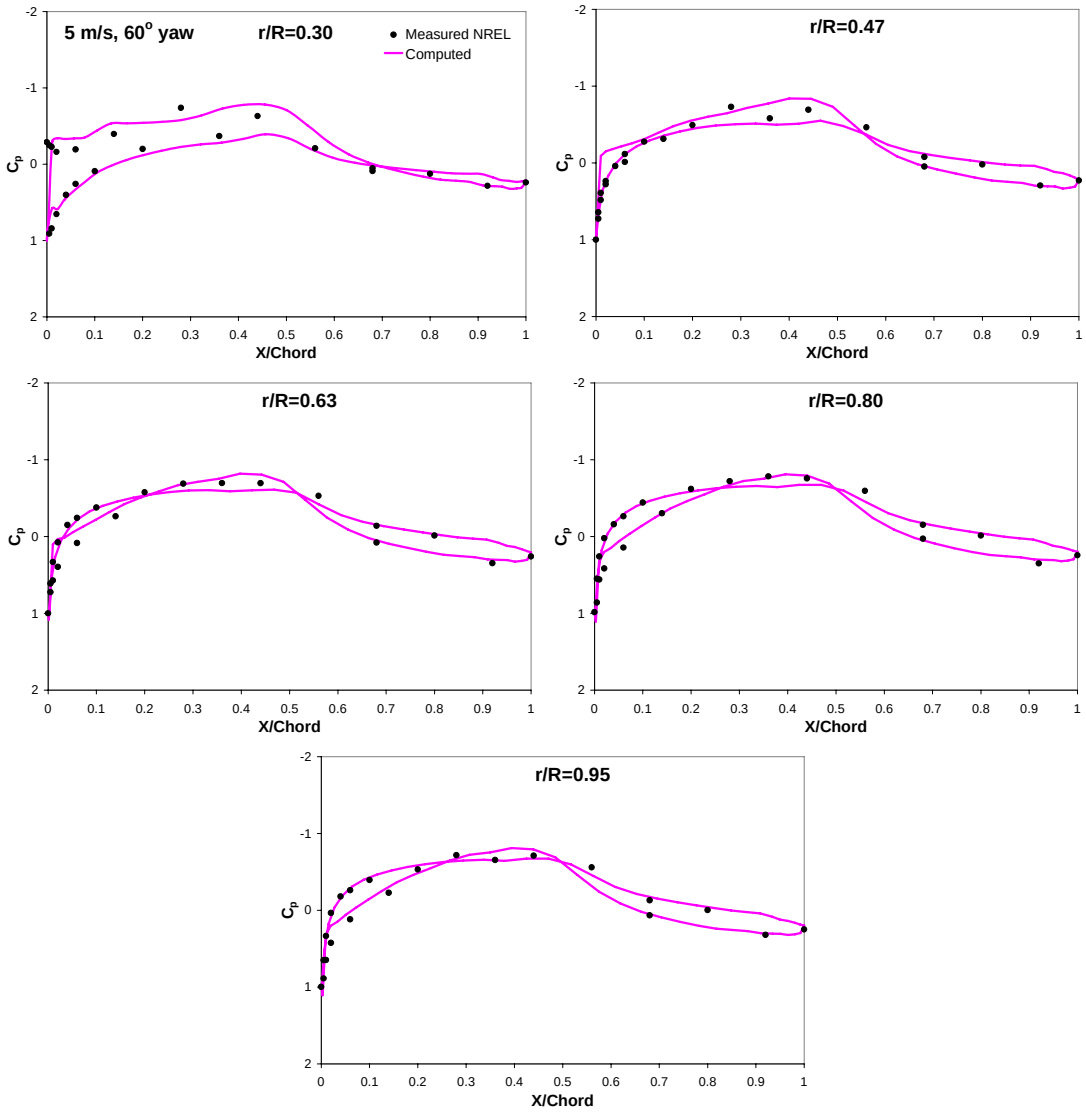

Figure 3.13 Pressure distribution of the 5 m/s and 60° yaw case

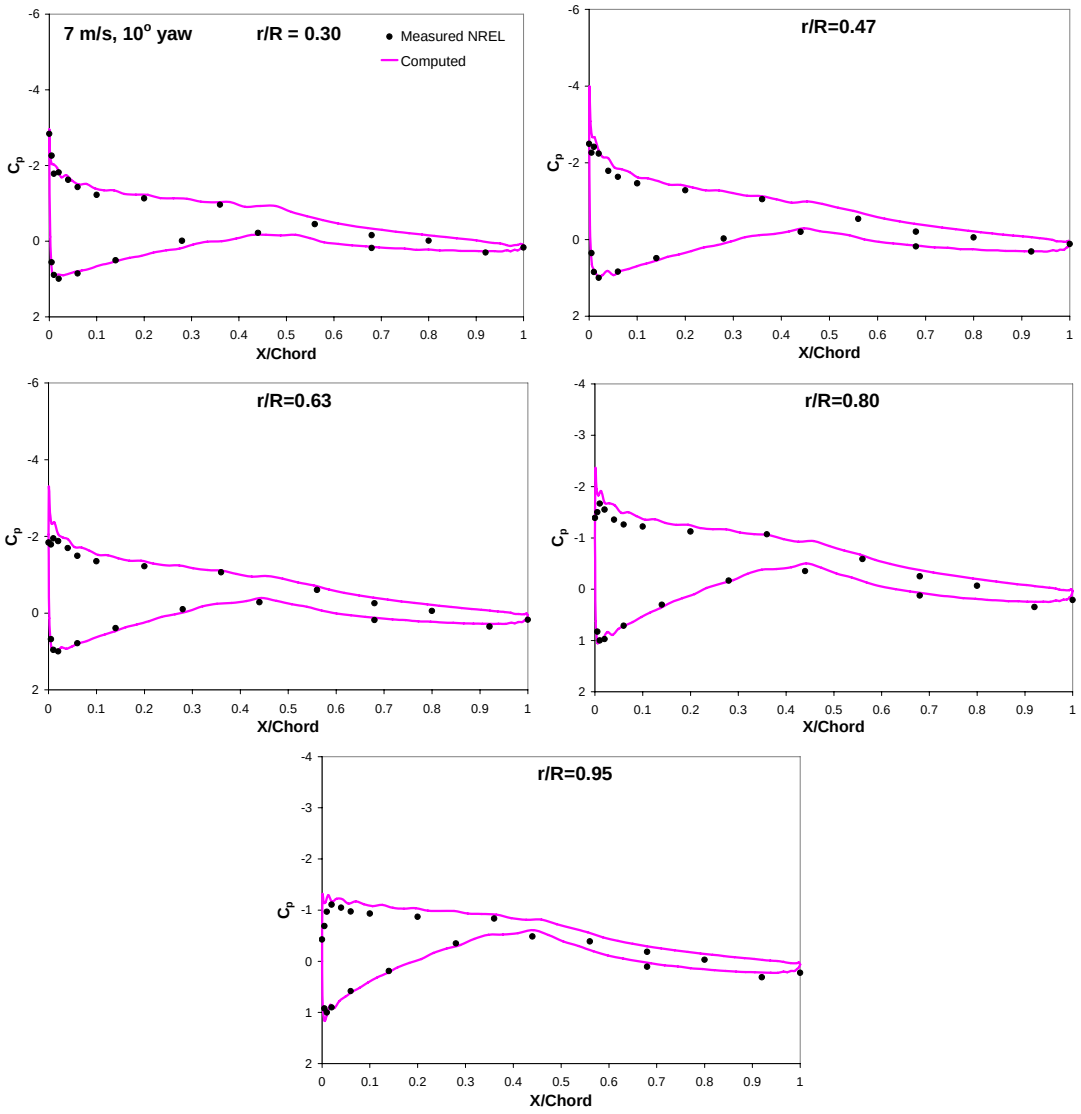

Figure 3.14 Pressure distribution of the 7 m/s and 10° yaw case

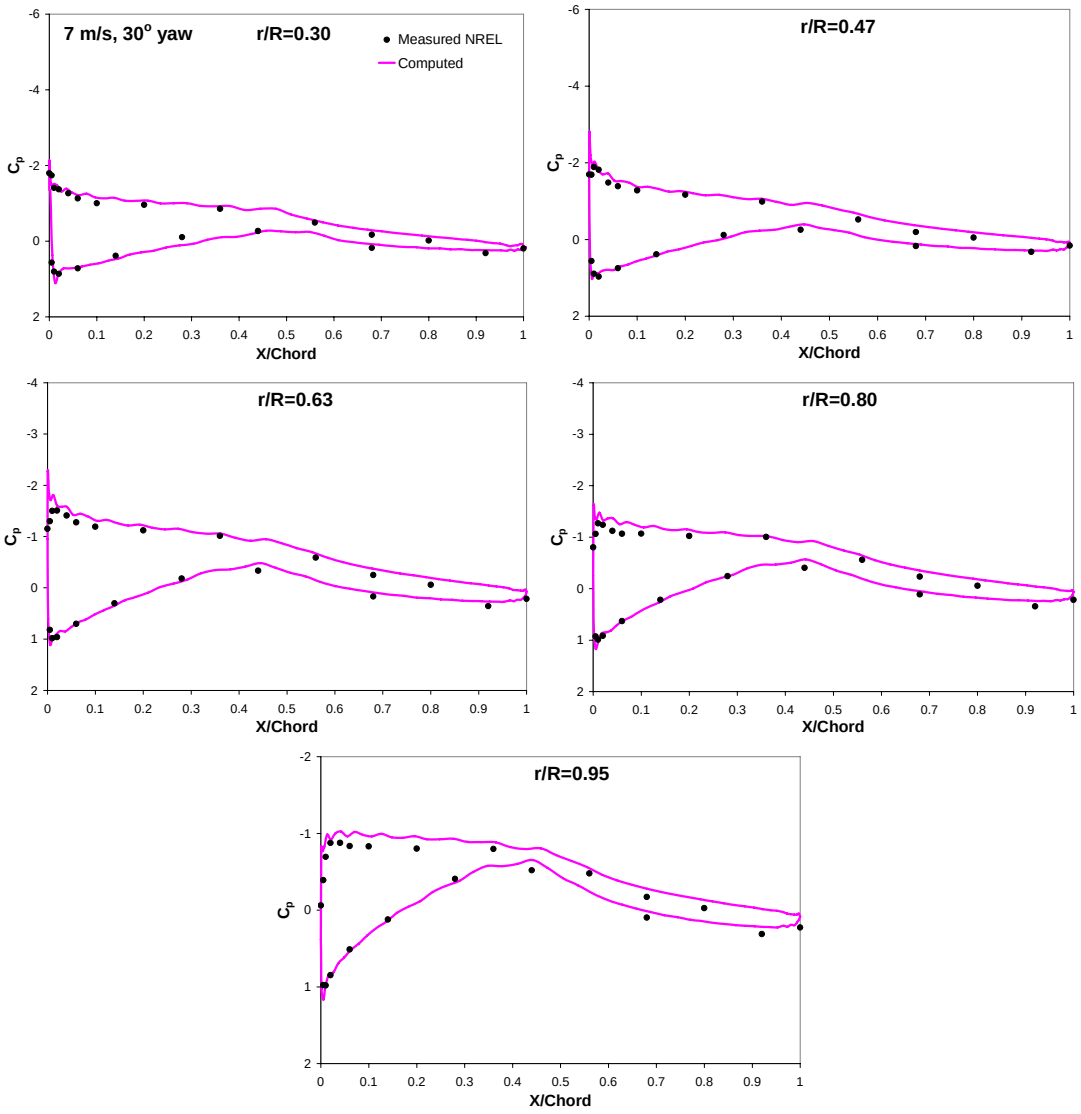

Figure 3.15 Pressure distribution of the 7 m/s and 30° yaw case

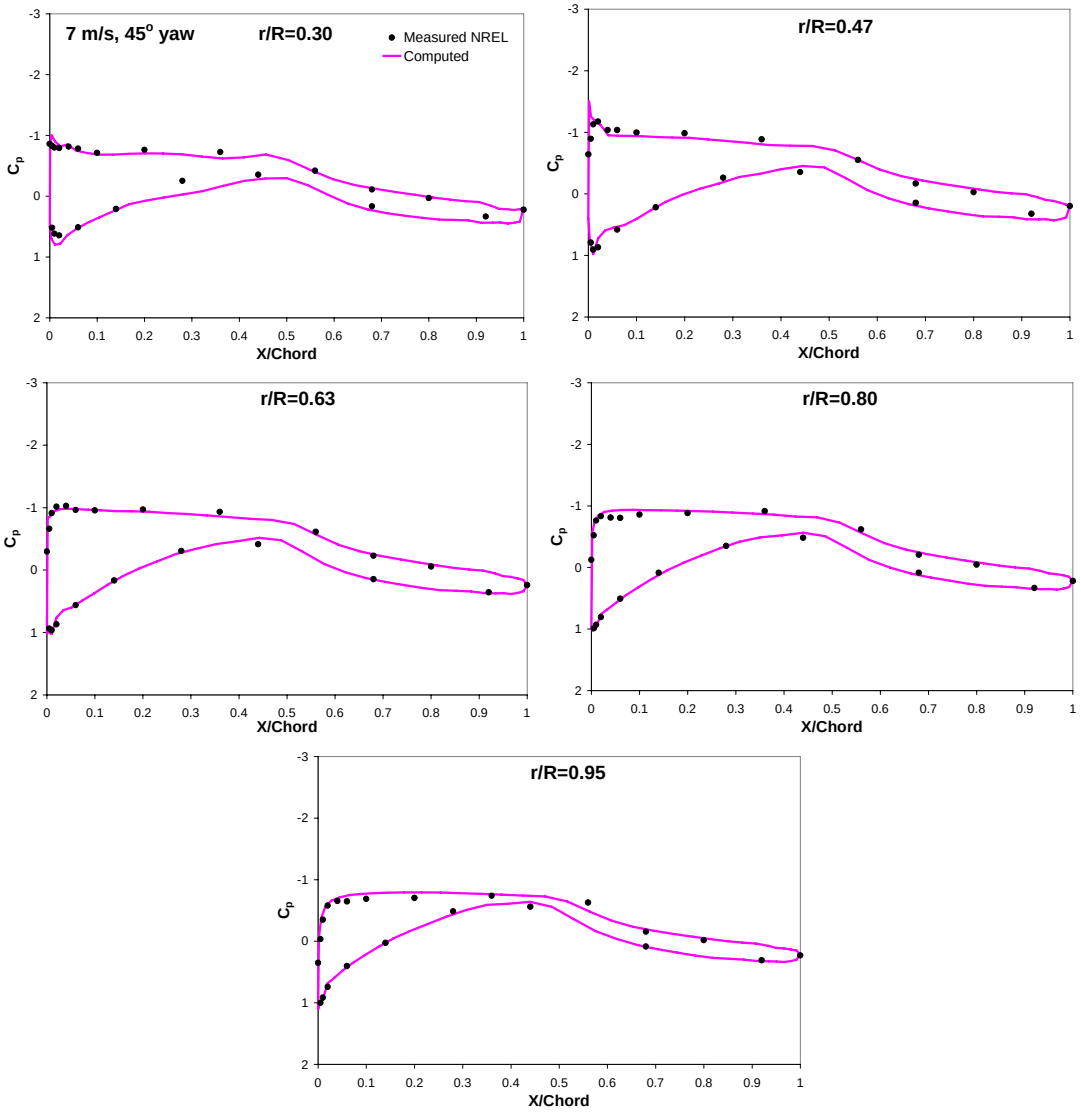

Figure 3.16 Pressure distribution of the 7 m/s and 45° yaw case

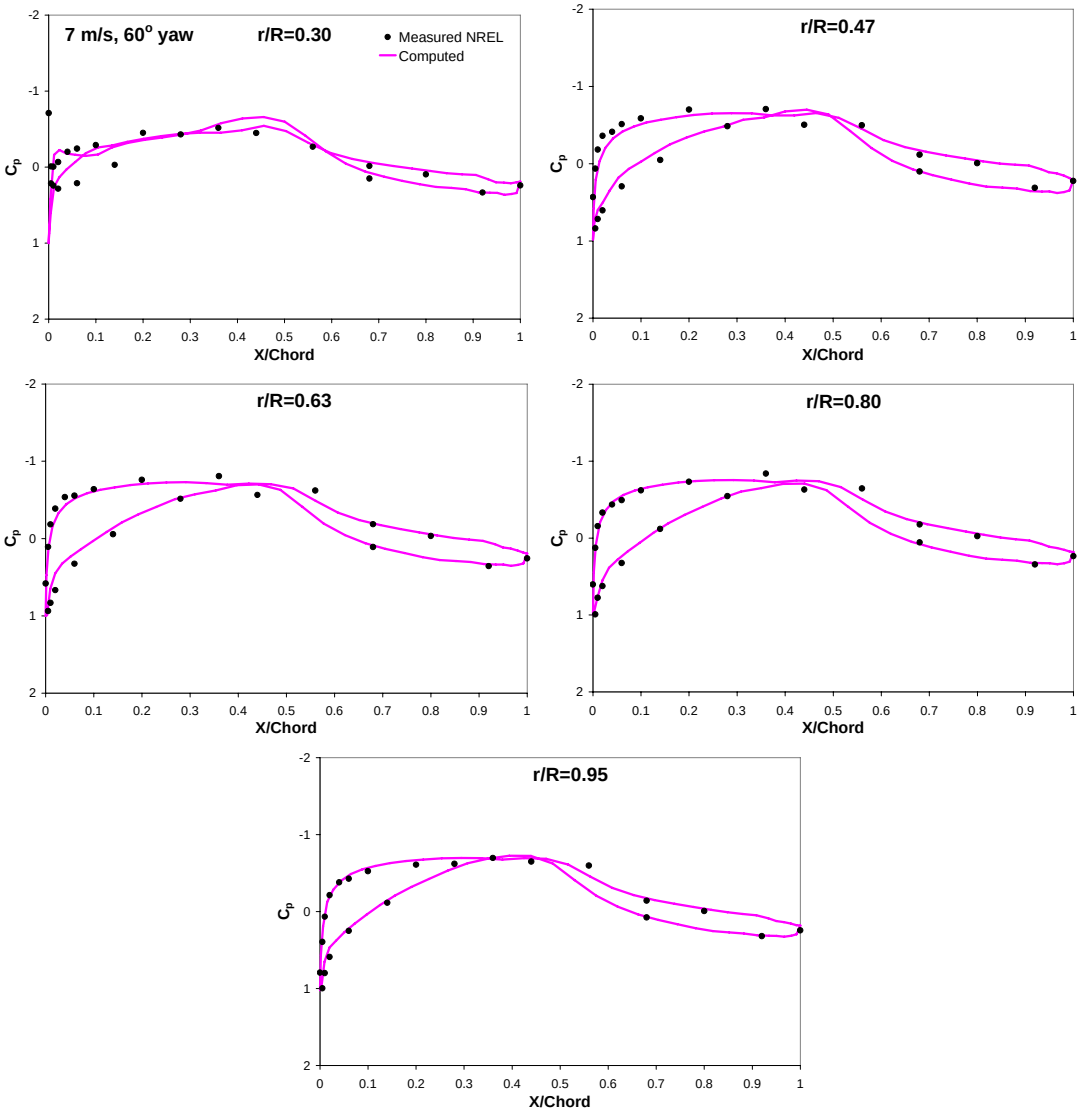

Figure 3.17 Pressure distribution of the 7 m/s and 60° yaw case

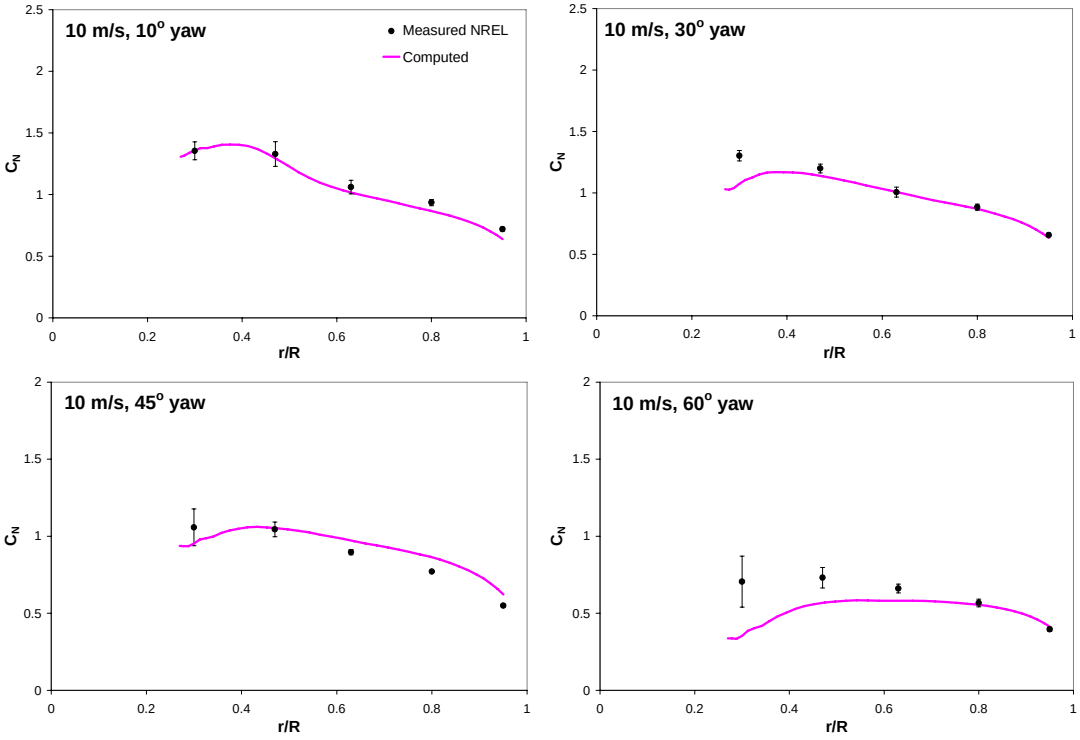

Figure 3.18 Radial distribution of the normal force coefficient C_N at 10 m/s

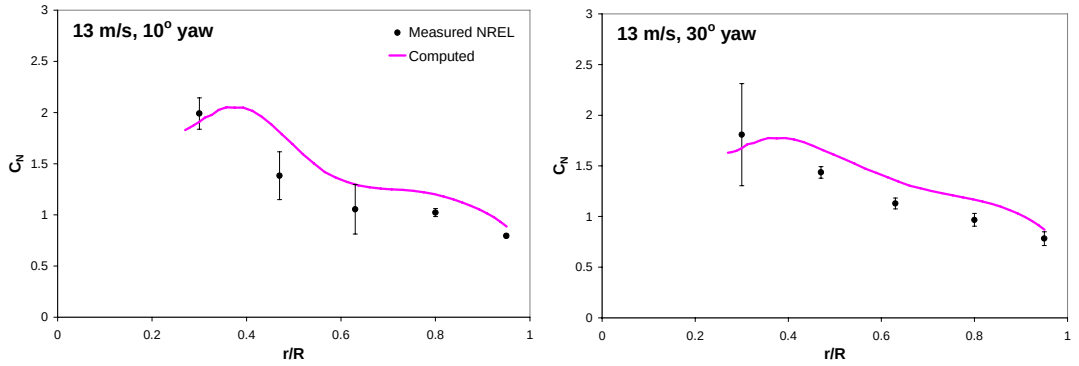

Figure 3.19 Radial distribution of the normal force coefficient C_N at 13 m/s

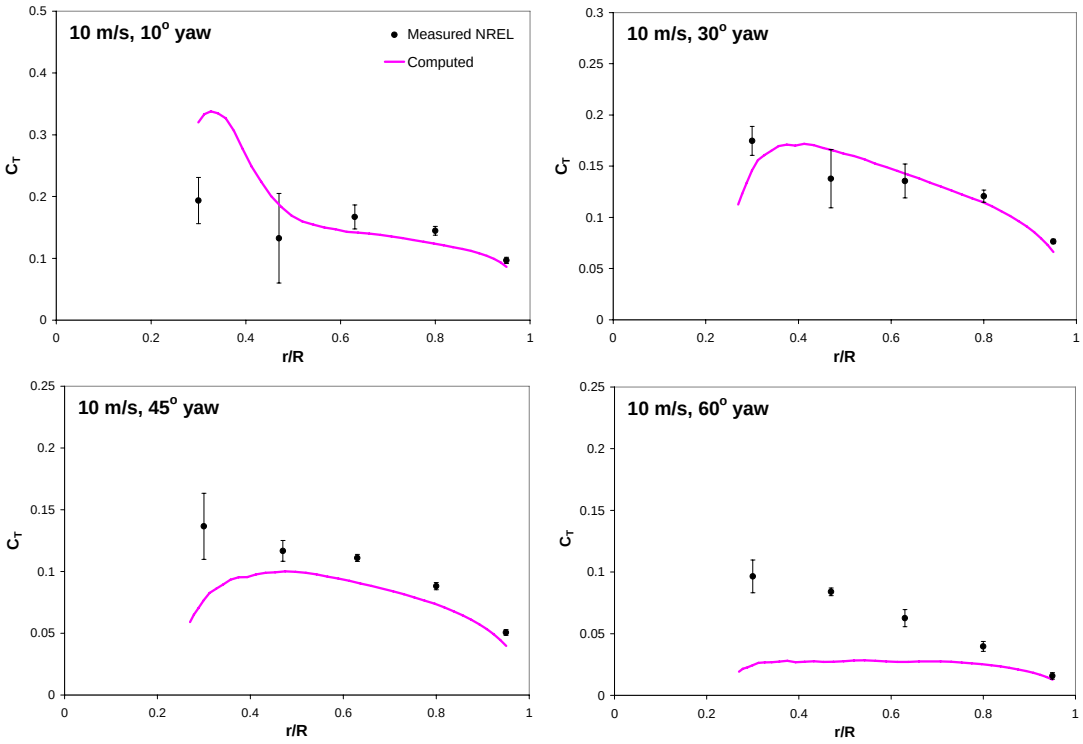

Figure 3.20 Radial distribution of the tangential force coefficient C_T at 10 m/s

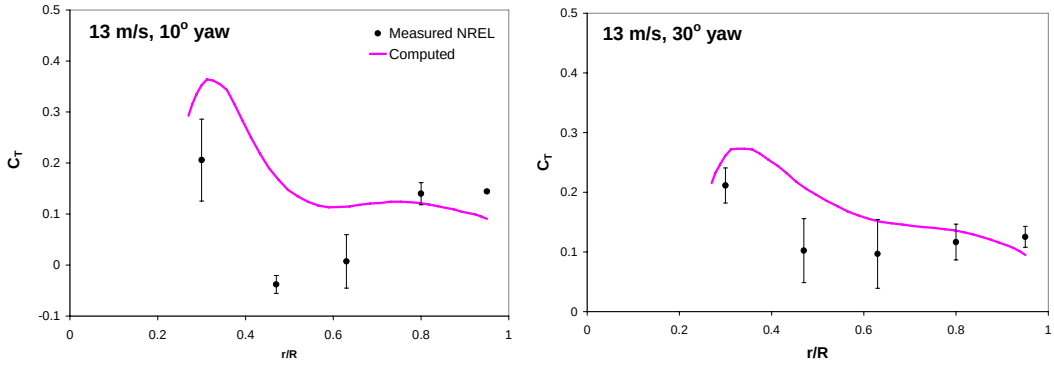

Figure 3.21 Radial distribution of the tangential force coefficient C_T at 13 m/s

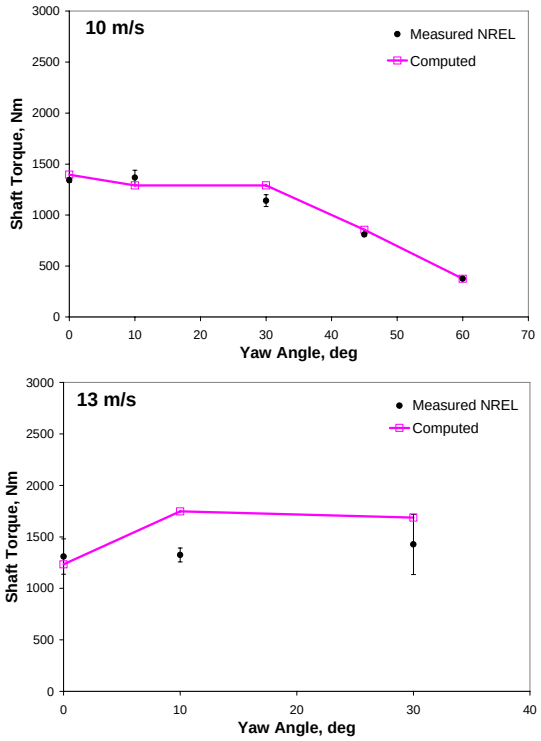

Figure 3.22 Variation of the torque generated by the rotor as a function of yaw angle; at 10 and 13 m/s

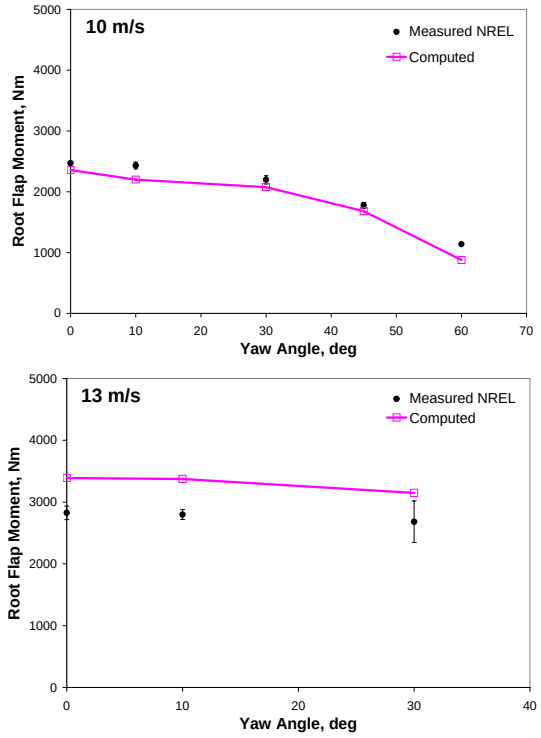

Figure 3.23 Variation of the root flap moment as a function of yaw angle; at 10 and 13 m/s

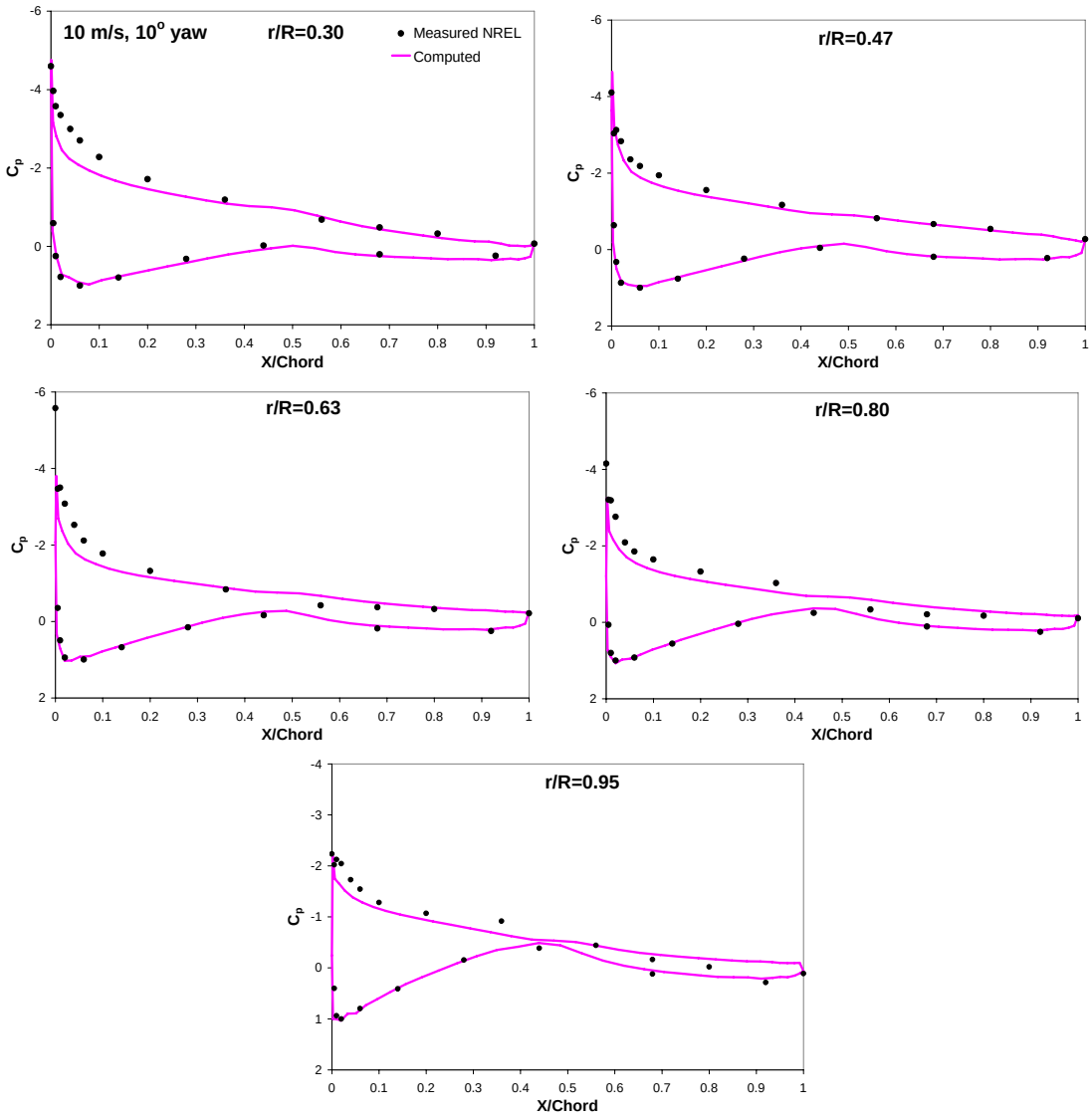

Figure 3.24 Pressure distribution of the 10 m/s and 10° yaw case

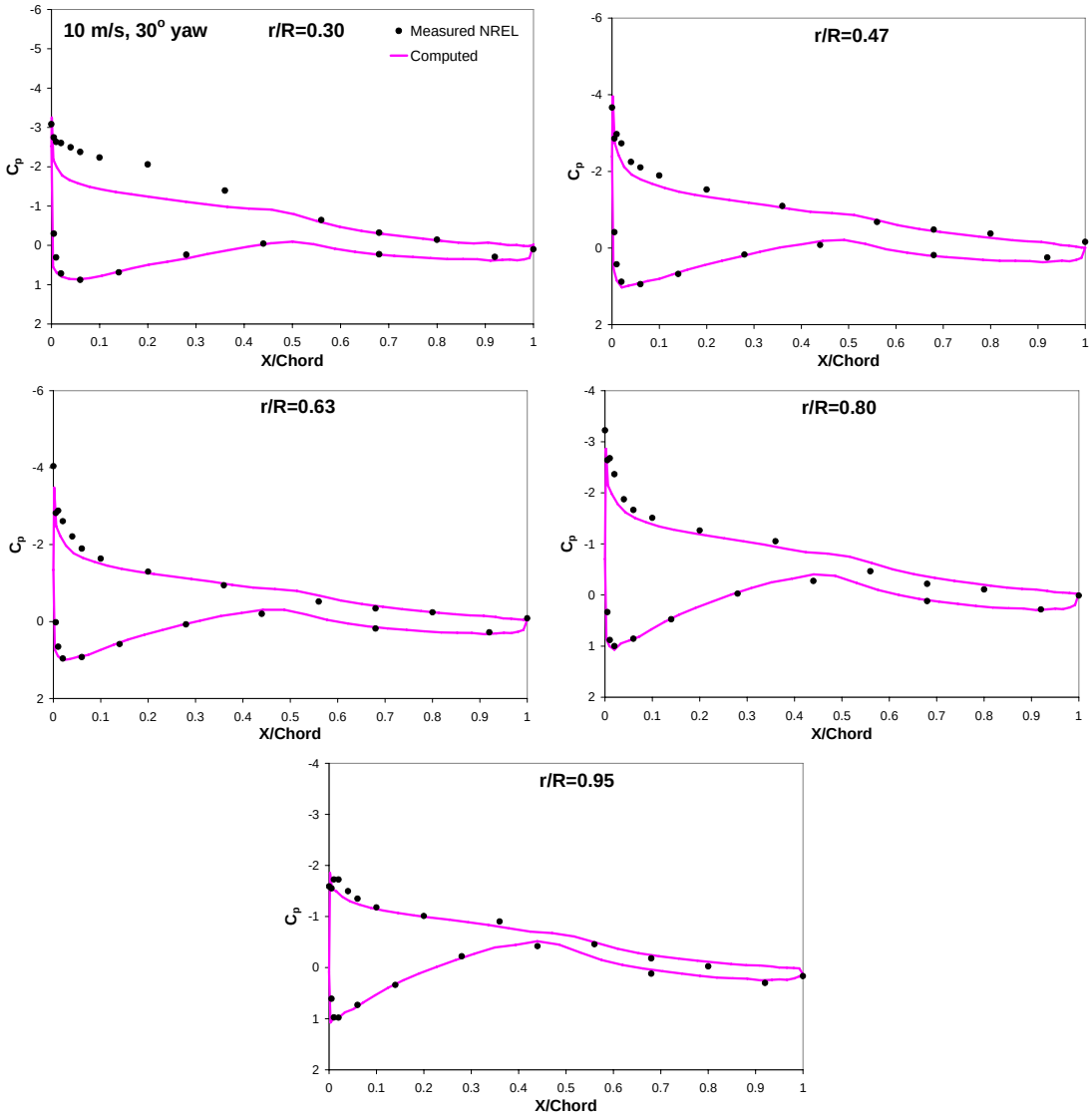

Figure 3.25 Pressure distribution of the 10 m/s and 30° yaw case

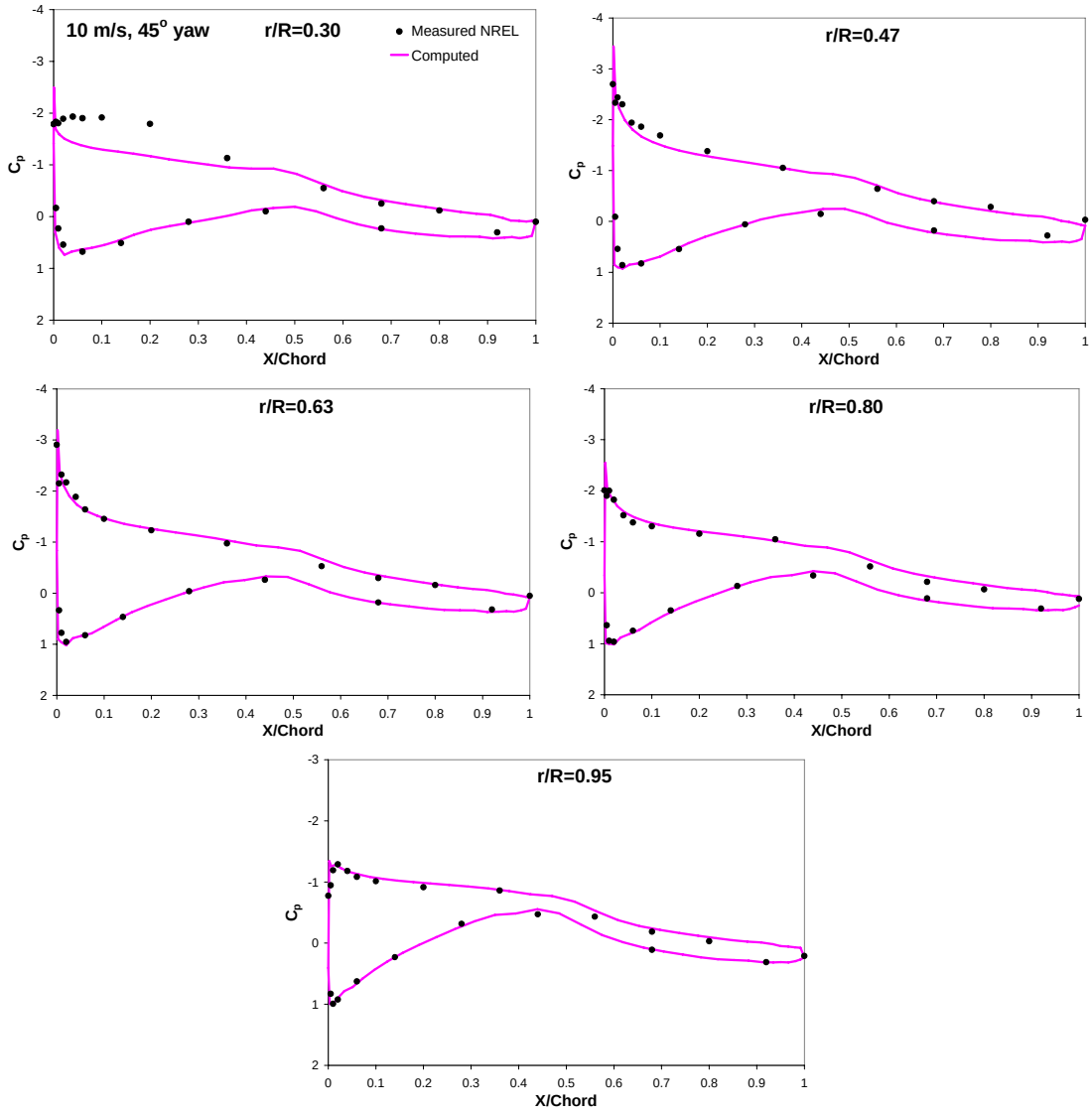

Figure 3.26 Pressure distribution of the 10 m/s and 45° yaw case

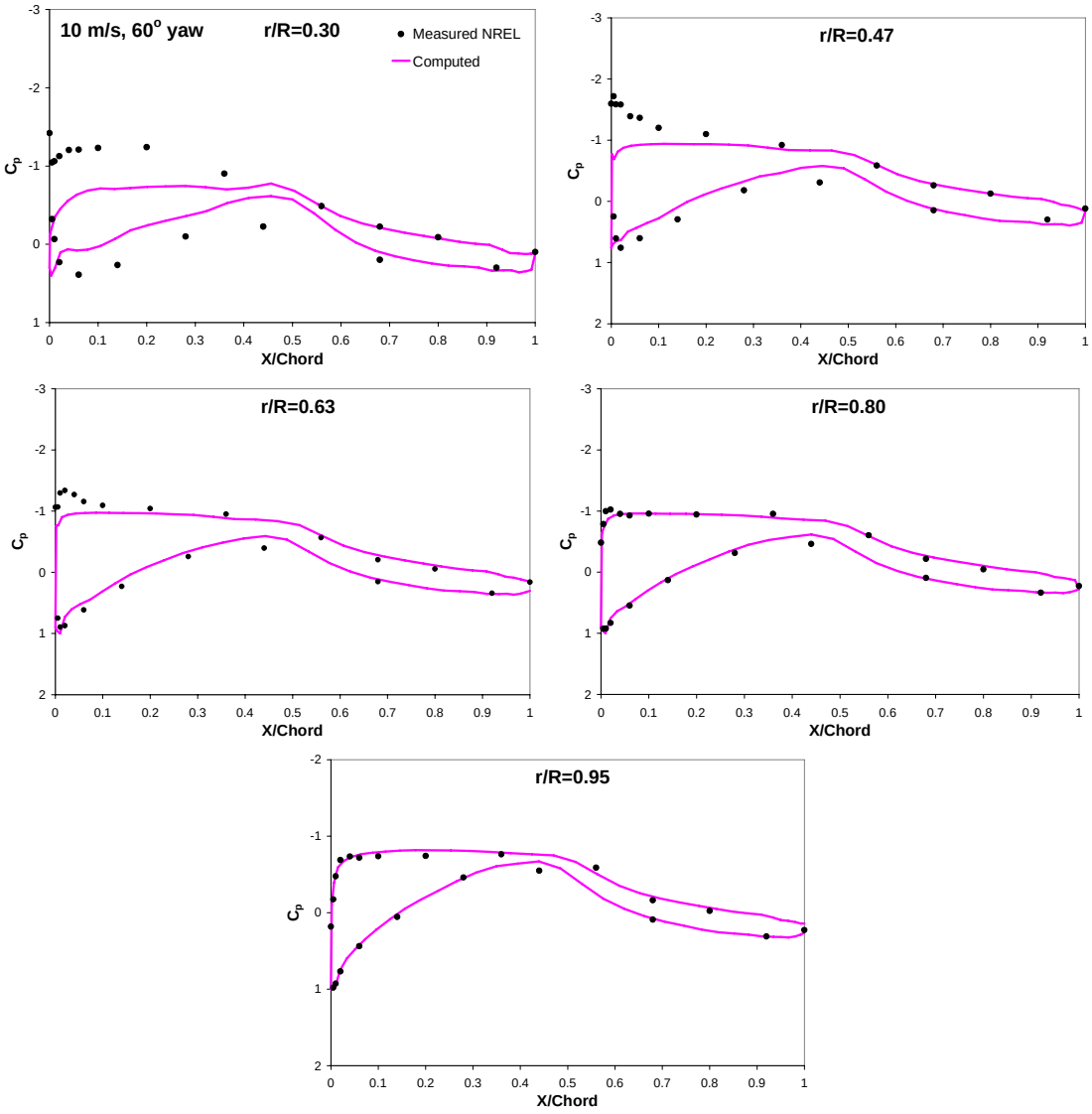

Figure 3.27 Pressure distribution of the 10 m/s and 60° yaw case

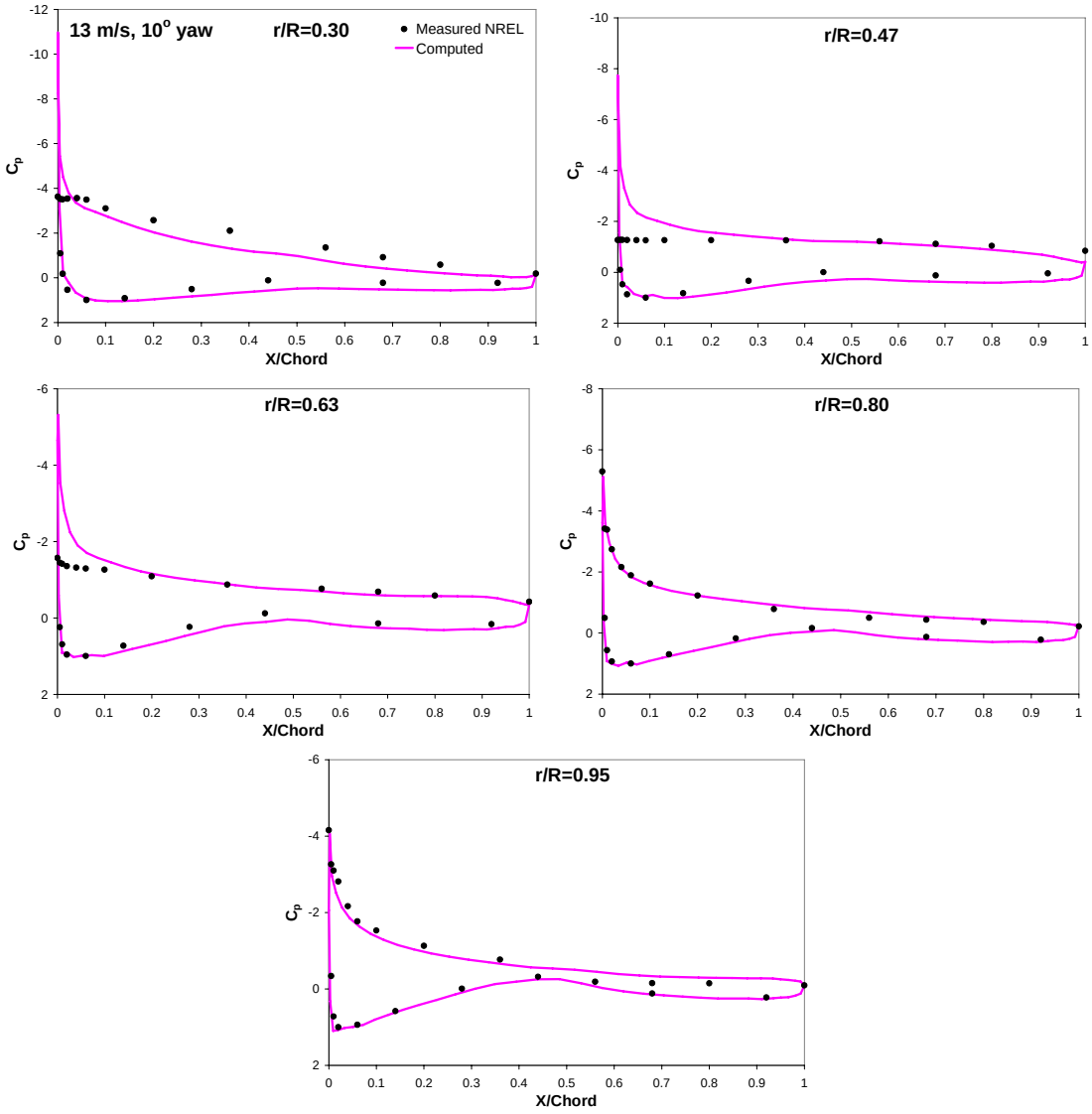

Figure 3.28 Pressure distribution of the 13 m/s and 10° yaw case

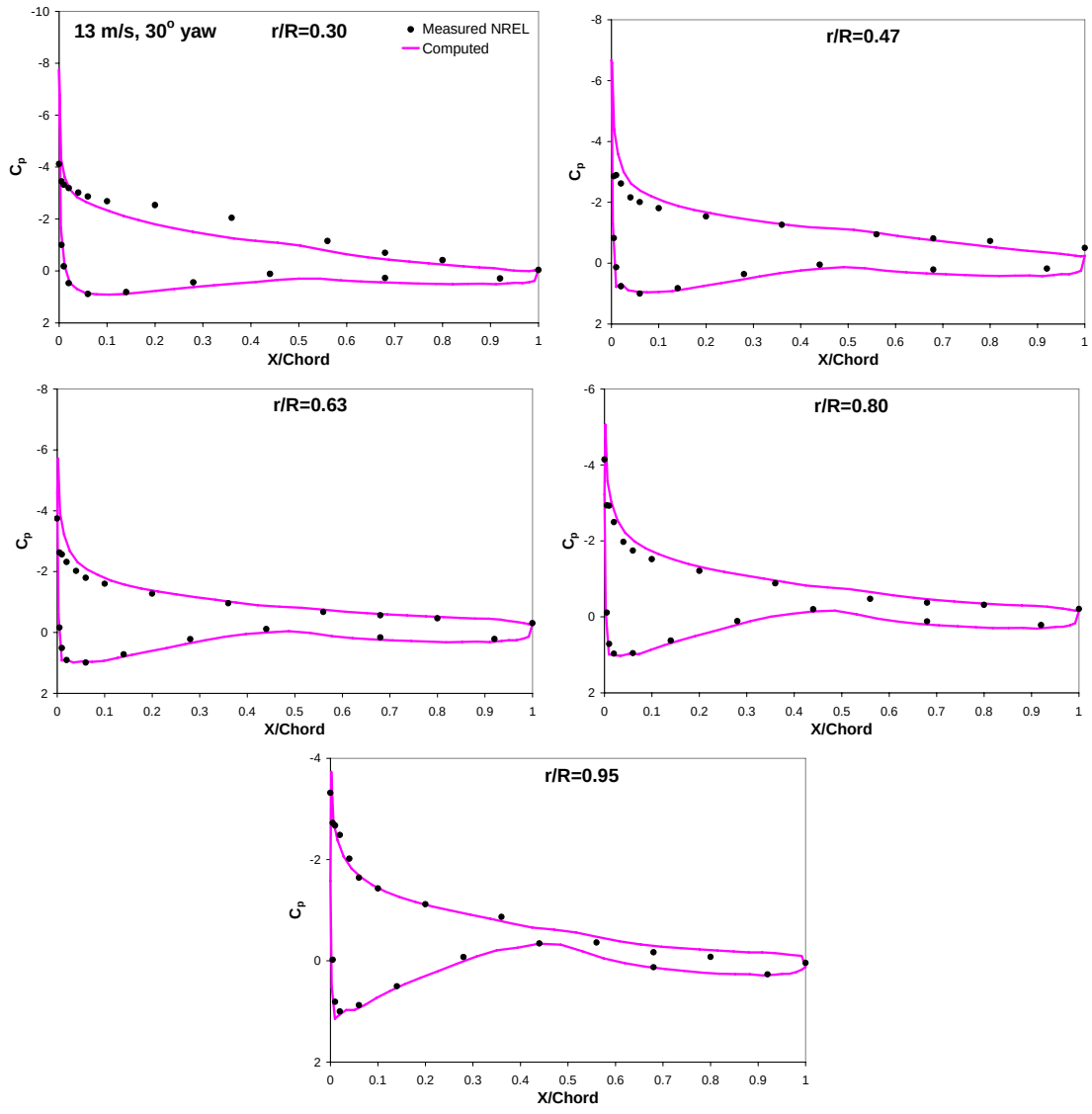

Figure 3.29 Pressure distribution of the 13 m/s and 30° yaw case

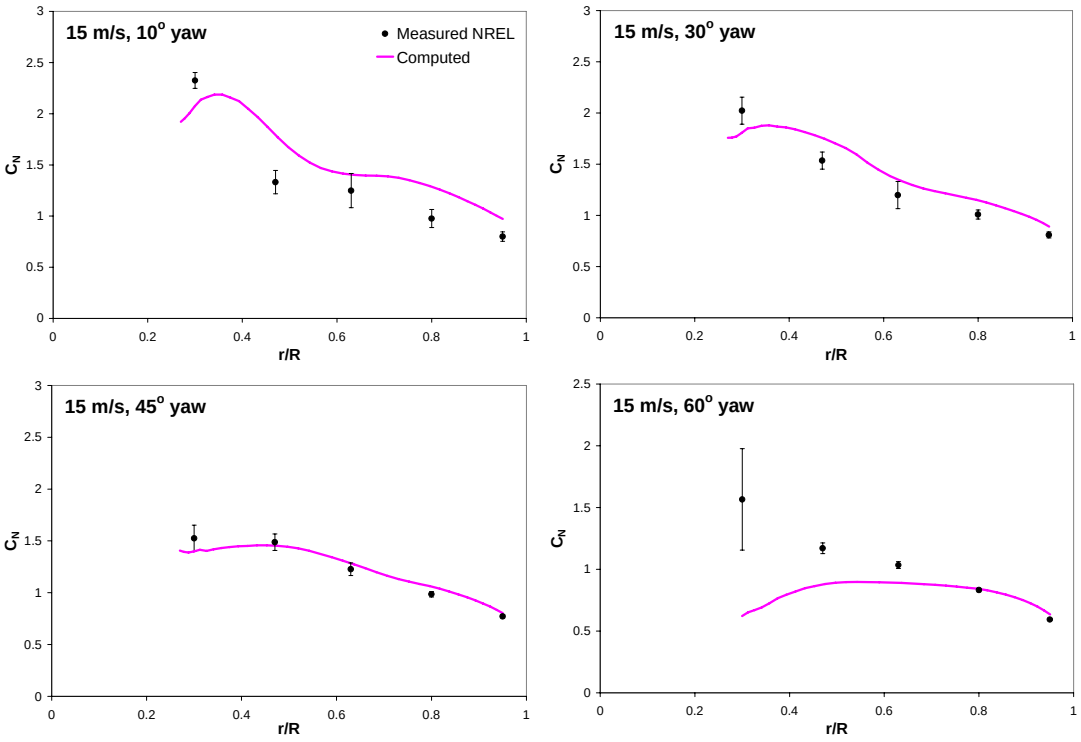

Figure 3.30 Radial distribution of the normal force coefficient C_N at 15 m/s

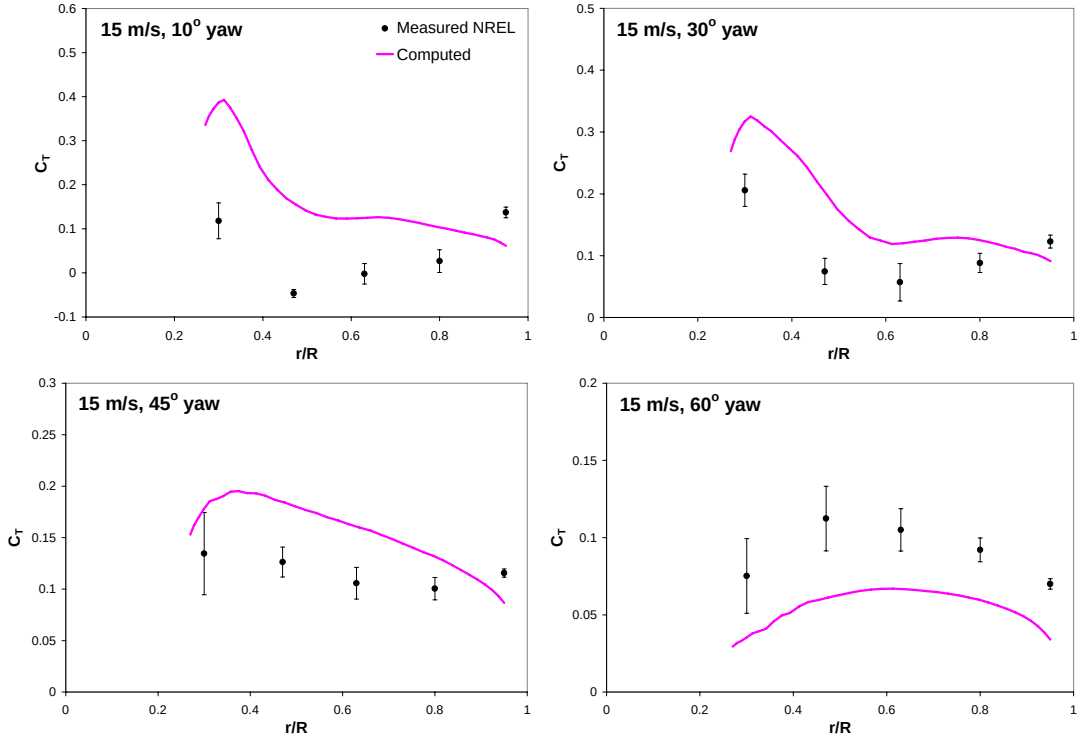

Figure 3.31 Radial distribution of the tangential force coefficient C_T at 15 m/s

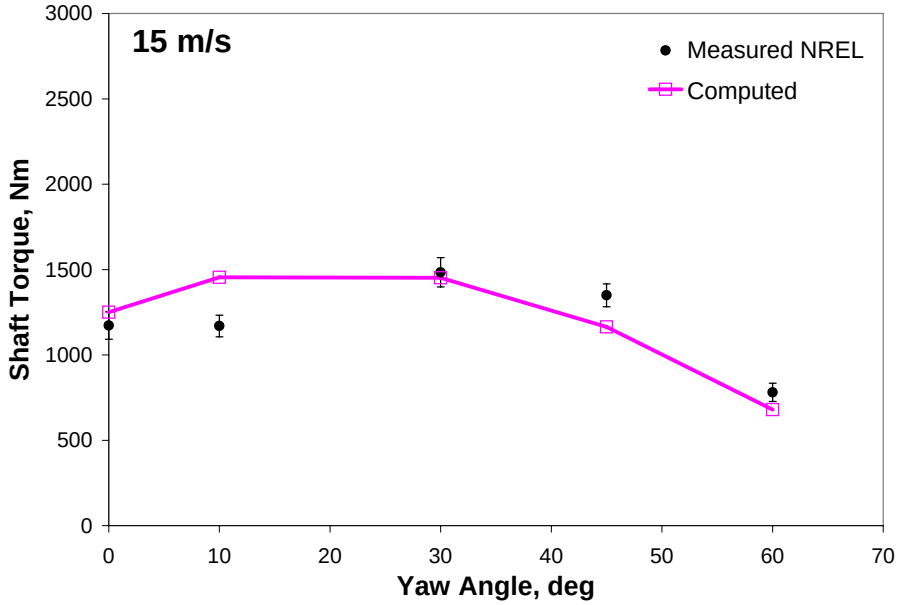

Figure 3.32 Variation of the torque generated by the rotor as a function of yaw angle; at 15 m/s

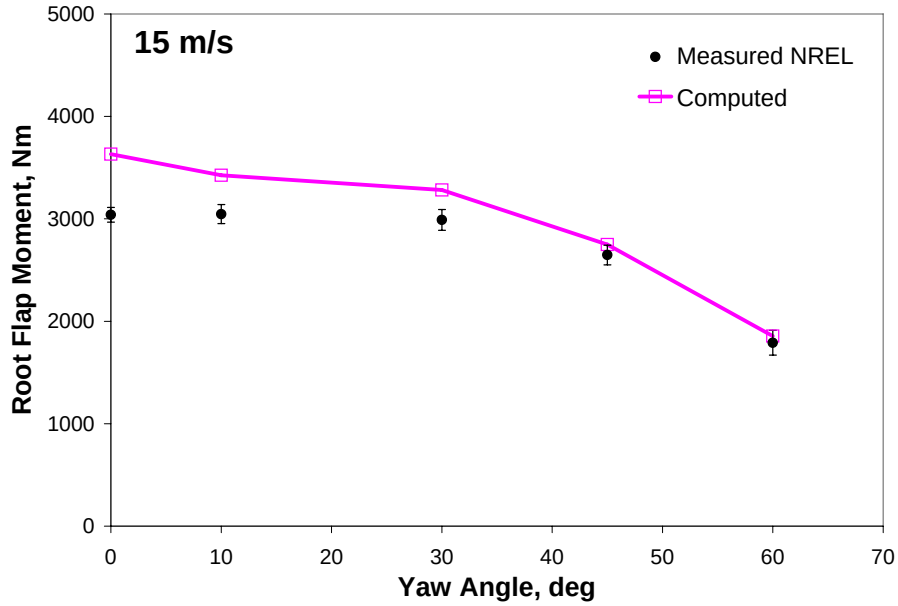

Figure 3.33 Variation of the root flap moment as a function of yaw angle; at 15 m/s

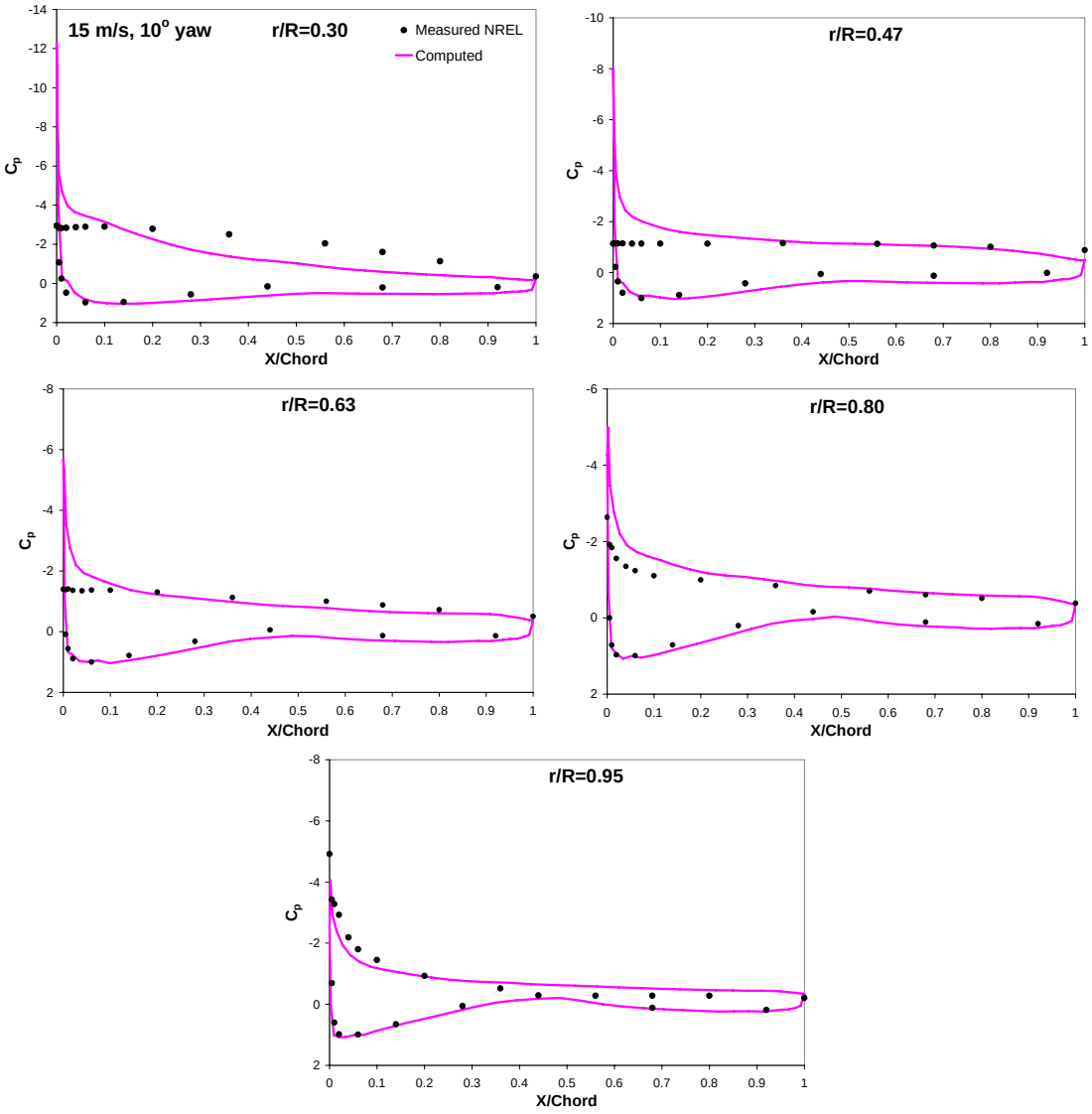

Figure 3.34 Pressure distribution of the 15 m/s and 10° yaw case

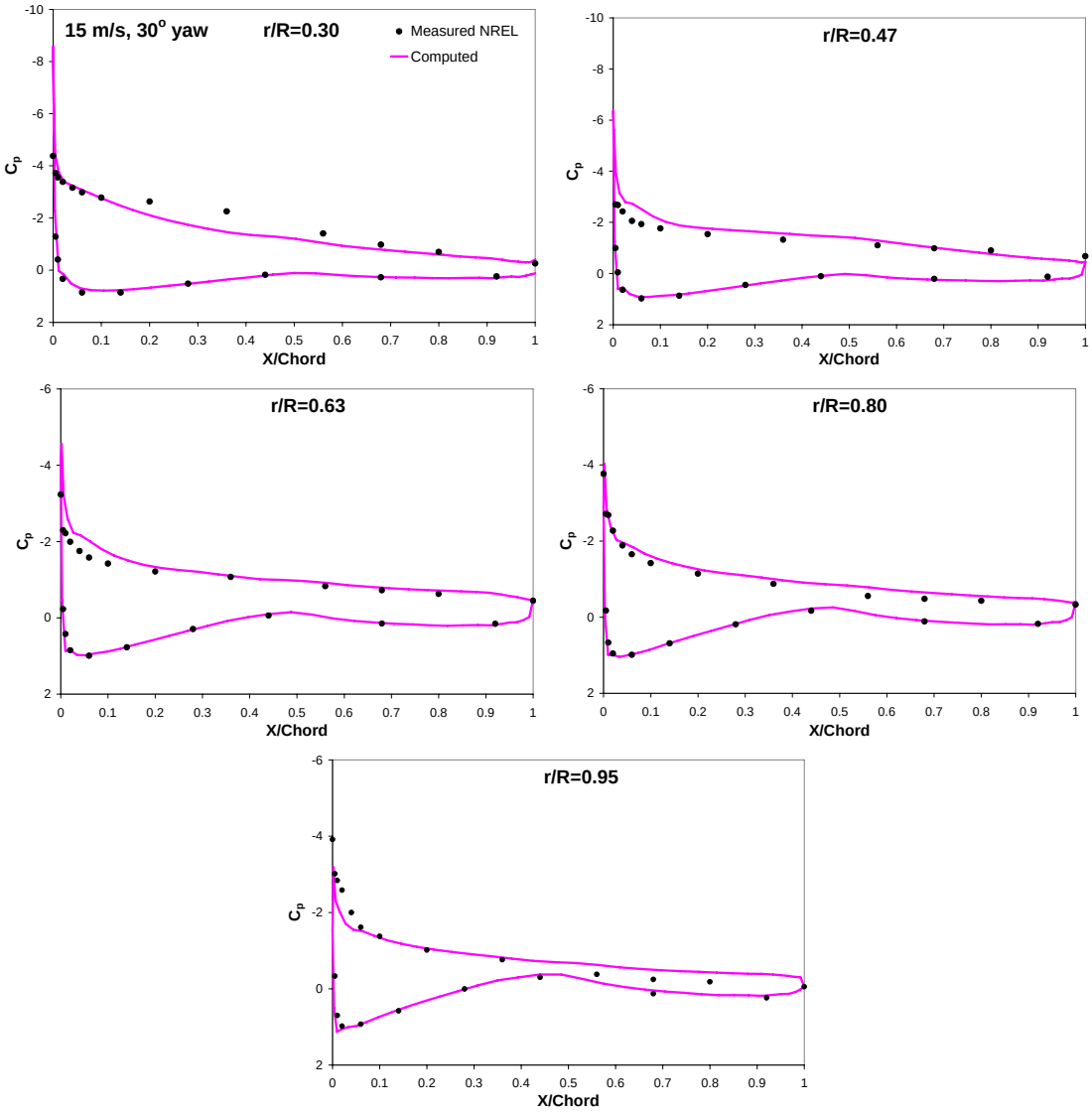

Figure 3.35 Pressure distribution of the 15 m/s and 30° yaw case

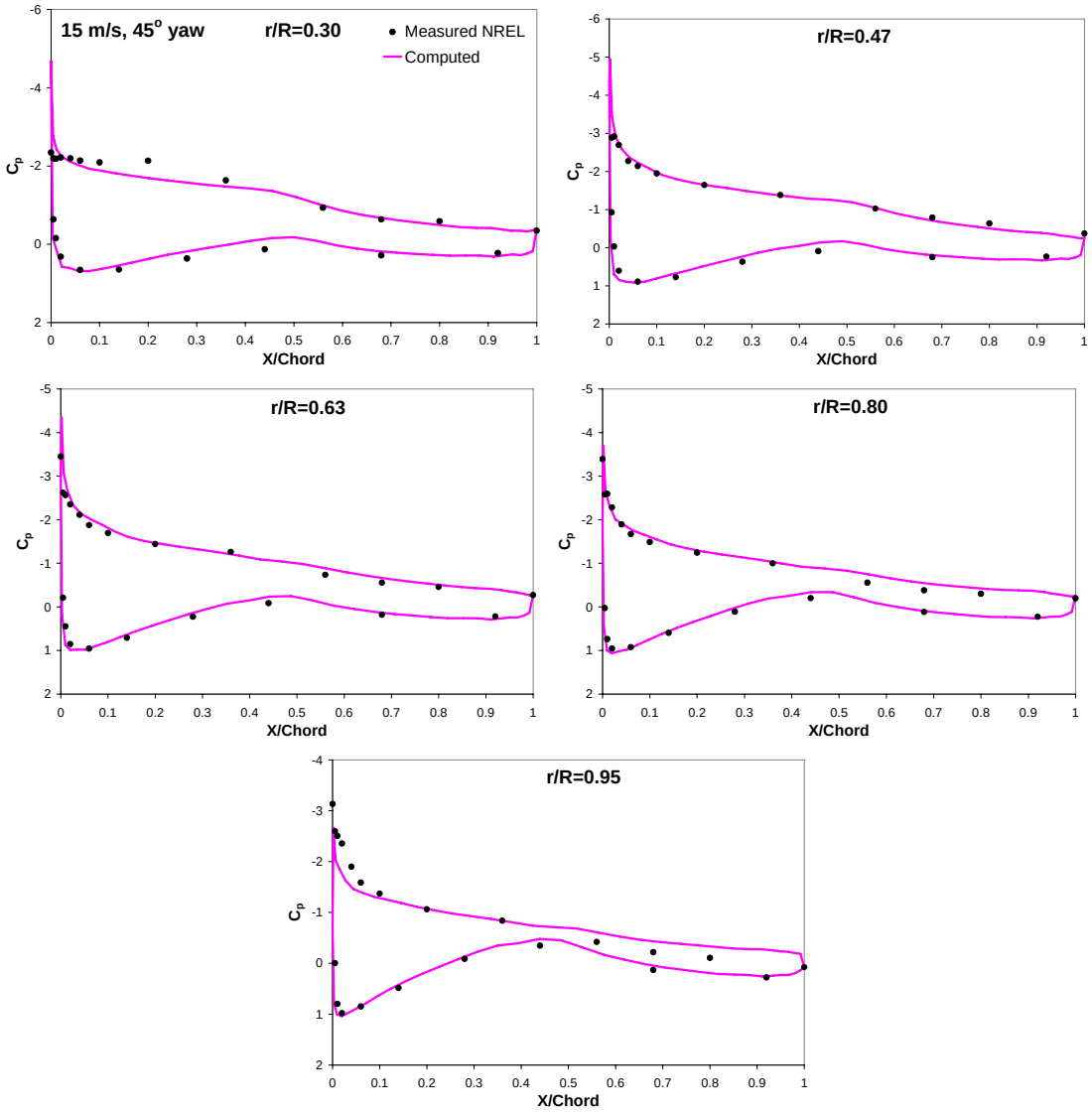

Figure 3.36 Pressure distribution of the 15 m/s and 45° yaw case

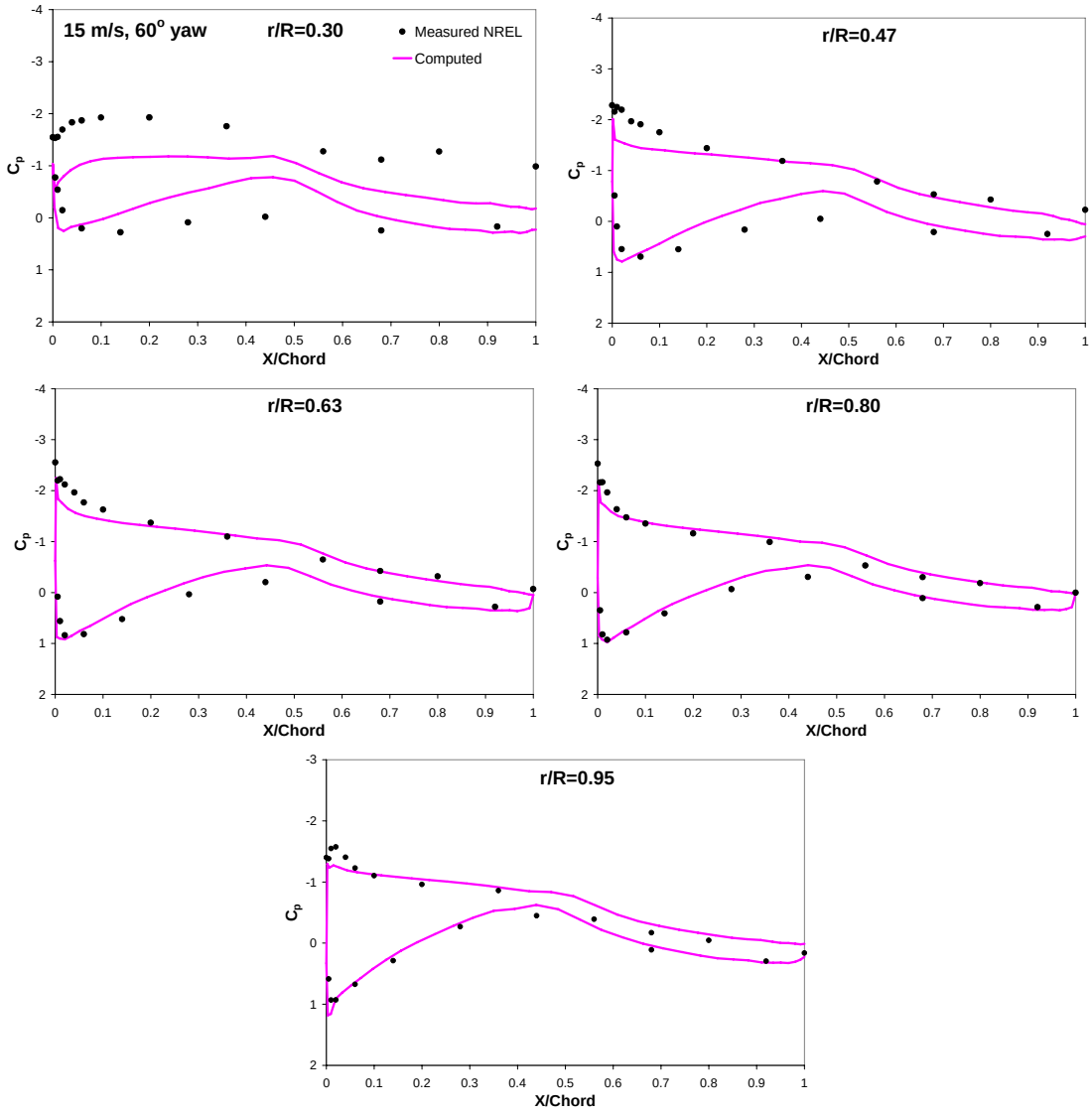

Figure 3.37 Pressure distribution of the 15 m/s and 60° yaw case

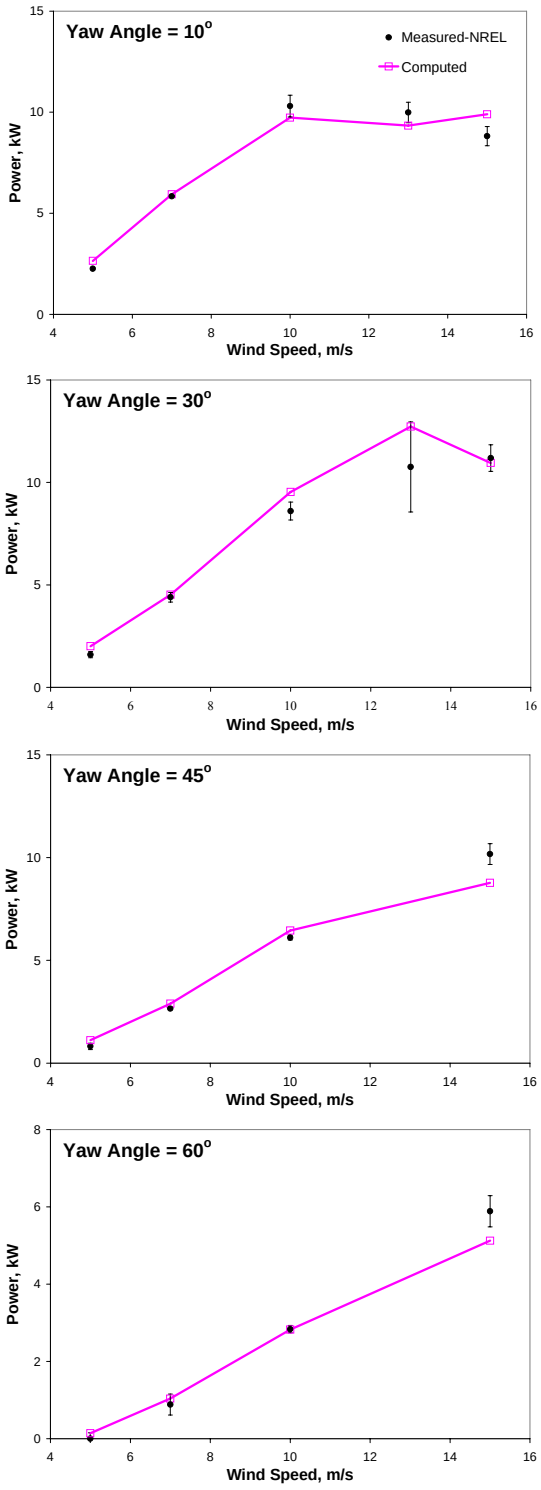

Figure 3.38 Comparison of computed and measured rotor power

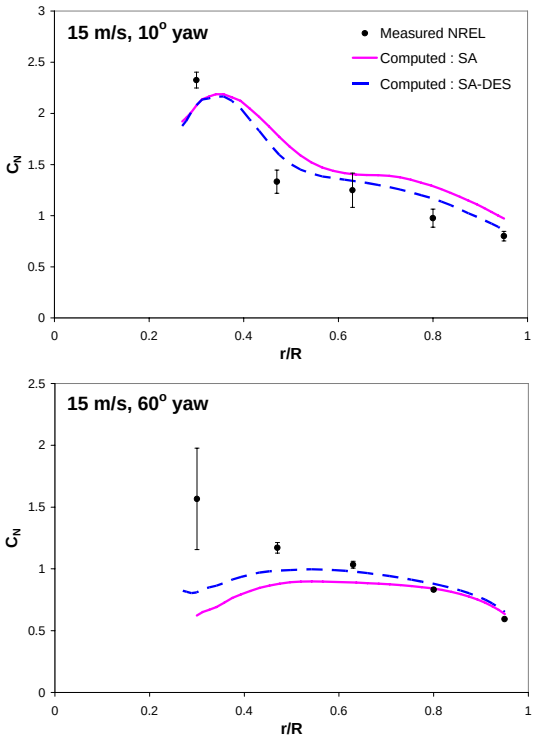

Figure 3.39 Radial distribution of the normal force coefficient C_N at 15 m/s; 10° and 60° yaw (Effect of SA-DES model)

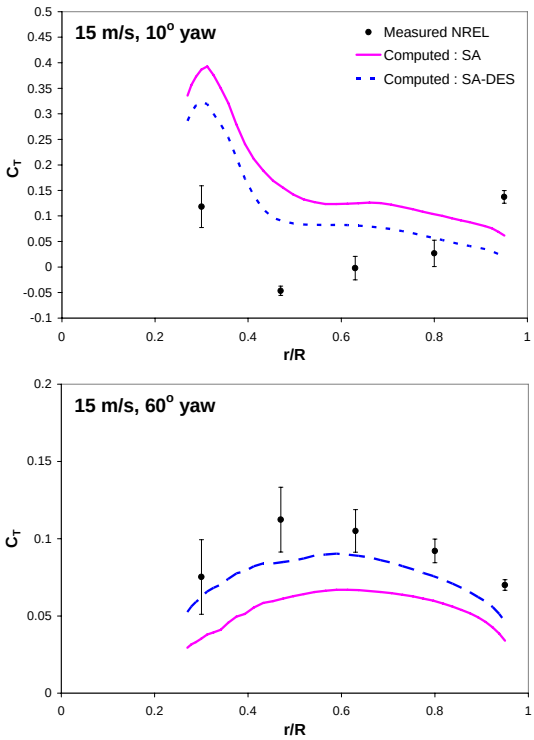

Figure 3.40 Radial distribution of the tangential force coefficient C_T at 15 m/s; 10° and 60° yaw (Effect of SA-DES model)

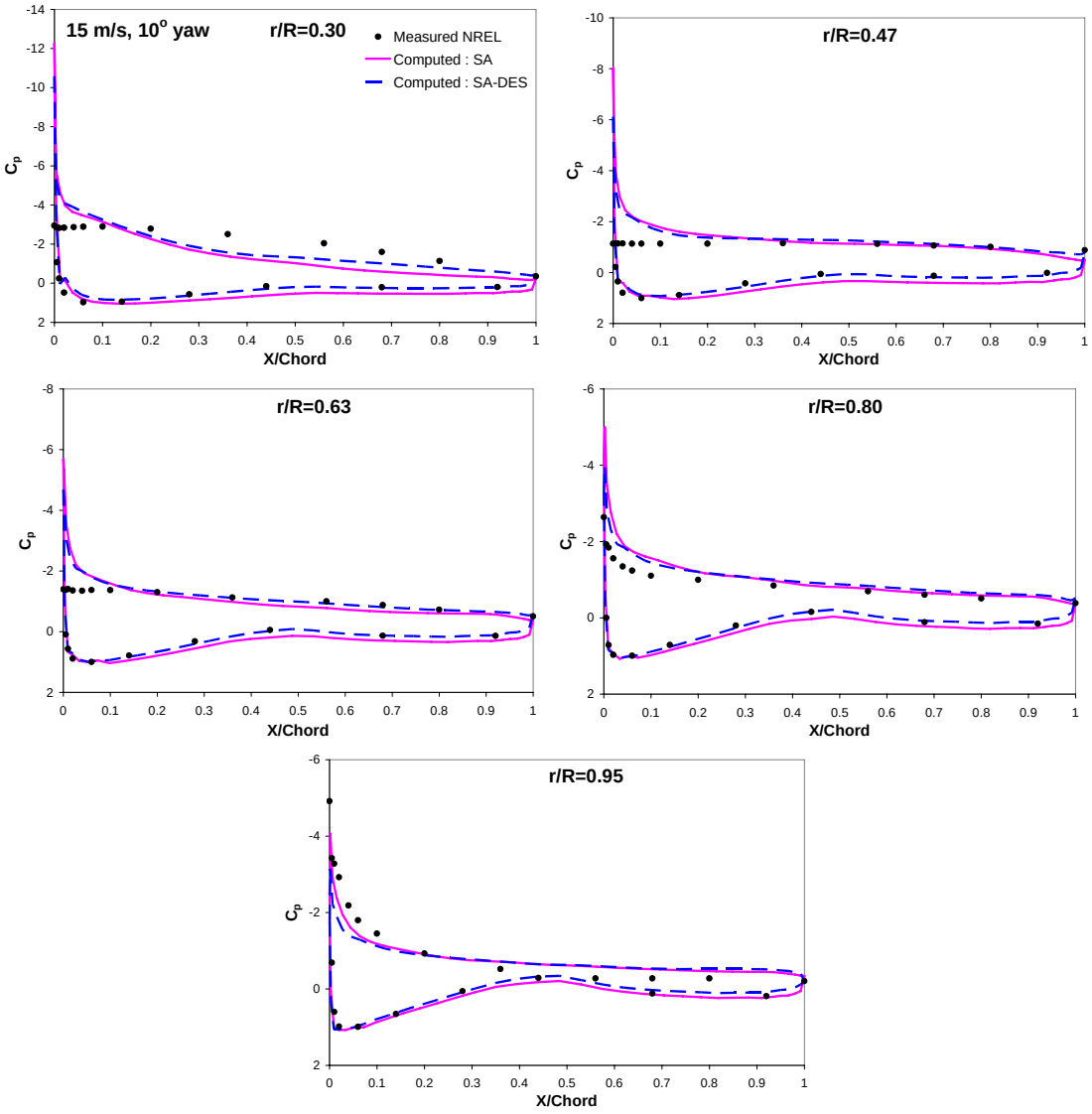

Figure 3.41 Pressure distribution of the 15 m/s and 10° yaw case (Effect of SA-DES model)

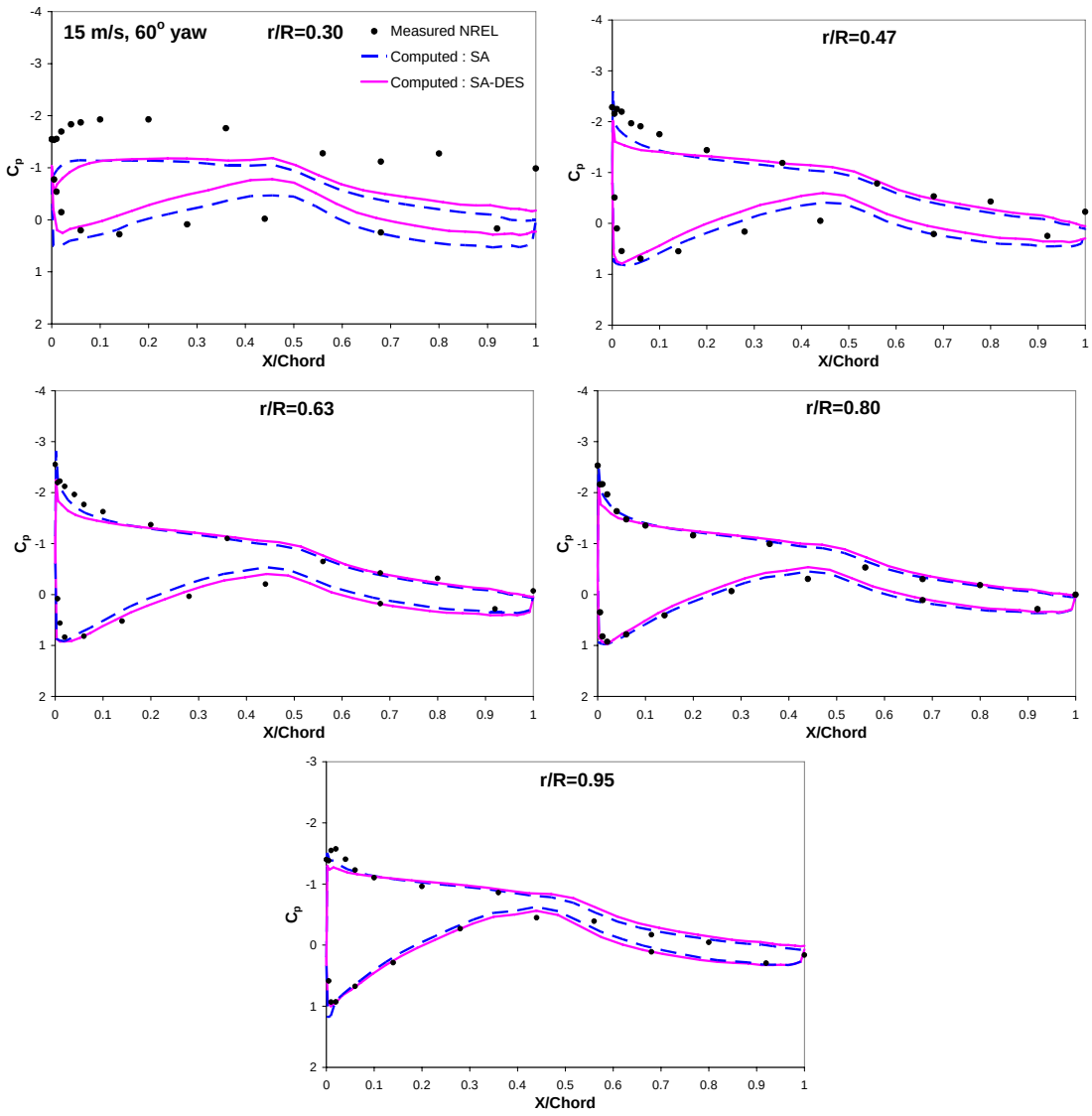

Figure 3.42 Pressure distribution of the 15 m/s and 60° yaw case (Effect of SA-DES model)

CHAPTER 4

RESULTS OF ACTIVE CIRCULATION ENHANCEMENT CONCEPT: BLOWING JET

As stated in the introduction, the performance of a wind turbine is greatly dependent on the lift-to-drag ratio of the airfoil sections. Laminar airfoils such as S809 are often used because they have a low drag coefficient compared to conventional airfoils such as NACA 0012 with large amounts of turbulent flow over surface. A second possibility is to increase C_l using passive or active techniques, while retaining C_d to be low.

In this chapter, the flow solver validated in the previous chapter is used to investigate the aerodynamic performance of a wind turbine rotor equipped with circulation control technology (blowing jet or Gurney flap). The highly beneficial impact to lift-to-drag ratio from using the Coanda jet can be seen in Ref. [26]-[28] and provided the motivation for investigating this technology in this study. Computational results are compared with the baseline rotor results discussed in the previous chapter to assess the benefits of the circulation control technology.

Computations have been carried out at selected wind speeds representing both low and high wind speed regimes. The effects of the jet slot height on the performance of the Coanda jet have been investigated. Finally the effect of pulsed blowing jet and the performance of the leading edge blowing have been studied.

4.1 Computational Grid

The computational grid used for baseline rotor analysis in the previous chapter is also used here with a dense grid near the slot and in the vicinity of trailing edge. In this study, the jet slot is located at 93% of chord on the upper surface of the rotor and the jet slot height is nominally 0.2% of chord. In the present work, the jet slot runs along the entire span of the blade. The grid generator is general enough so that one can easily vary the jet slot location and size. The grid near the rotor surface and the jet slot is shown in Figure 4.1.

In contrast to conventional rounded trailing edge circulation control airfoils, the present configuration retains the flat lower surface of the S809 airfoil, and relies on upper surface curvature for the Coanda effect. It should be mentioned that the jet itself and the blunt trailing edge with a thickness of approximately 1 mm or more can cause some noise problems [109].

The construction of a high quality grid around the circulation control airfoil is made difficult by the presence of a small jet slot. In the present study, an approach of treating the jet slot as a grid-aligned boundary (Liu [27]) is used as guidance, with the jet slot boundary condition described in Section 2.5.

4.2 Test Conditions

Calculations have been obtained for the NREL Phase VI rotor at two wind speeds (7 and 15 m/s); at three yaw angles (0, 10, and 30 degrees). The jet momentum coefficients C_μ used in this work range from 0 to 0.10. The reference values for these simulations are: freestream temperature T_∞ = 284 K, freestream density ρ_∞ = 1.225 kg/m^3 and reference chord length c = 0.483 m.

The assessment of the present method was done by comparing the predictions with the following measurements: (a) radial variation of the normal force coefficient C_N and tangential force coefficient C_T; (b) variation of time-averaged torque generated by the rotor as a function of yaw angle and wind speed; (c) time-averaged root flap moment variation as a function of wind speed and yaw angle; (d) surface pressure distributions at selected radial sections; (e) azimuthal variations of C_N and C_T. Flow visualization data, in the form of streamlines have also been done. In all the figures of streamlines shown in this work, the rotor was moving from the right to the left, and the wind direction is directed upwards perpendicular to the rotor disk.

Because the present analysis is time accurate, it yields time histories of the entire flow field, and engineering quantities of interest such as sectional normal and tangential force coefficients as a function of time. Typical results are shown in Figure 4.2 and 4.3. It is clearly seen that the model is capable of simulating the unsteady flow details, and agrees well with measured data for $C_\mu = 0$ (unblown case). However, in most instances, time-averaged quantities, averaged over multiple revolutions are of the most interest. For this reason, from now on, only the time averaged quantities are presented and discussed.

4.3 Circulation Control Results for Low Wind Speed Conditions

Results at a low wind speed of 7 m/s for yaw angles up to 30 degrees are presented first. At these conditions, a visualization of the computed flow indicates that the flow is well-behaved and attached over much of the rotor. Therefore, on the present grid and the SA turbulence model, one can expect the results for the baseline case to be in reasonable agreement with measurements. This indeed turns out to be the case.

Figure 4.4 shows streamlines around the rotor for computed results at 7 m/s, zero yaw with increasing C_μ at the same azimuth. These "snap shot" plots are particles traces using the instantaneous velocity field at selected radial stations near the mid span. The increase in circulation of the rotor is clearly illustrated by the change in the flow field. Due to the Coanda effect, the jet remains attached to the curved trailing edge and provides enhanced suction on the trailing edge upper surface. In this work, the jet leaves the surface from a sharp trailing edge which fixes the rear stagnation point. As C_μ increases the front stagnation point moves backward on the lower surface, and there is a significant turning of the potential flow (outside of the boundary layer) over the airfoil causing an increase in circulation around the rotor section.

Figure 4.5 shows the radial distribution of the pressure force normal to the chord with varying C_μ. A reasonable agreement between prediction and measurements of the baseline case is observed for the no-blowing case at all the yaw angles. As expected, the normal forces for the circulation control case are higher relative to the baseline no-blowing case. It is also seen that C_N increases as C_μ increases. At this low wind speed condition where the flow is well-behaved and attached over much of the rotor, the lift force is increased and also turned forward as a result of the increased angle of attack.

Figure 4.6 shows the radial distribution of the tangential force coefficient C_T with varying C_μ. Note that C_T is tangential to the chord line, and is considered positive when directed towards the leading edge. Again, for the no-blowing case, the computed results are in good agreement with the measurements. It is clearly seen that C_T (associated with the induced thrust component of lift) is increased when circulation control is used.

Figure 4.7 shows the variation of shaft torque (a direct measure of the shaft power extracted) with yaw angle and C_μ. The baseline unblown case and theoretical Betz limit of $\frac{8}{27}\rho A V^3$ (where V is the wind speed) are also shown. It is seen that circulation control considerably increases the torque generated. However, blowing becomes less effective in increasing shaft torque as C_μ increases. Figure 4.8 shows the corresponding root flap moment as a function of yaw angle and C_μ. This indicates that the structure must be augmented to withstand the increased shear forces and bending moments at the root.

Surface pressure coefficient distributions at four radial locations for 0° and 30° yaw cases with C_μ = 0.025 and 0.05 are shown in Figure 4.9 and 4.10 respectively. As stated earlier, the pressure coefficients shown in Figure 4.9 and 4.10 are averaged over one revolution. It can be seen that the increase in circulation resulting from blowing produces an increased loading over the entire blade section, and is not a local effect that occurs only in the vicinity of the slot. In particular, significant suction can be seen at both the leading edge and trailing edge.

The use of the Coanda jet seems to increase the aft loading over the airfoil. This will lead to larger nose down pitching moments. These increased moments may require stiffer and heavier blade sections.

Circulation control technology requires power input into the system to generate the jets. The net power is the mechanical (shaft) power extracted from the wind minus the power input into the system to generate the jets. There should be a net positive increase in power generated for this concept to be attractive. The consumed power to generate the jet is proportional to the mass flow rate through the jet ($\rho_{jet} A_{jet} V_{jet}$) and the kinetic energy per unit mass of the jet ($\frac{1}{2} V_{jet}^2$). Thus, the power consumed in production of the jet is

$(\frac{1}{2}\rho_{jet}A_{jet}V_{jet}^3)/\eta_{sys}$, where η_{sys} is a parameter that takes into account losses or efficiencies associated with various components (such as compressor, duct work, slot design) in the system. For this present work, a range of η_{sys} value was considered (η_{sys} = 1 - no loss; η_{sys} = 0.8 - 25% loss, for example). Figure 4.11 shows the net excess power defined in percentage of baseline power as:

$$Net\ Access\ Power = \left(\frac{P_{circulation} - P_{baseline} - P_{input}}{P_{baseline}} \right) \times 100\% \qquad (4.1)$$

where $P_{circulation}$ = Power generated by the circulation control rotor

$P_{baseline}$ = Power generated from the baseline unblown rotor

P_{input} = Power input into the system

It is clearly seen that approximately up to C_μ = 0.075 there is net excess power production and the excess power production is clearly attributable to the circulation control technology. No net benefit was found at the higher C_μ values.

4.4 Circulation Control Results for High Wind Speed Conditions

A second case studied is for a 15 m/s wind, where the wind speed is high enough to cause flow separation over the entire upper surface. Selected results of zero and 10° yaw conditions are discussed. Results of the trailing edge blowing cases are shown in Figures 4.12-4.15.

At 15 m/s the flow is fully separated over the rotor, and the Coanda jet is not as effective at generating lift as at the 7 m/s case. In this case, it has been found that there is a small change in lift; however, drag is noticeably increased due to the enlarged effective area of wake over the rotor. Figure 4.12 shows streamlines around the rotor for computed

results at 15 m/s, 10° yaw with increasing C_μ at the same azimuth. Those plots in Figure 4.12 are snapshots of the rotor at the advancing blade side. It is seen that the outer flow is not affected by the trailing edge jet as much as it was at the low wind speed (7 m/s) case.

Figure 4.13 shows the normal force coefficient C_N distribution at the same condition. As expected, the normal forces for the circulation control case are higher relative to the baseline no-blowing case. However, the increase in C_N due to the circulation control effects is less at this wind speed compared to the 7 m/s case. Figure 4.14 shows the radial distribution of the tangential force coefficient C_T. Only a small increase in C_T was found at this high wind speed condition for reasons discussed earlier. Thus one can expect the shaft torque (and power output) for this case will not be affected much by the trailing edge blowing. Less than 10% increase in torque was found in this case. Figure 4.15 shows that there is a small increase in power, less than 10% of the baseline power, while blowing the jet requires much larger input power. No net power benefit was found at this high wind speed case.

Thus, one can expect a trailing edge blowing will not be effective if the flow over the airfoil separates at the leading edge. It may be possible to eliminate leading edge stall with a blowing jet placed at the leading edge. The benefit of leading edge blowing for airfoil operating at high angle of attack was investigated by Liu [27]. He found that the use of leading edge blowing, in combination with trailing edge blowing (circulation control) may be effective in suppressing 2-D airfoil stall and extending the benefits of circulation control to high angles of attack. Leading edge blowing has been explored and preliminary results are presented in Section 4.7.

4.5 Effect of Jet Slot Height

As described in Section 2.5, the jet slot boundary condition is specified by the momentum coefficient of the jet, C_μ, which is defined as follows:

$$C_\mu = \frac{\dot{m} V_{jet}}{\frac{1}{2}\rho_\infty V_{ref}^2 A_{ref}} = \frac{\rho_{jet} V_{jet}^2 A_{jet}}{\frac{1}{2}\rho_\infty V_{ref}^2 A_{ref}} \tag{4.2}$$

We can see that, for a given constant C_μ, changing the area of jet slot will affects the jet velocity, and the thickness of the jet stream. The effect of the jet slot height is studied in this section.

To investigate the effect of the jet slot height on the aerodynamic performance of the circulation control wind turbine, computations at wind speed 7 m/s, zero yaw condition have been done with three jet slot heights (0.1%, 0.2%, and 0.4% of chord), at a constant $C_\mu = 0.025$.

Figure 4.16 and 4.17 show the radial distribution of the normal force coefficient C_N and tangential force coefficient C_T, respectively. It is clearly seen that the jet slot height has only a small effect on both normal and tangential force. The shaft torque (and power output) is increased by 5% approximately, as the slot height is decreased from 0.4% to 0.1% of chord. Thus, one can say that changing the jet slot height has insignificant effect on the power generation of the wind turbine, given same value of C_μ.

However, as shown in Figure 4.18, the mass flow rate of the jet is increased about 85% as the jet slot height is increased from 0.1% to 0.4% of chord, due to the larger slot area. While the mass flow rate increases as the jet slot height increases, the input power (power needed to produce the jet) is decreased about 45% (Figure 4.19), due to the lower jet velocity.

As mentioned earlier in Section 4.4, for the circulation control wind turbine, the operating range which yields the net benefit in power production is always preferable. For this case, with nearly same amount of power generated, the larger jet slot height is more attractive than the smaller jet slot height because it consumes less power (approximately 45% less) to produce the jet flow. Moreover, according to the acoustic study of jet noise [110], a larger jet slot produces less noise than a smaller jet slot. Though a larger jet is preferred from the wind turbine performance and acoustic perspectives, having too large of jet slot near the trailing edge may cause difficulty in manufacturing. Thus, a compromise should be made for the jet slot height.

4.6 Effect of Pulsed Blowing Jet

Calculations have been obtained for the NREL Phase VI rotor at wind speed of 7 m/s wind speeds, zero yaw, and the steady jet momentum coefficient $C_\mu = 0.025$ is used. The jet slot configuration and location are same as in the steady jet studies presented in previous section. In the present work, the jet momentum coefficient C_μ is assumed to vary with time as follows:

$$C_\mu(t) = C_{\mu,0}[1 + F(t)] \tag{4.3}$$

where $C_{\mu,0}$ is the time-average jet momentum coefficient, which is also the value of the steady jet for comparison. F(t) is a function of time, which varies from -1 to 1, and determines the temporal variation of the pulsed jet.

In this work, the effect of a square wave pulse jet is studied. Liu [27] reported the advantage of the square wave pulsed jet in producing the comparable lift of the CC airfoil at lower mass flow rate. Thus the squared wave pulsed jet is seen to be beneficial in power production of the wind turbine application. For the square wave pulsed jet, the

function F(t) in equation (4.3) is chosen to be a square wave form with 50% duty cycle. With this setting, F(t) is set to value +1 for half cycle, and -1 for the other half cycle. The instantaneous C_μ is equal to zero during one half and equal to $2C_{\mu,0}$ during the other half of the cycle as shown in Figure 4.20. Thus, the time-averaged value is $C_{\mu,0}$, which is also the value of the steady jet used for comparison. Note that the frequency indicates the number of cycles that the jet is turned on and off per second.

Figure 4.21 and Figure 4.22 show the radial distributions of normal force and tangential force, respectively, at two frequencies; 50 Hz and 100 Hz. Results are compared to the baseline steady blowing jet at same C_μ. It is found that there is no appreciable improvement in C_N and C_T for both frequencies, compared to the steady jet. Slight decrease in C_T is observed for a 50Hz pulsed jet. This is because, at lower frequency, the beneficial effects of Coanda jet are lost over larger portion of the time compared to the higher frequency pulsed jet, and the rotor behaves like an unblown baseline rotor. In general, the higher frequencies are preferred over lower frequencies.

Figure 4.23 shows the variation of mass flow rate as a function of time. It is clearly seen that the average mass flow rate of the square wave pulsed jet is lower than that of the steady jet. This can be explained as follows. The momentum coefficient is proportional to the square of the jet velocity V_{jet}^2 , while the mass flow rate is proportional to the jet velocity V_{jet} . As a result, changing the instantaneous momentum coefficient to twice its average value increases the instantaneous mass flow rate only by a factor of $\sqrt{2}$, compared to a steady jet. Thus, the average mass flow rate of the square wave pulsed jet is approximately 70% of the average mass flow rate of a steady jet at the same average

C_μ. Note that, since the average momentum coefficient is independent of the frequency, the mass flow rate and the jet velocity do not depend on the frequency as well.

It is seen that the square wave pulsed jet is preferred over the steady jet due to its lower mass flow rate. However, the results show that the square wave pulsed jet consumes about 50% more power needed to produce the jet flow than the steady jet. This drawback makes the square wave pulsed jet less attractive than the steady jet for the circulation control wind turbine.

4.7 Effect of Leading Edge Blowing

As mentioned earlier, leading edge blowing is an effective way to alleviate stall and to achieve desired performance at higher angle of attack. It has the potential to help suppress the leading stall of wind turbines under high wind speed conditions, and enhance the power generation.

To investigate the performance of the effect of leading edge blowing, a jet was placed at 1.25% of chord measured from the leading edge. This jet is located on the lower surface and blows the jet stream toward the leading edge using the curved leading edge to produce the Coanda effect. The jet slot height is 0.2% of chord, same as for trailing edge blowing. Only the steady blowing has been investigated in this study.

Figure 4.24 shows the flow field around the rotor with leading edge blowing. Figure 4.25 and 4.26 show the radial distribution of normal force coefficient C_N and tangential force coefficients C_T, respectively. It can be seen that leading edge blowing has negligible effect on C_N because the jet is ineffective in suppress the leading edge separation. Flow is still separated over the upper surface. However, the jet itself creates a suction area around the leading edge due to its high velocity (Figure 4.27). The suction

become stronger as C_μ increase and creates a propulsive force pulling the blade forward resulting in an increased tangential force. Thus, one can expect that the shaft torque and power output are also increased (Figure 4.28).

4.8 Structural Issues

Most wind turbine blades are constructed with hollow shell structures corresponding to the designed blade shape which provides a simple, efficient structure to resist flexural and torsional loads. Negative moulds for the upper part (suction side) and the lower part (pressure side) of the blade are made. Typically a thin shell is made around the leading edge and the trailing edge, and the think shell is made in the middle of the blade airfoil. For most modern wind turbines, the glass-fibre reinforced plastic (GFRP) is the material now commonly used in the blade construction.

Though the GFRPs have a substantially higher compressive strength-to-weight ratio compared to other materials (aluminum, steel), the relative low Young's modulus of these composites yields the panel stability problem. The resistance to buckling of the thin shell dominates the structure design, rather than simple compression yielding. Thus, cutting a jet slot through thin skins near the trailing edge and installing a plenum for a blowing jet may not be feasible. As a result, the circulation enhancement concept by a leading or trailing edge blowing needs to be further explored from a structural stability and strength point of view.

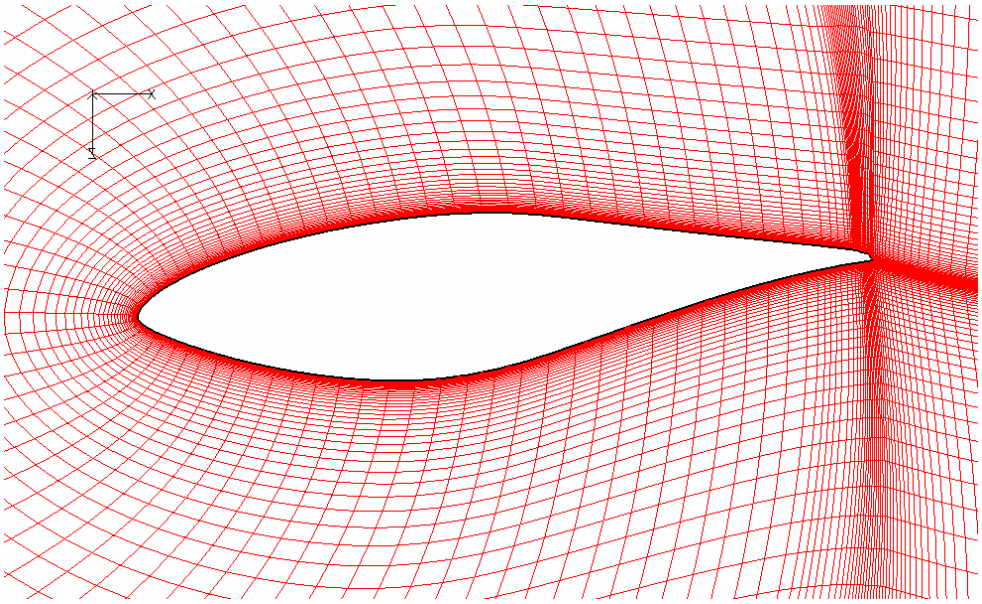

(a) C grid near the rotor surface

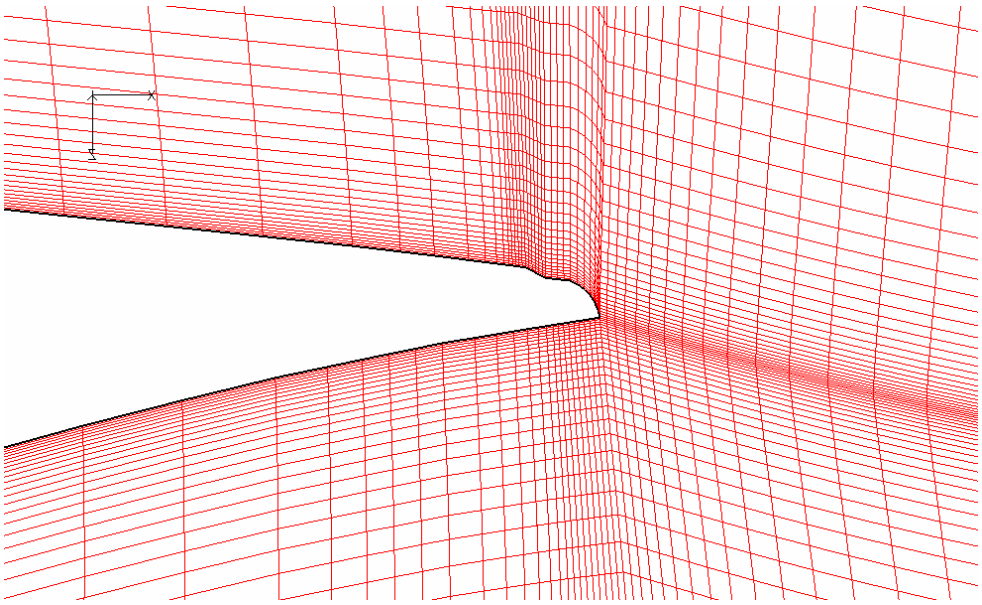

(b) Mesh in vicinity of jet slot

Figure 4.1 Body-fitted C grid used for the circulation control rotor

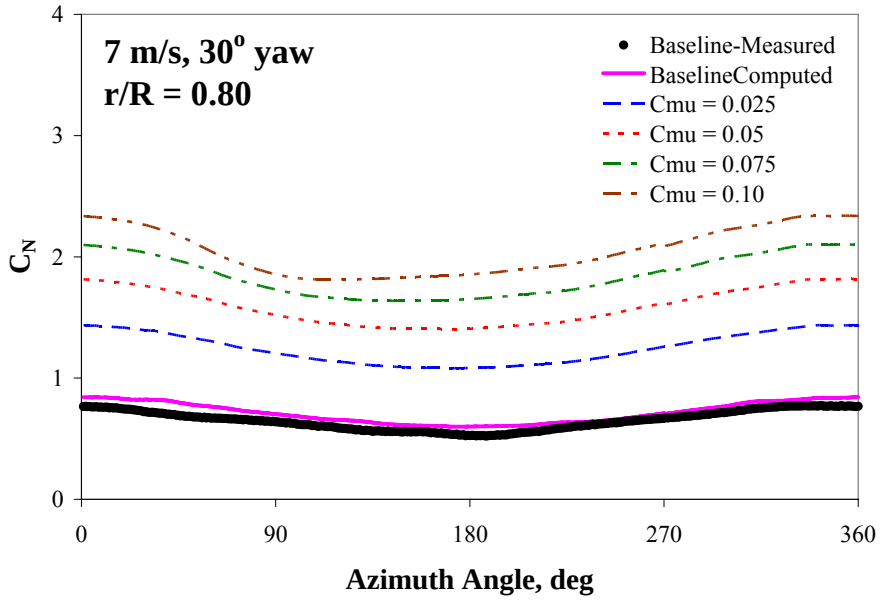

Figure 4.2 Azimuth variation of the normal force coefficient C_N at 7 m/s, 30° yaw; with and without blowing

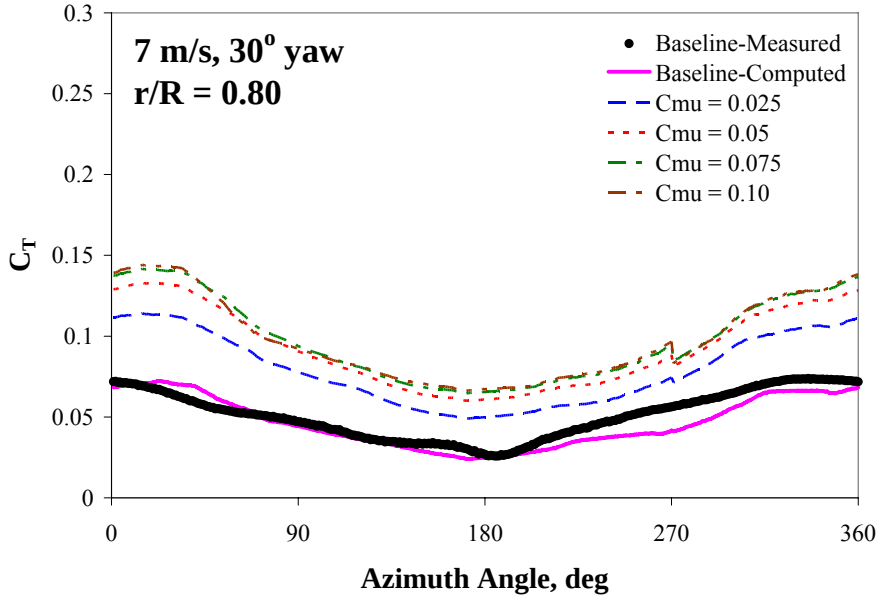

Figure 4.3 Azimuth variation of the tangential force coefficient C_T at 7 m/s, 30° yaw; with and without blowing

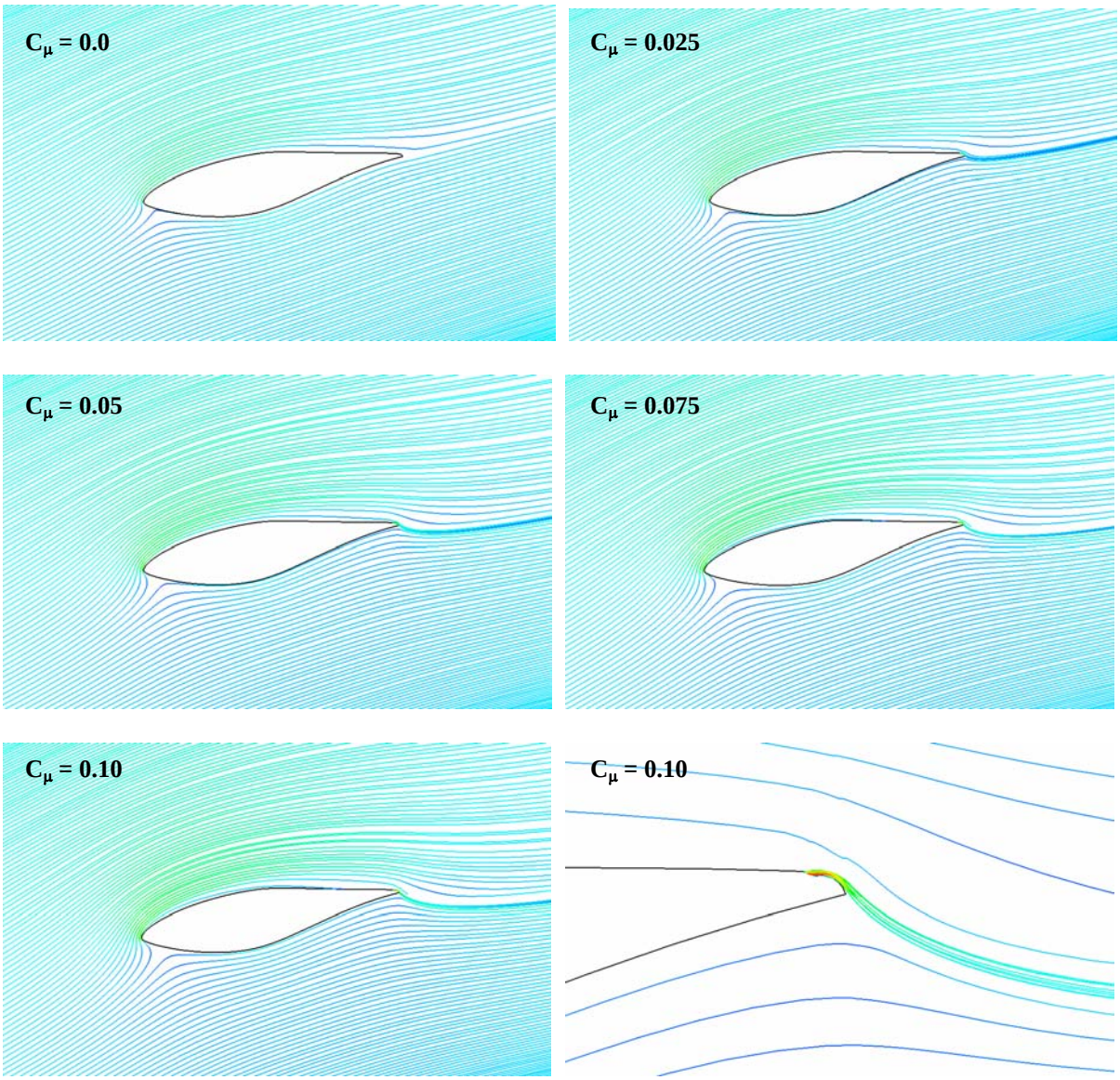

Figure 4.4 Computed streamlines over the rotor at 7 m/s, 0° yaw

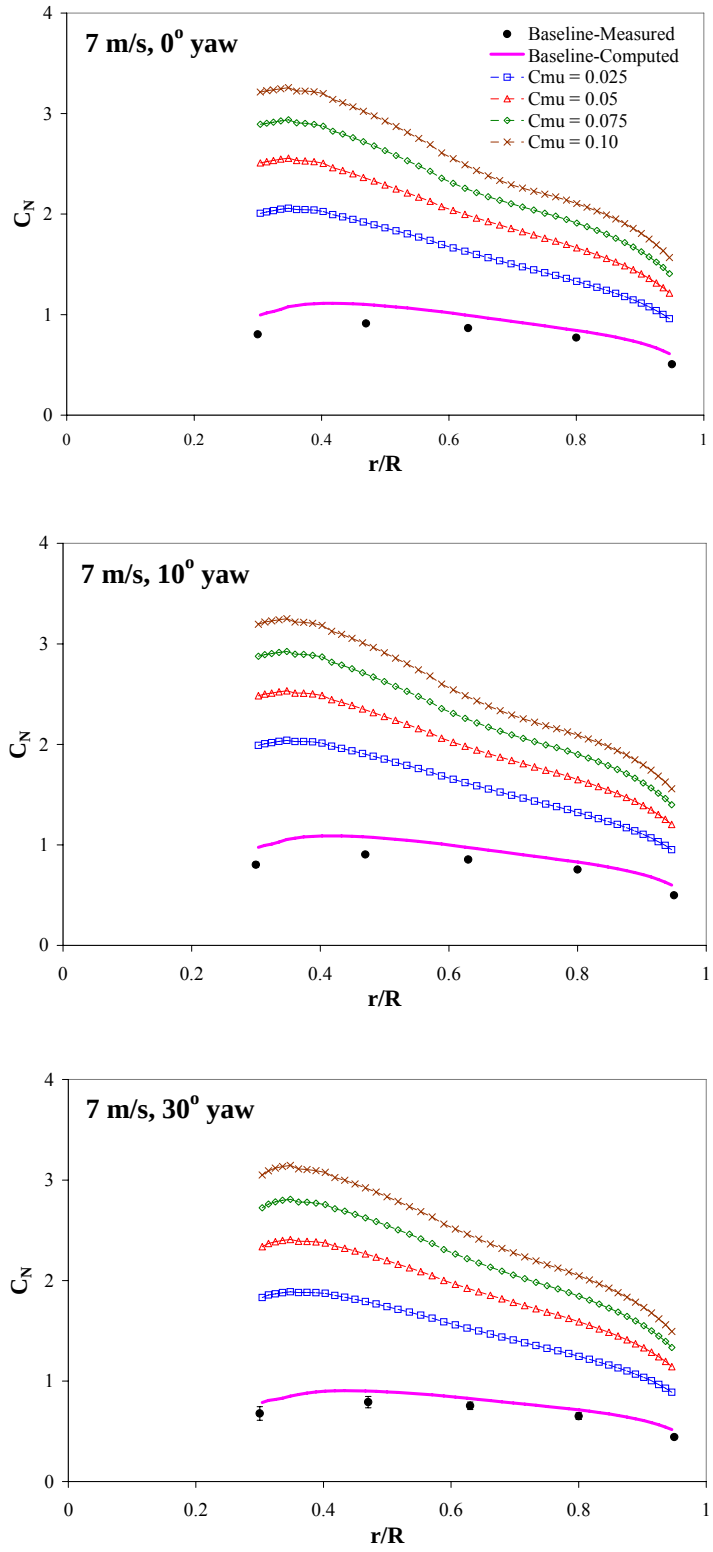

Figure 4.5 Radial distribution of the normal force coefficient C_N at 7 m/s with varying C_μ

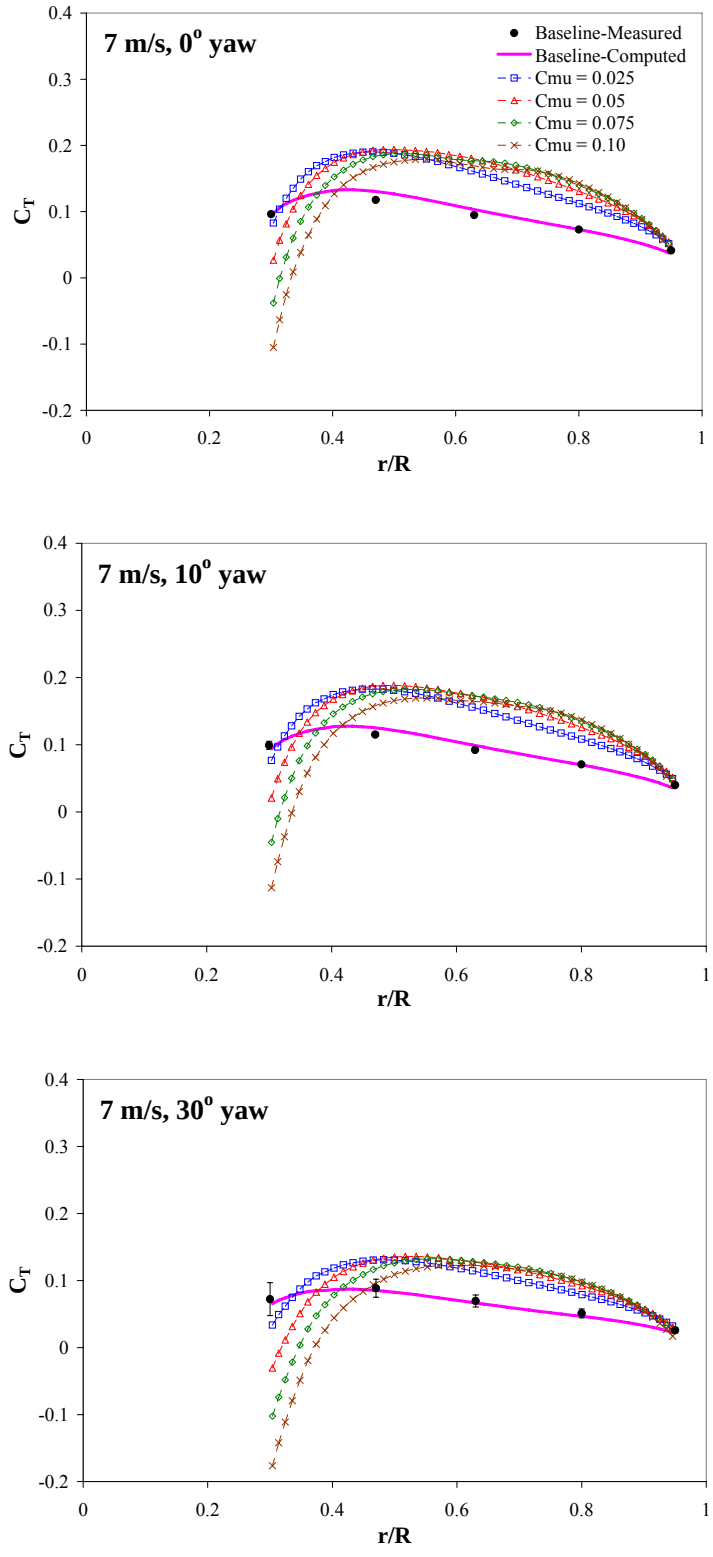

Figure 4.6 Radial distribution of the tangential force coefficient C_T at 7 m/s with varying C_μ

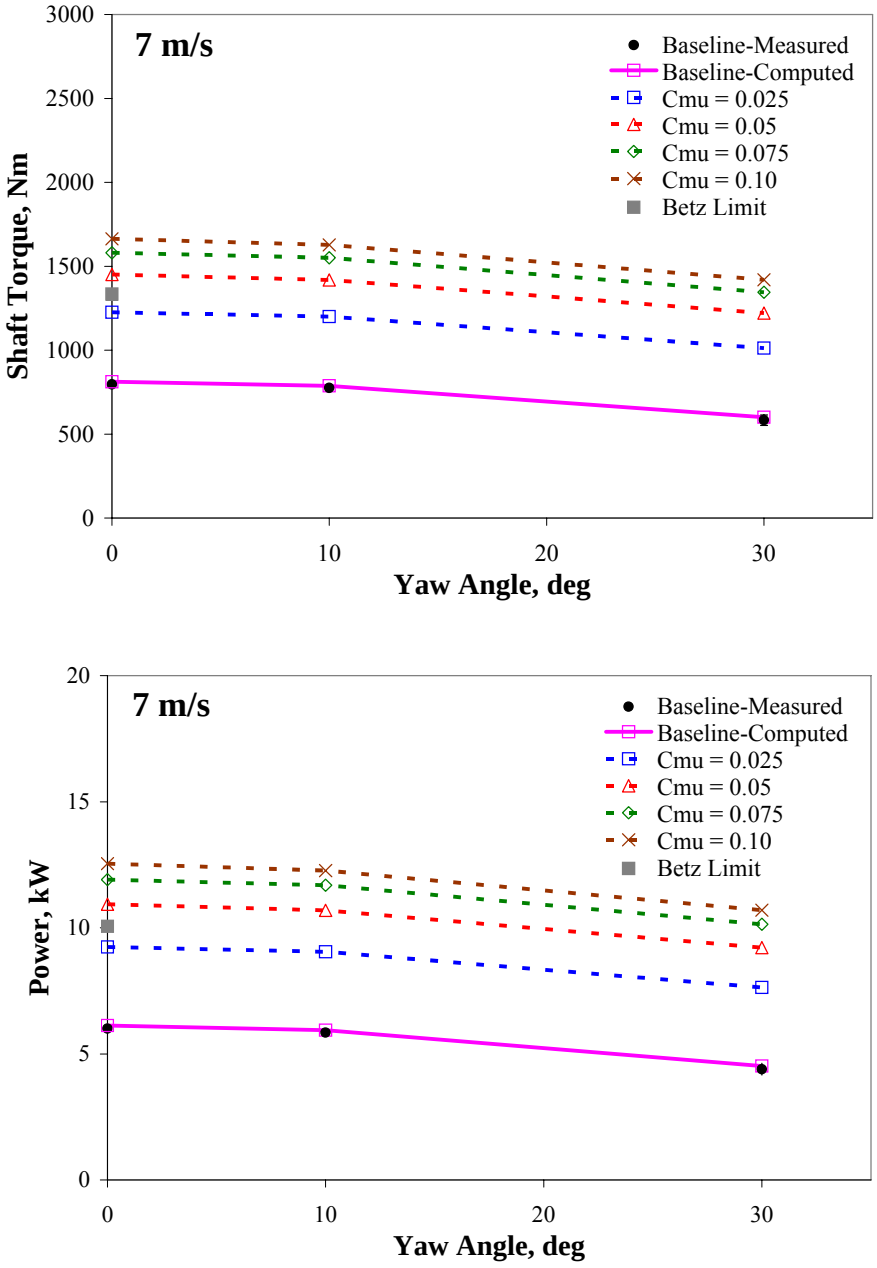

Figure 4.7 Variation of the shaft torque and the corresponding power at 7 m/s as a function of yaw angle with varying C_μ

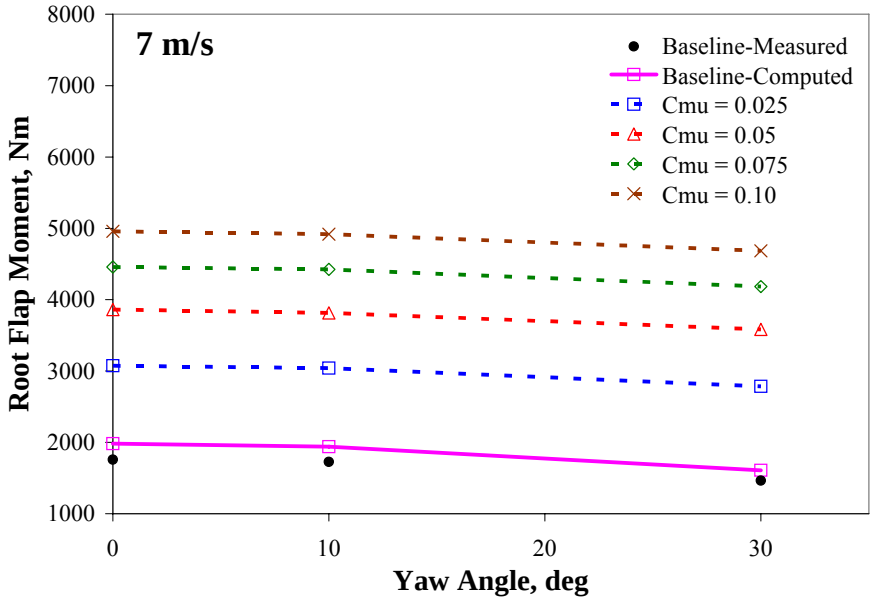

Figure 4.8 Variation of the root flap moment at 7 m/s as a function of yaw angle with varying C_μ

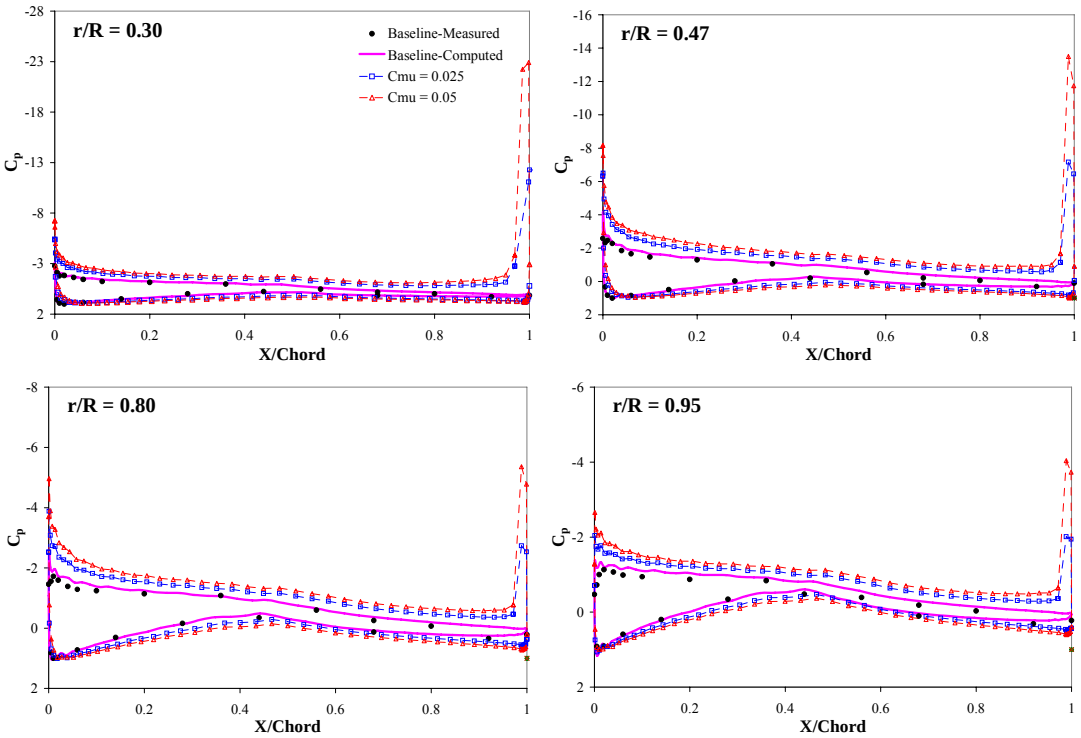

Figure 4.9 Comparison of pressure coefficient distribution at 7 m/s, 0° yaw; with and without blowing

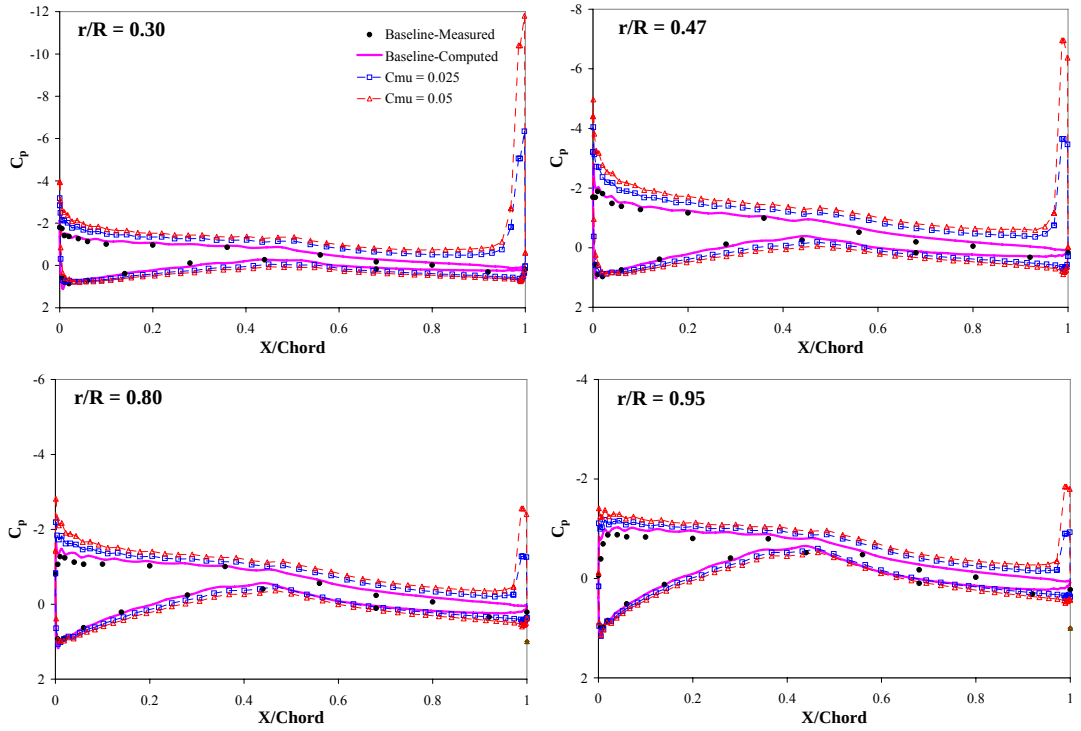

Figure 4.10 Comparison of pressure coefficient distribution at 7 m/s, 30° yaw; with and without blowing

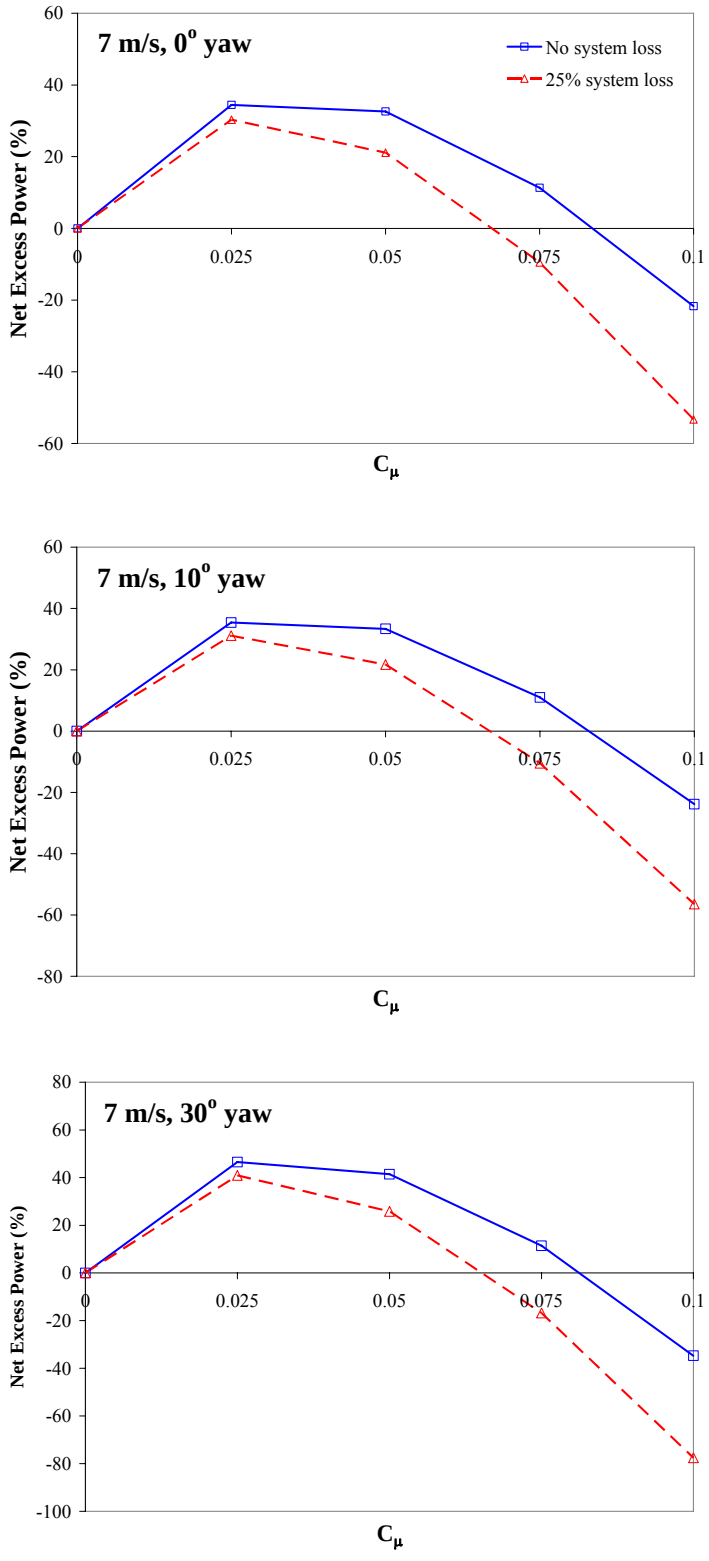

Figure 4.11 Net Excess Power vs. C_μ at 7 m/s with 0°, 10°, and 30° yaw

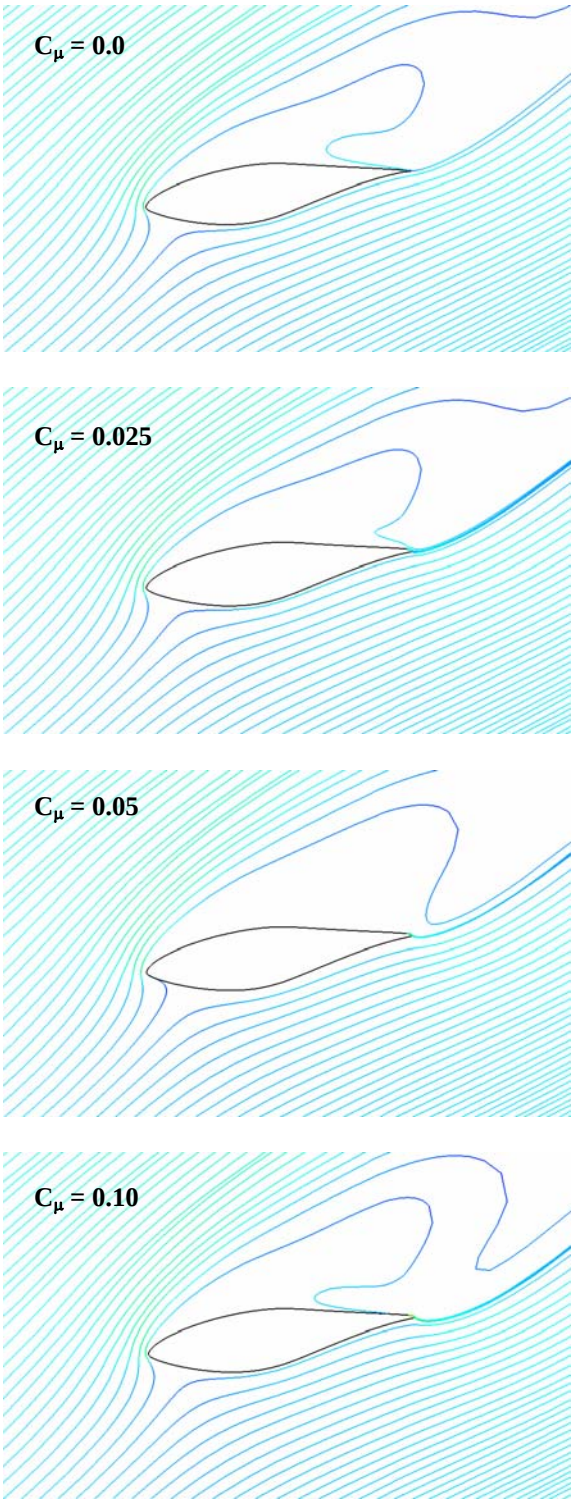

Figure 4.12 Computed streamlines over the rotor at 15 m/s, 10° yaw

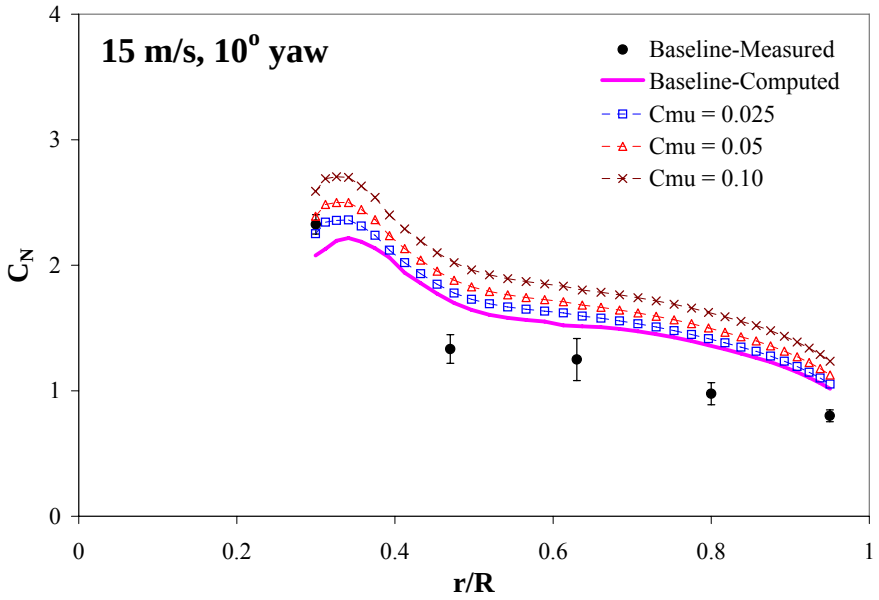

Figure 4.13 Radial distribution of the normal force coefficient C_N at 15 m/s and 10° yaw with varying C_μ

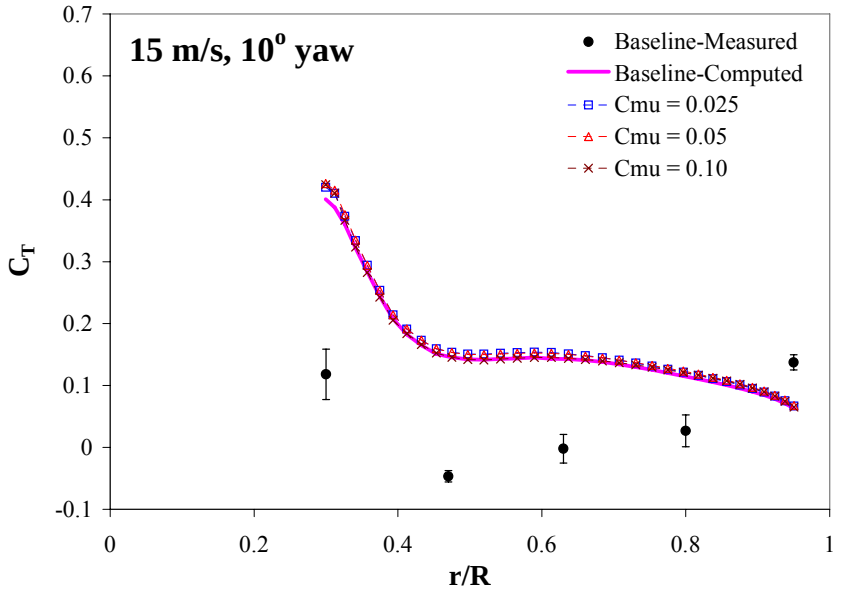

Figure 4.14 Radial distribution of the tangential force coefficient C_T at 15 m/s and 10° yaw with varying C_μ

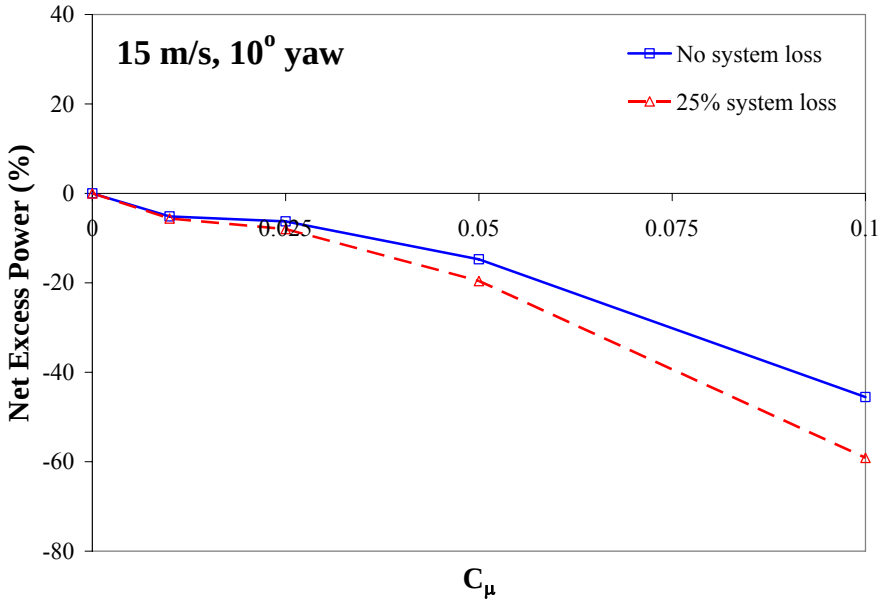

Figure 4.15 Net Excess Power vs. C_μ at 15 m/s and 10° yaw

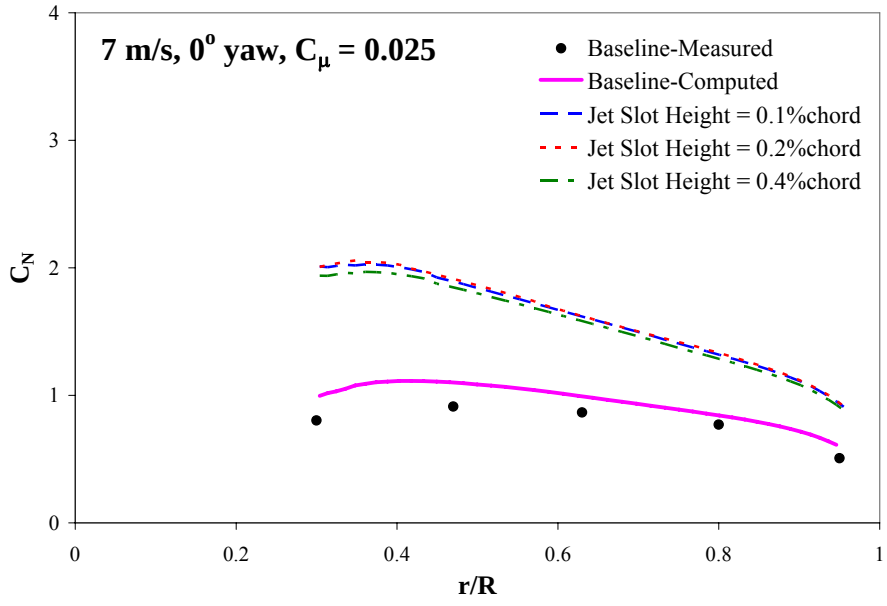

Figure 4.16 Radial distribution of the normal force coefficient C_N with varying jet slot height (7 m/s, 0° yaw, and C_μ = 0.025)

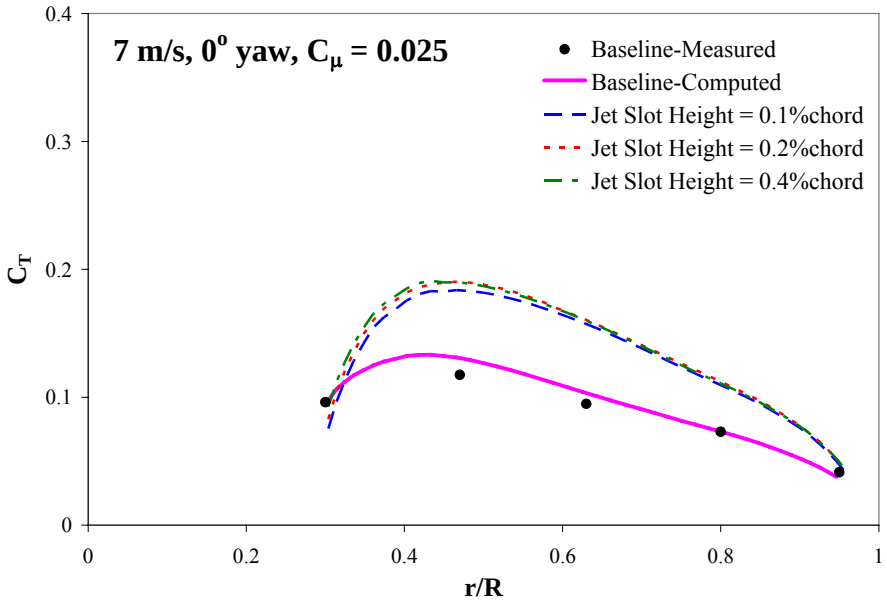

Figure 4.17 Radial distribution of the tangential force coefficient C_T with varying jet slot height (7 m/s, 0° yaw, and C_μ = 0.025)

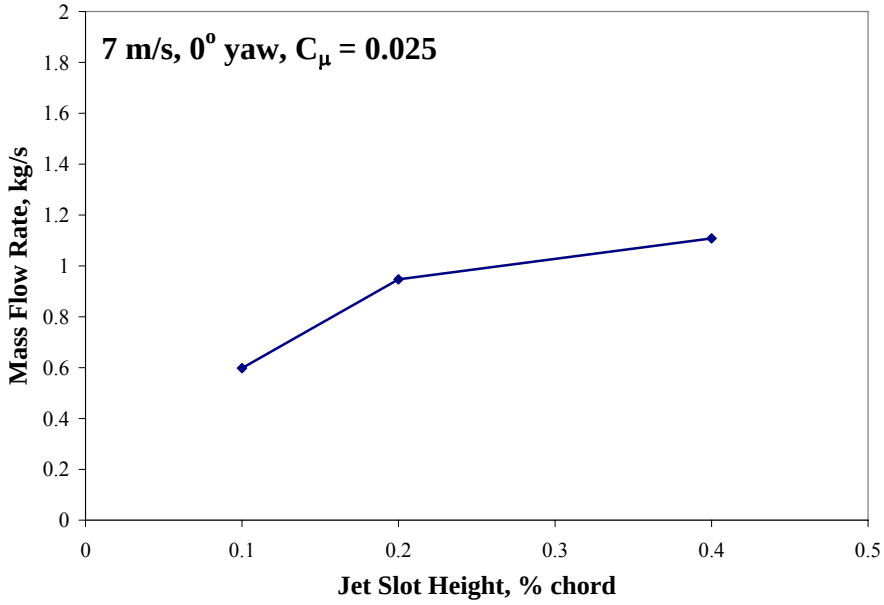

Figure 4.18 Variation of mass flow rate as a function of jet slot height (7 m/s, 0° yaw, andC_μ = 0.025)

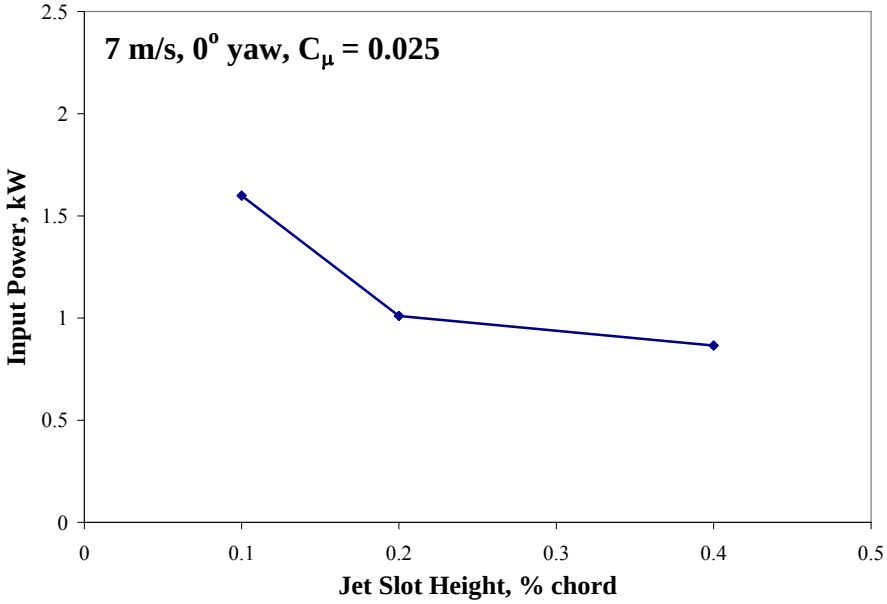

Figure 4.19 Variation of input power as a function of jet slot height (7 m/s, 0° yaw, andC_μ = 0.025)

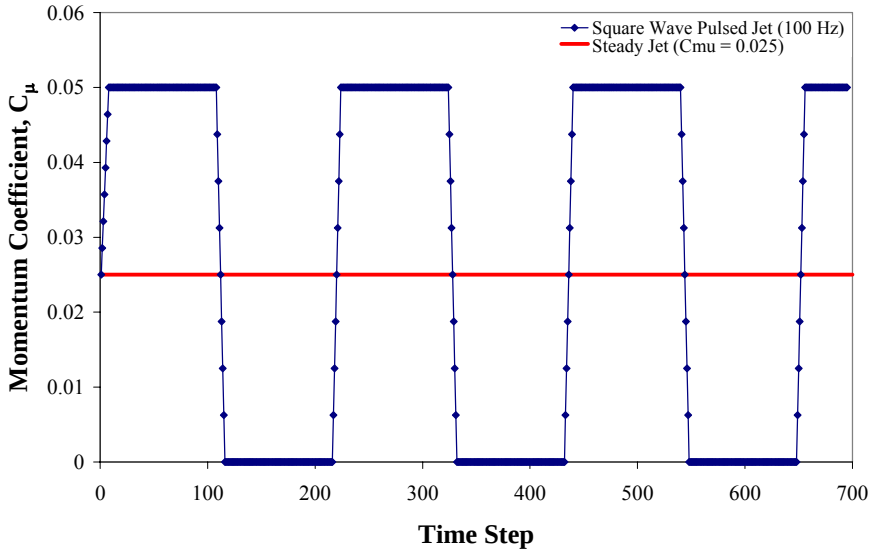

Figure 4.20 Time history of the momentum coefficient C_μ

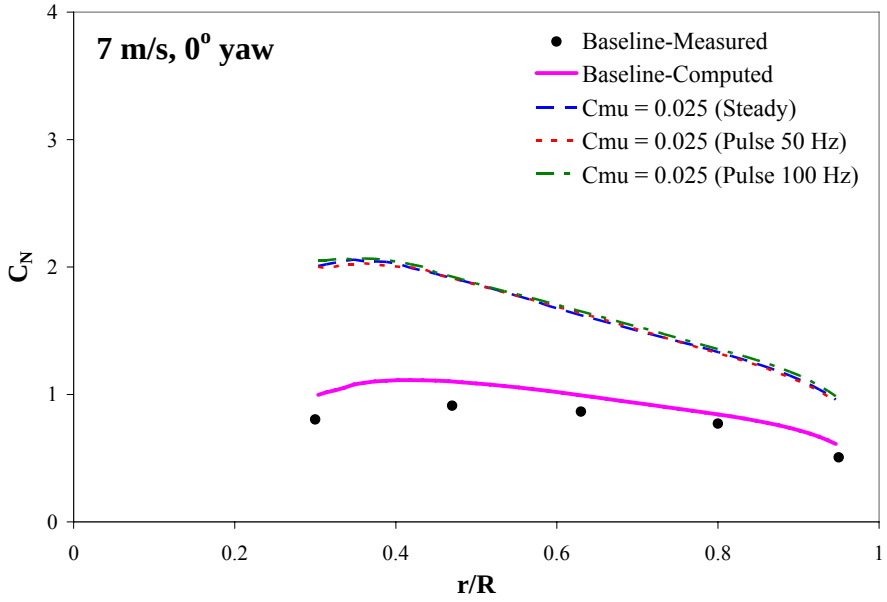

Figure 4.21 Radial distribution of the normal force coefficient C_N with varying blowing frequency

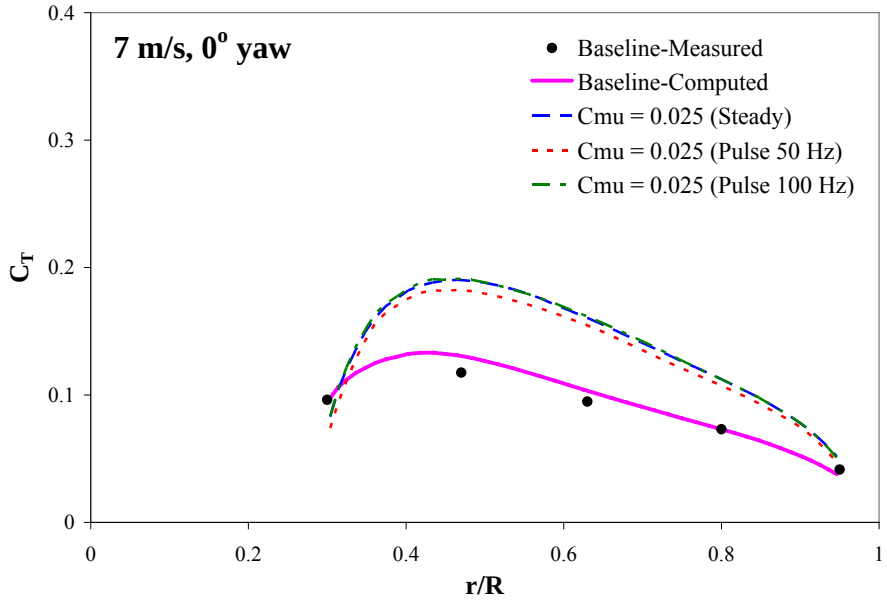

Figure 4.22 Radial distribution of the tangential force coefficient C_T with varying blowing frequency

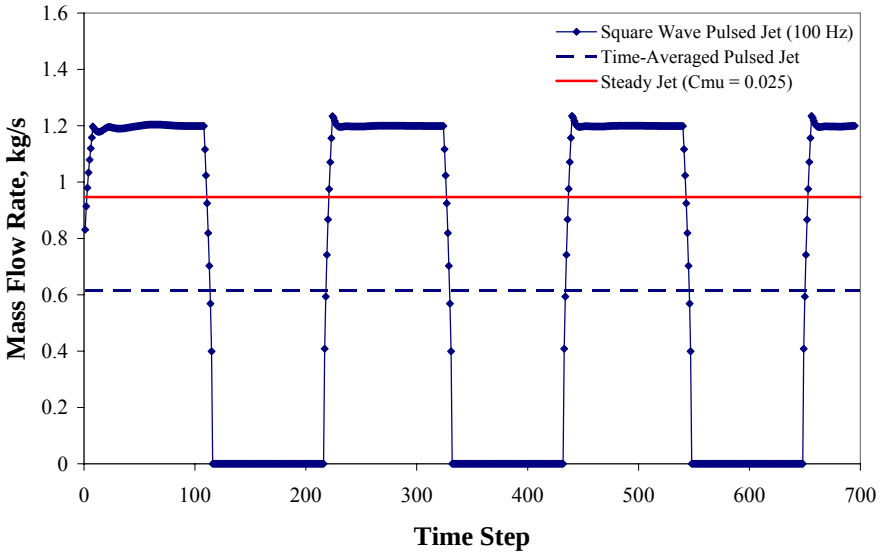

Figure 4.23 Time history of the mass flow rate

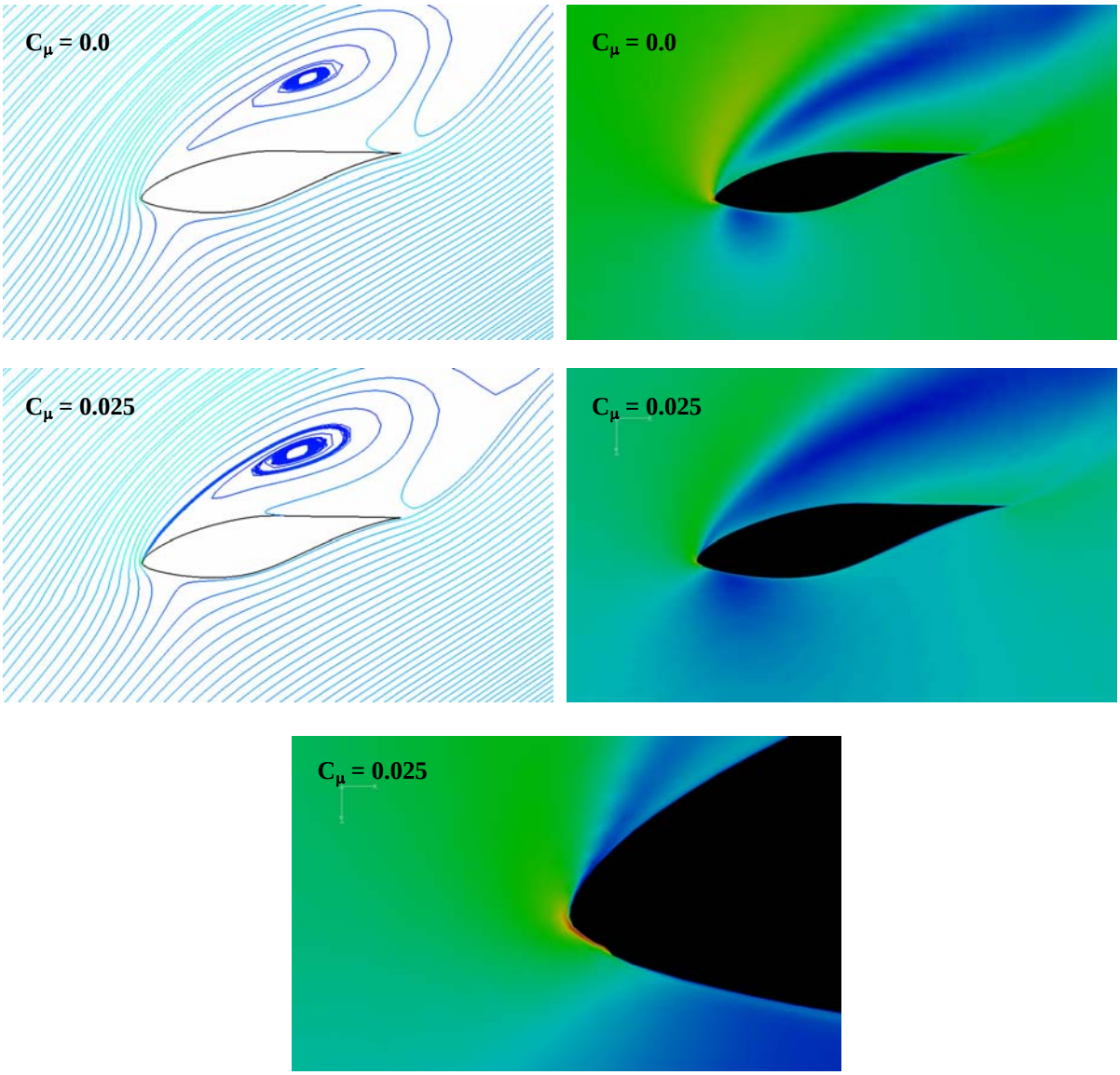

Figure 4.24 Computed flow field over the rotor at 15 m/s, 0° yaw

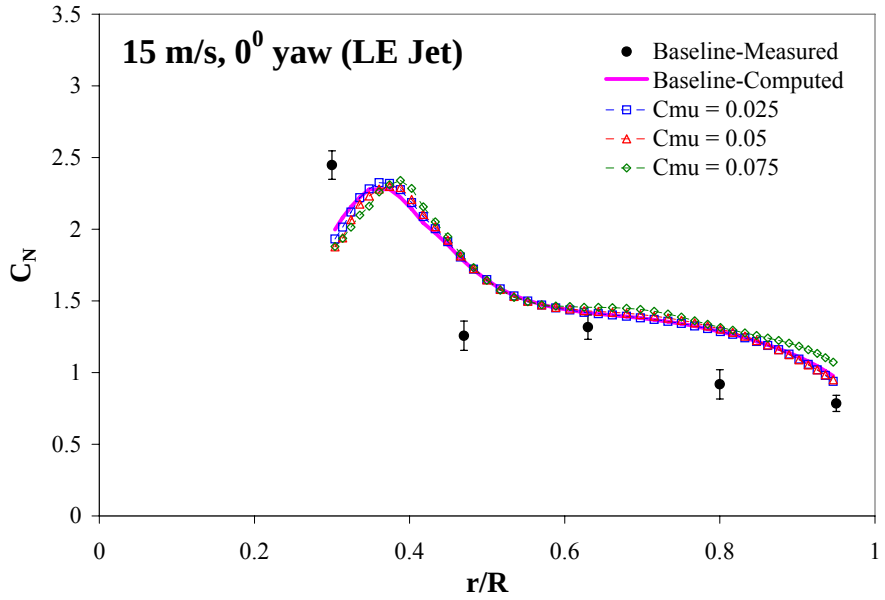

Figure 4.25 Radial distribution of the normal force coefficient C_N with varying C_μ

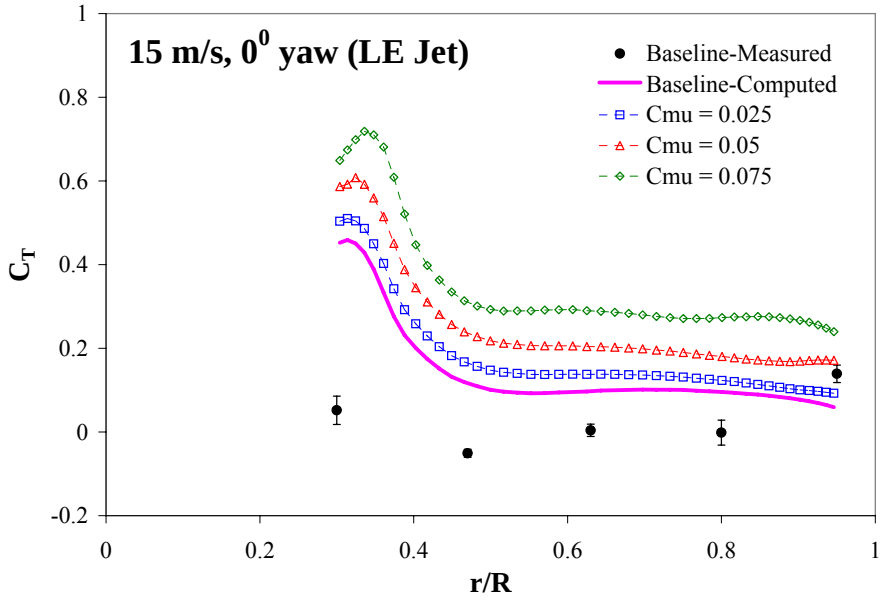

Figure 4.26 Radial distribution of the tangential force coefficient C_T with varying C_μ

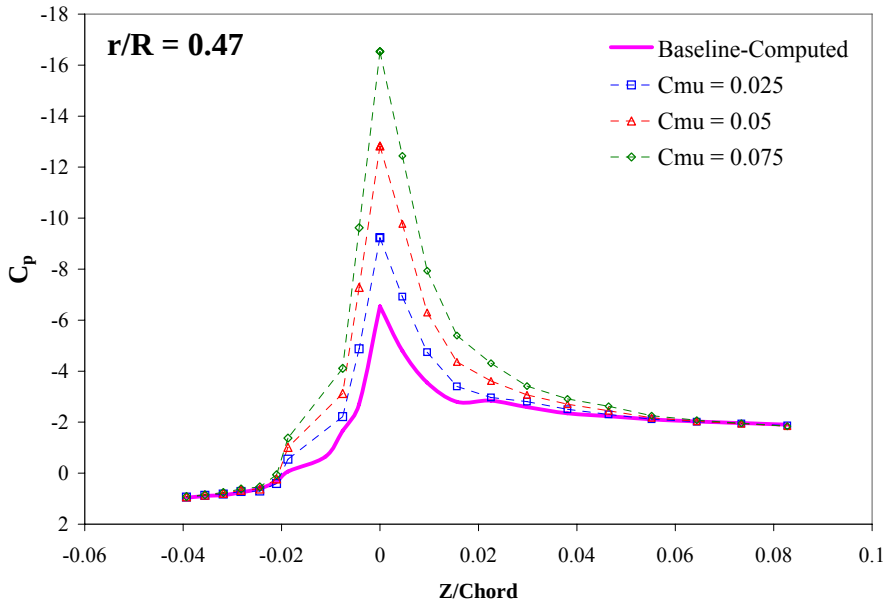

Figure 4.27 Pressure coefficient distribution around the rotor leading edge at 15 m/s, 0° yaw; with and without blowing

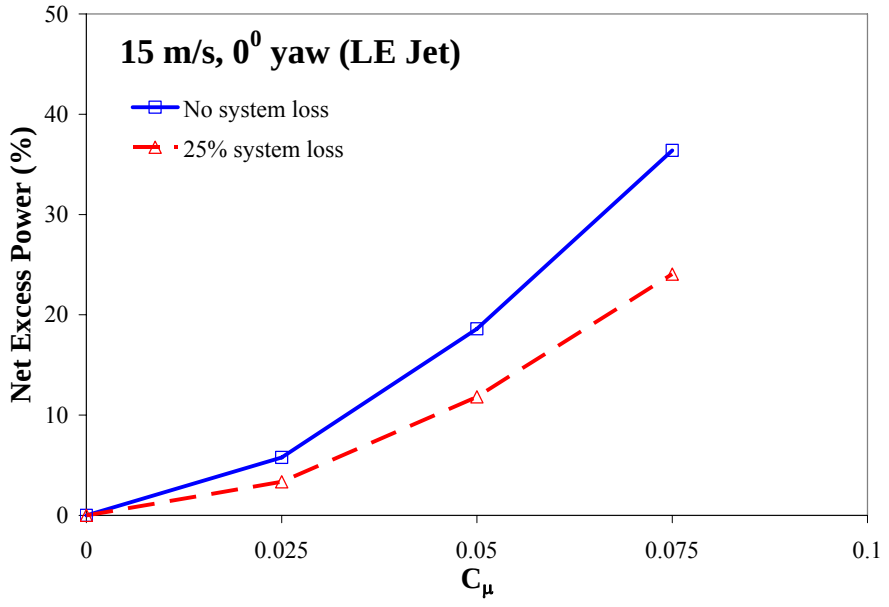

Figure 4.28 Net Excess Power vs. C_μ at 15 m/s and 0° yaw; Leading edge blowing

CHAPTER 5

RESULTS OF PASSIVE CIRCULATION ENHANCEMENT CONCEPT: GURNEY FLAP

In the previous chapter we looked at active techniques for enhancing the circulation around airfoils and their L/D characteristics, and hence power production. In this chapter, we will discuss a passive concept, namely the Gurney flap, for circulation enhancement. The impact of Gurney flaps on the airfoil lift-to-drag ratio is discussed in Ref. [43],[111]-[113]. Computations have been obtained at selected wind speeds representing both low and high wind speed regimes. The results are compared to the baseline unblown case presented in Chapter 3. Results of low wind speed condition are first presented. Next, results of high wind speed condition are discussed. Finally, the effects of Gurney flap angle on the performance are presented.

5.1 Grid System Used in the Study

The computational grid used in this study is similar to the grid used for baseline rotor analysis in Chapter 3, with minor modifications to model the gurney flap attached to the trailing edge. In this study, the length of Gurney flap is 1.5% of chord. A larger Gurney flap may improve lift production but will have a high drag penalty. In the present work, the Gurney flap runs along the entire length of the flap. The grid near the rotor surface and the flap is shown in Figure 5.1.

5.2 Results for Low Wind Speed Conditions

Figure 5.2 shows streamlines over the rotor for computed results at 7 m/s, zero yaw; with and without the Gurney flap. On the windward side of the flap, the local

pressures are considerably higher than the leeward side. The lower pressures on the leeward side have a tendency to create a favourable pressure gradient over the upper surface of trailing edge, causing the flow to follow the flap and turn downward, as illustrated in this figure. The entire circulation over the rotor is enhanced, similar in effect to that achieved by the Coanda jet (see Figure. 4.4).

Figure 5.3 shows the radial variation of normal force coefficient C_N with and without the Gurney flap at three yaw conditions (0°, 10°, and 30°). The beneficial effects of the flap in increasing the lift are clearly seen. Figure 5.4 shows the radial variation of tangential force coefficient C_T. The increase in the tangential force due to the deployment of the flap leads to an increase in torque (and hence the power) generated as shown in Figure 5.5, while the increase in the normal force has the undesirable side effect of an increase in root flap moments, as seen in Figure 5.6. Figure 5.5 also shows the theoretical Betz limit of $\frac{8}{27}\rho A V^3$ (where V is the wind speed).

Surface pressure coefficient distributions at four radial locations at 7 m/s and zero yaw are shown in Figure 5.7. It can be seen that the increase in circulation resulting from Gurney flap produces an increased loading over the entire blade section. Once again, this is similar in effect to that obtained by the Coanda jet.

Figure 5.8 shows comparisons of the effectiveness of the Gurney flap and the Coanda jet at trailing edge in enhancing blade forces, shaft torque, root flap moment, and net excess power. It is clearly seen that circulation control using the trailing edge blowing resulted in a greater shaft torque (hence power output) compared to Gurney flap. However, because blowing requires power, the net excess power obtained from

circulation control is nearly the same as that from Gurney flap. Furthermore Gurney flap concept is more easily implemented and does not require any input power.

5.3 Results for High Wind Speed Conditions

Calculations have also been done for 15 m/s wind conditions, where the wind speed is high enough to cause flow separation over the entire upper surface. As discussed in previous chapter, the circulation control technique may not be effective for high wind conditions where the flow is massively separated. One can expect similar results to that obtained by the blowing jet at high wind speed condition. Figure 5.9 shows streamlines over the rotor at 15 m/s at zero yaw. There is an extensive separation over the rotor. It is seen that the Gurney flap has a negligible influence on the flow field, under this separated flow condition. The use of the Gurney flap thus results in only a small increment of the normal and tangential force components (Figure 5.10, Figure 5.11) and on the production of shaft torque or power output (Figure 5.12). For better readability of the data plotted in Figure 5.12, the theoretical Betz limit, which is approximately 13,100 Nm, is not shown as it was in previous figures.

5.4 Effects of Gurney Flap Angle on Power Production

As mentioned in the first chapter, the effect of the Gurney flap in increasing lift is dependent on the lower pressures on the leeward side of the Gurney flap. The lower pressures have tendency to create a favorable pressure gradient over the upper surface of the trailing edge and cause the flow to follow the flap and turn downward. The entire circulation over the rotor is enhanced, similar in effect to that achieved by the Coanda jet. Therefore, changing the flap angle may affect the pressure gradient over the upper surface and hence the wind turbine performance. In the following calculations, the effect

of the flap angle on the wind turbine performance is investigated at three different flap angles; 45°, 60°, and 90°, at low wind speed 7 m/s with zero yaw.

Figure 5.13 shows the radial distribution of the pressure force normal to the chord with varying flap angle. It is seen that the normal forces of the rotor with higher flap angle are relatively higher than those with smaller flap angle. Figure 5.14 shows the radial distribution of the tangential force coefficient C_T with varying flap angle. It is clearly seen that C_T (associated with the induced thrust component of lift) is increased when a higher flap angle is used.

At the 7 m/sec, for these three Gurney flap angles (45°, 60°, and 90°), the shaft torque was approximately 940 Nm, 1080 Nm, and 1140 Nm, respectively. The baseline configuration (no Gurney flap, 7 m/sec, and zero yaw) produced 800 Nm Thus, it is clear that the Gurney flap produces progressively more torque, which translates into useable power as long as the flow over the trailing edge is attached.

5.5 Structural Issues

Gurney flap can simply be a length of aluminum right-angle rigidly bolted or riveted to the lower surface at vicinity of the trailing edge of wind turbine blade. Given the fact that the trailing edge of a wind turbine blade is typically sharp, which provides small volume and a lack of support structure, it is obviously that Gurney flap is more practically implemented on the wind turbine blade compared to blowing jet.

However, as mentioned in Section 4.8, the blade surfaces near the trailing edge are built relative thin using composite materials, thus the panel structures have to have enough strength to support the weight of the Gurney flap and to withstand the stress concentration due to bolting the flap to the blade surface.

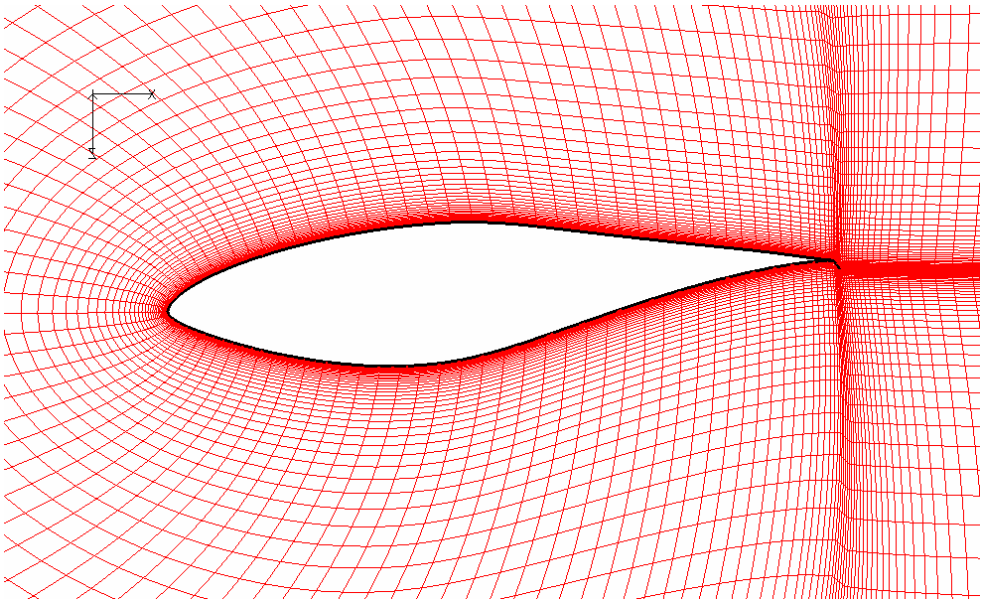

(a) C grid near the rotor surface

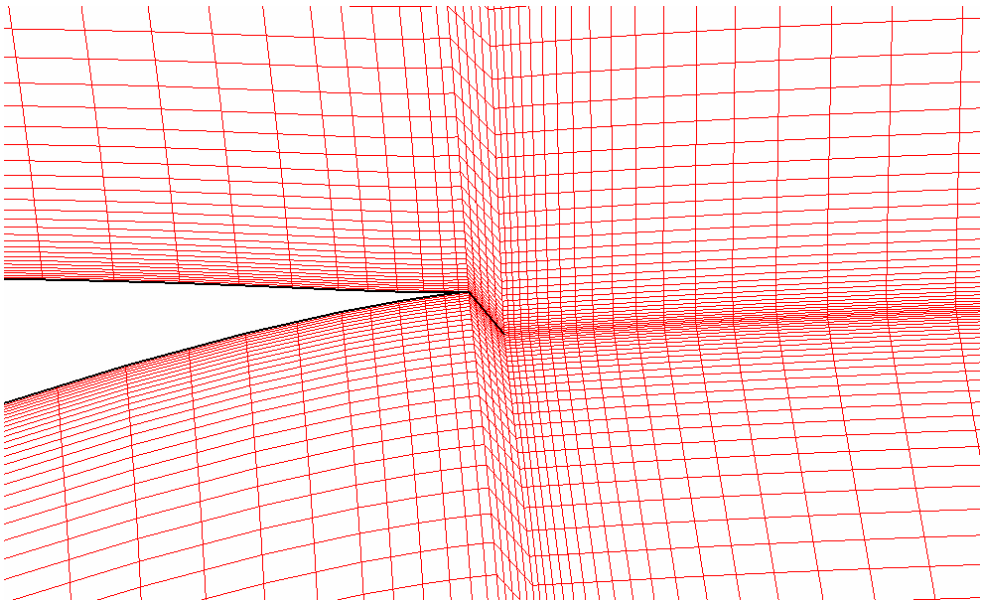

(b) Mesh in vicinity of Gurney flap

Figure 5.1 Body-fitted C grid of the rotor with Gurney flap

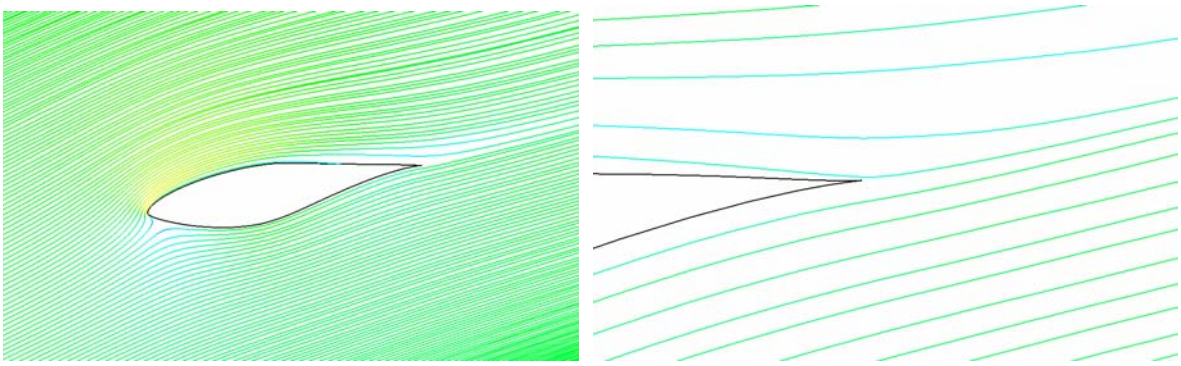

(a) Without the Gurney flap

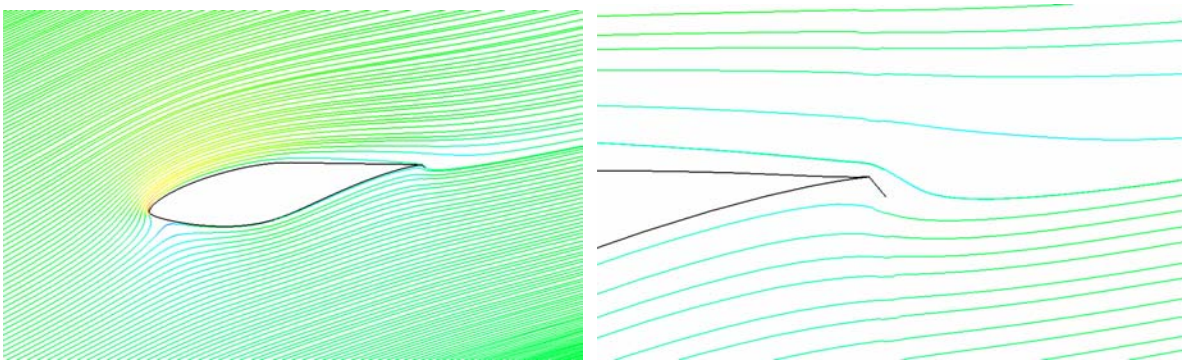

(b) With the Gurney flap

Figure 5.2 Computed streamlines over the rotor at 7 m/s, 0° yaw; Gurney flap case

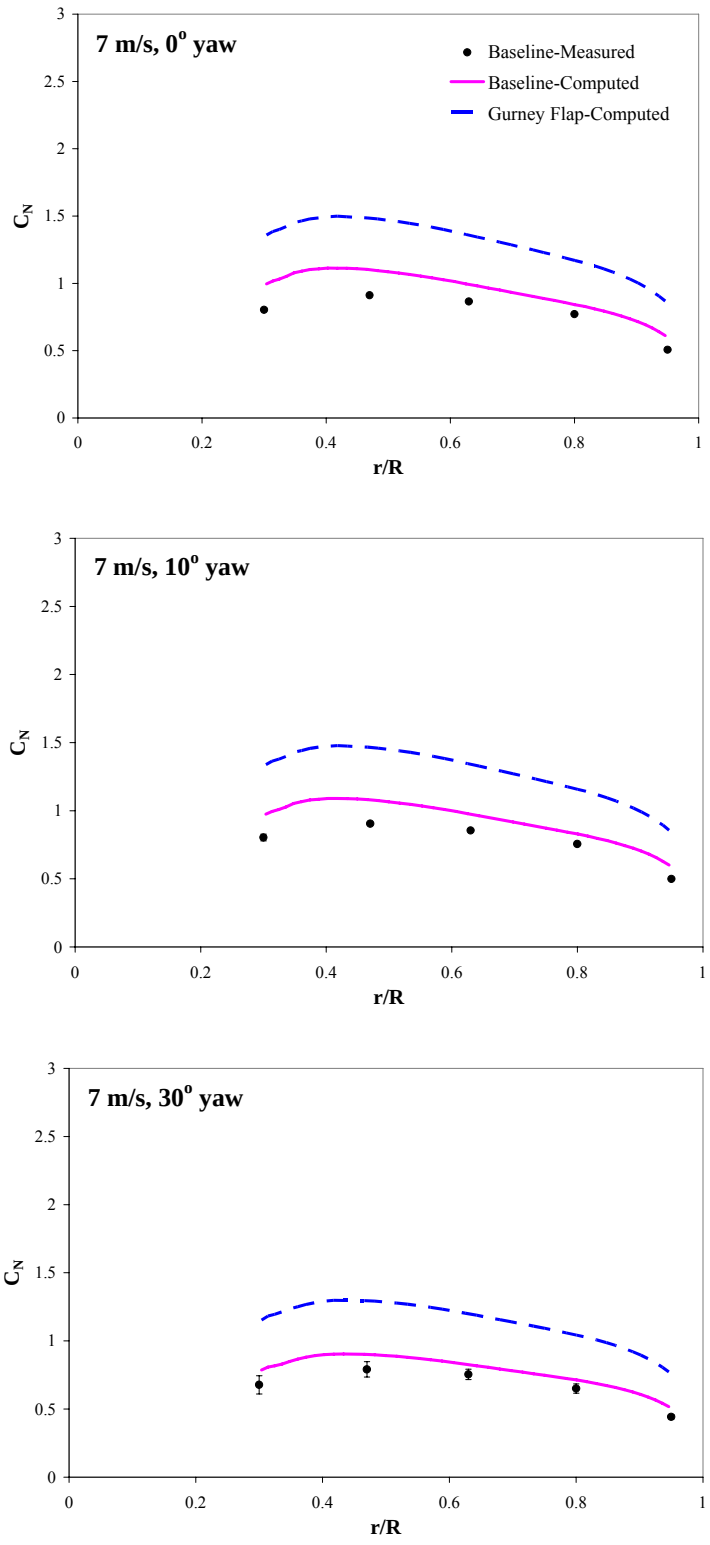

Figure 5.3 Radial distribution of the normal force coefficient C_N at 7 m/s; with and without a Gurney flap

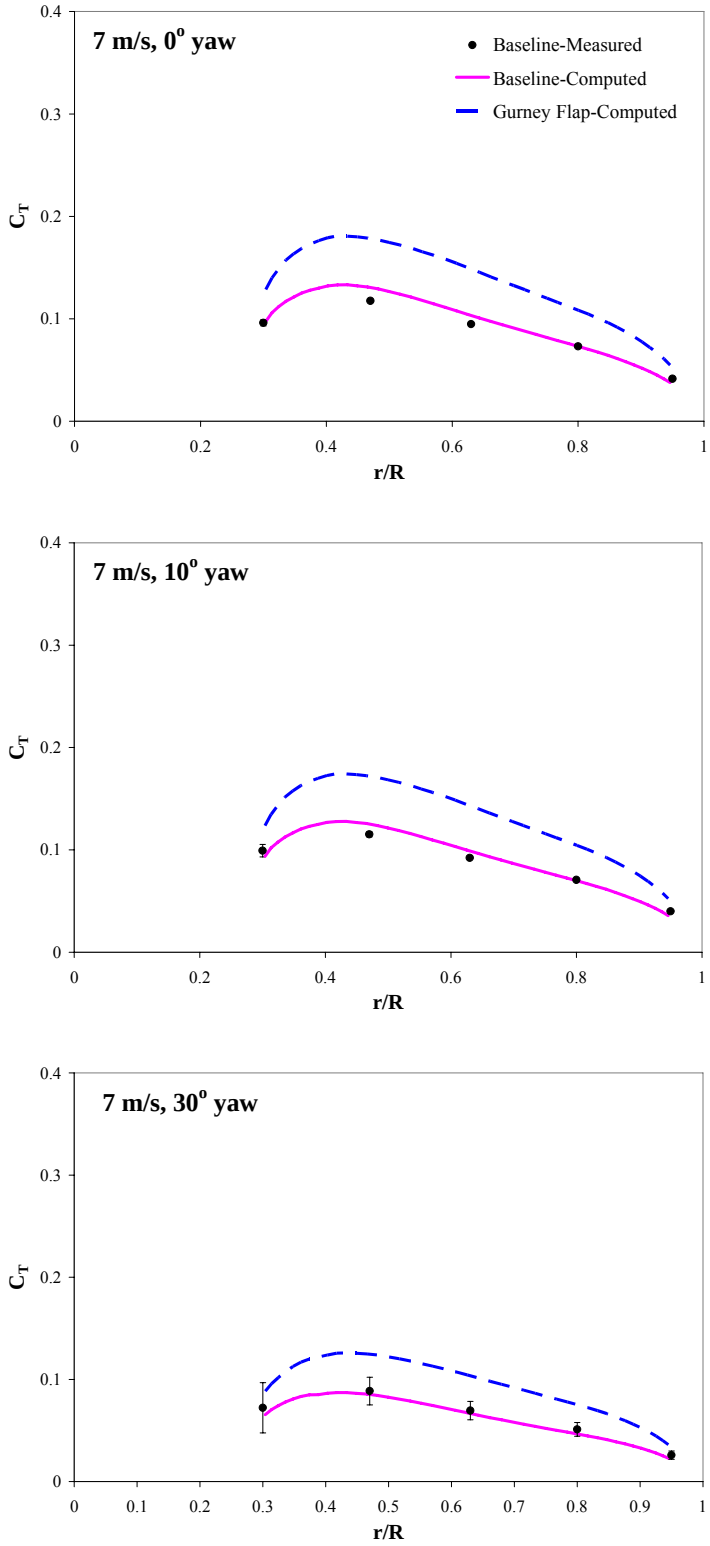

Figure 5.4 Radial distribution of the tangential force coefficient C_T at 7 m/s; with and without a Gurney flap

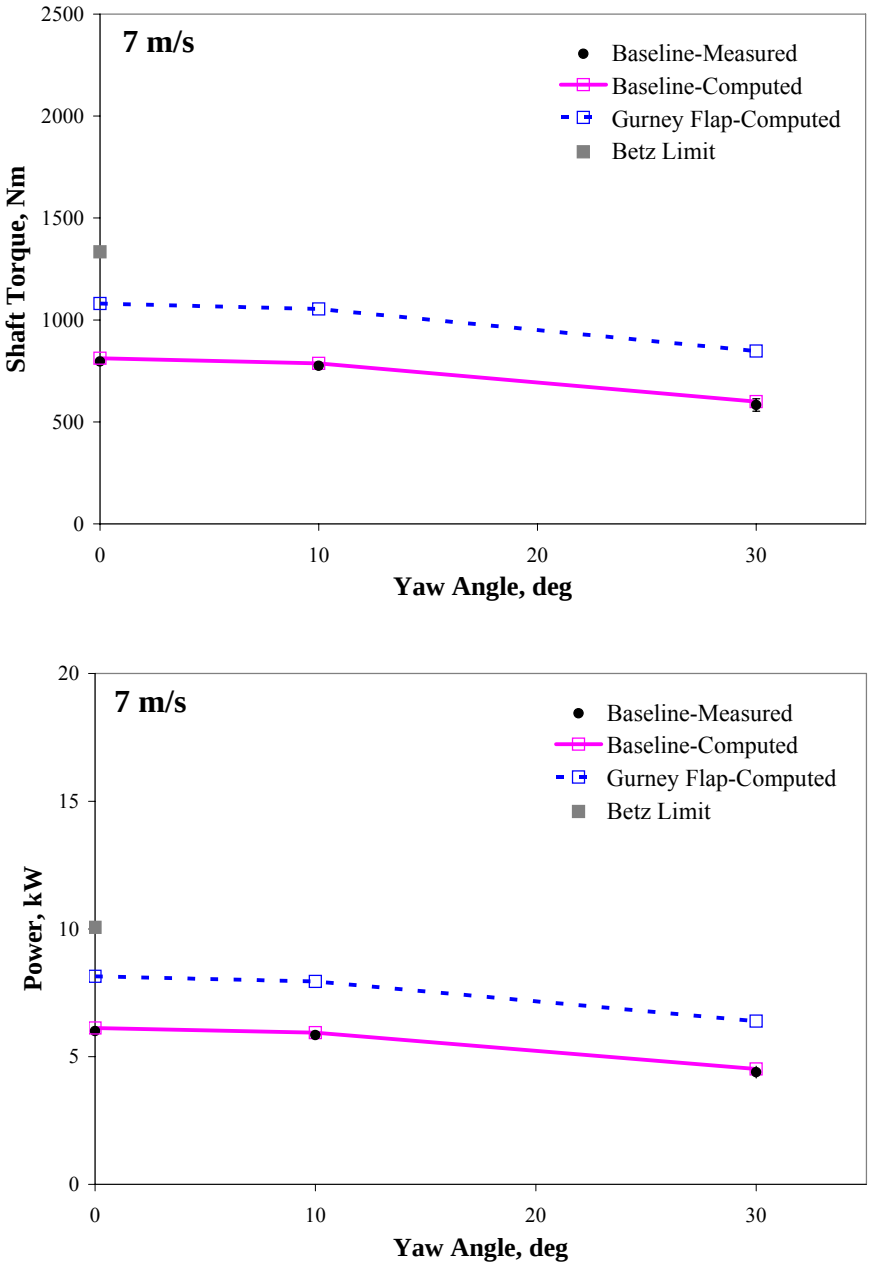

Figure 5.5 Variation of the shaft torque and the corresponding power at 7 m/s as a function of yaw angle; with and without a Gurney flap

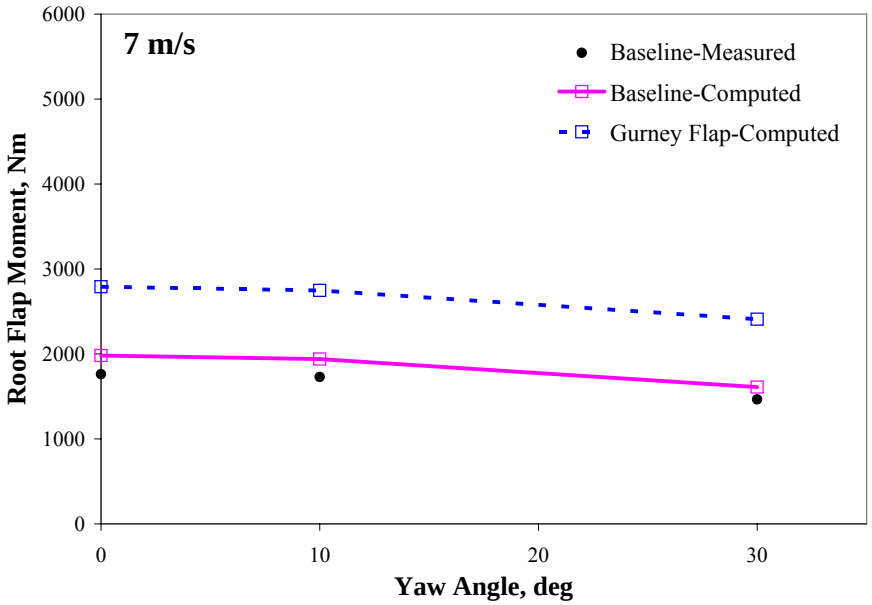

Figure 5.6 Variation of the root flap moment at 7 m/s as a function of yaw angle; with and without a Gurney flap

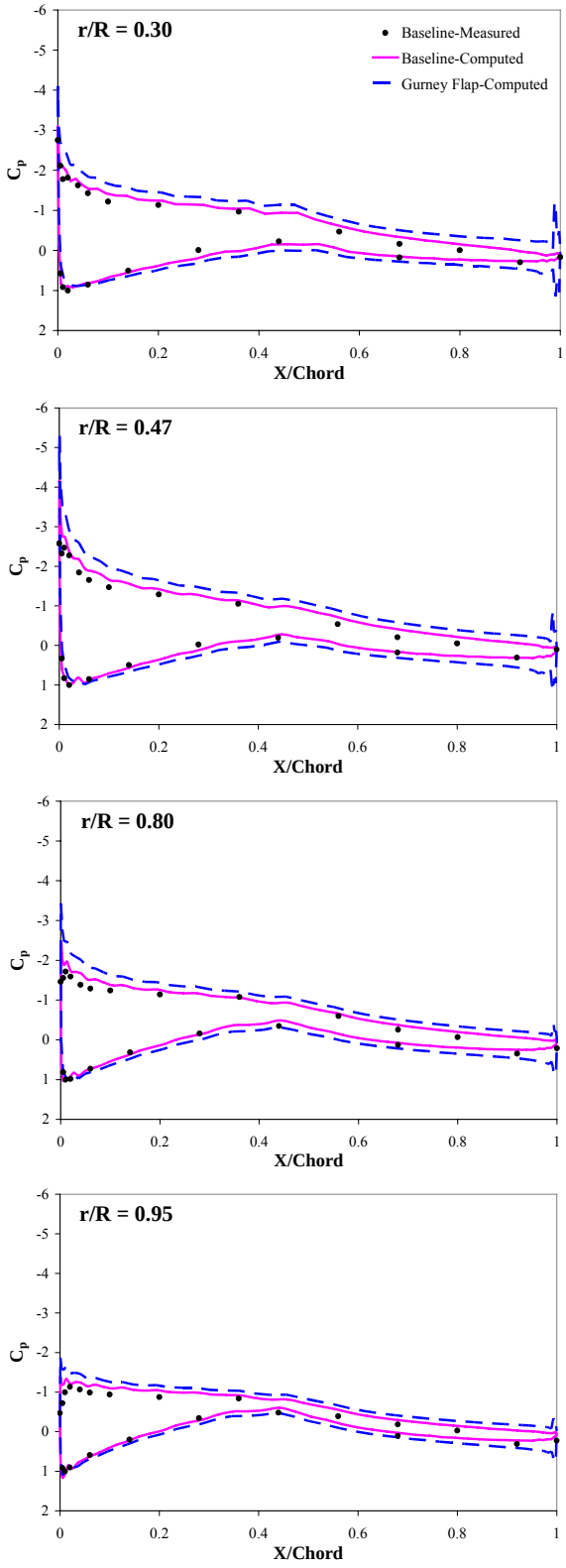

Figure 5.7 Comparison of pressure coefficient distribution at 7 m/s, 0° yaw; with and without a Gurney flap

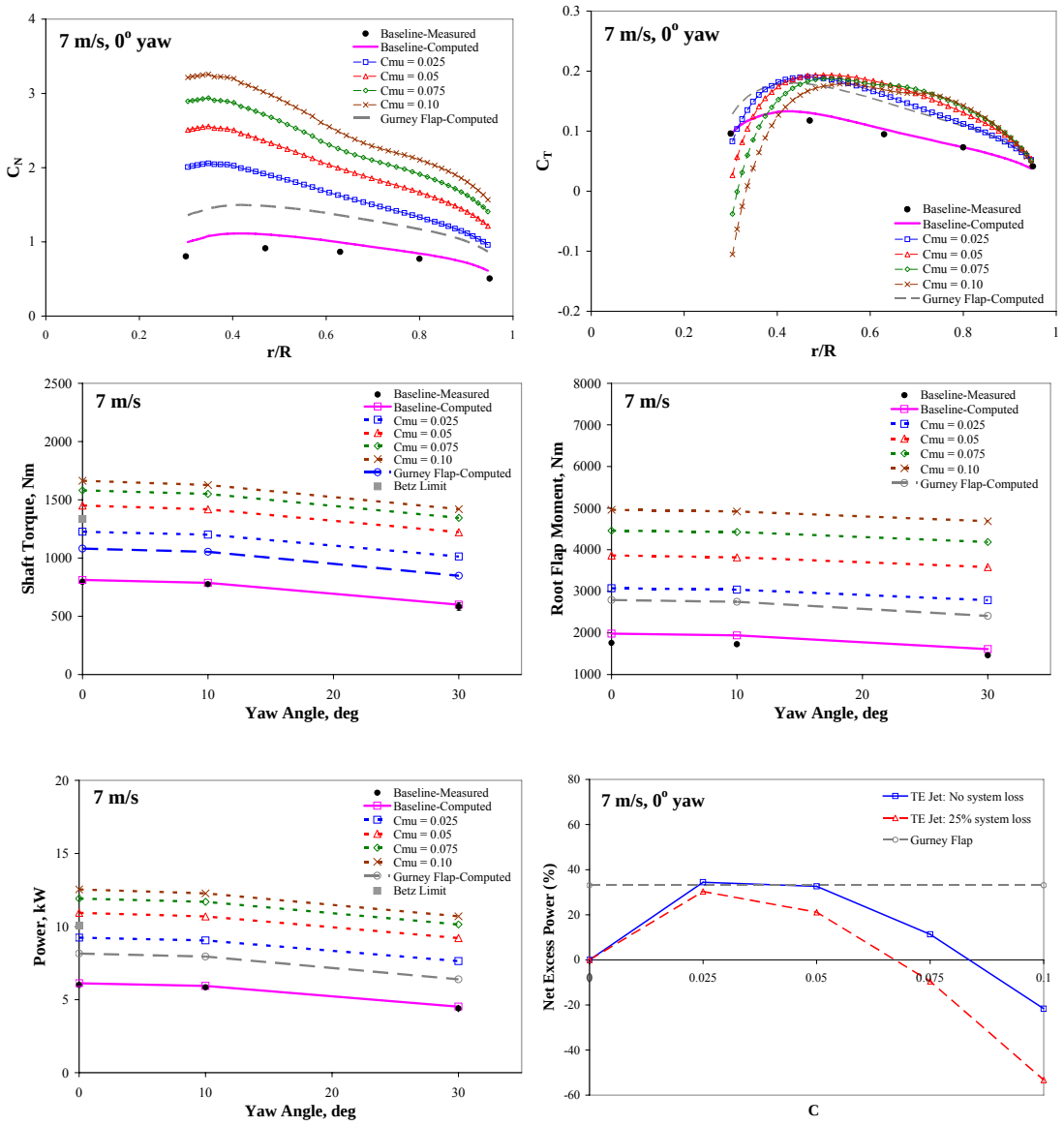

Figure 5.8 Comparisons of performance of trailing edge blowing jet and gurney flap at 7 m/s and zero yaw

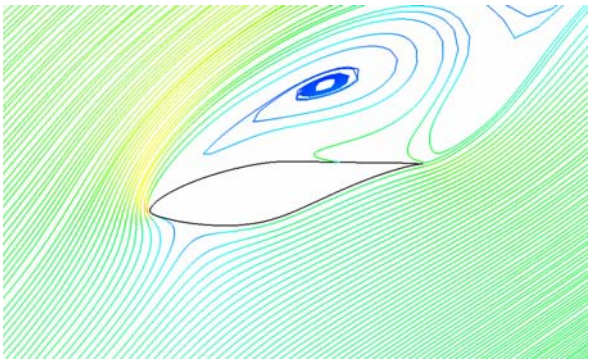

(a) Without the Gurney flap

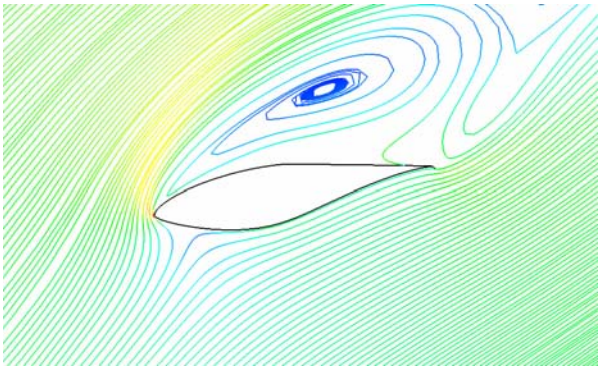

(b) With the Gurney flap

Figure 5.9 Computed streamlines over the rotor at 15 m/s, 0° yaw; Gurney flap case

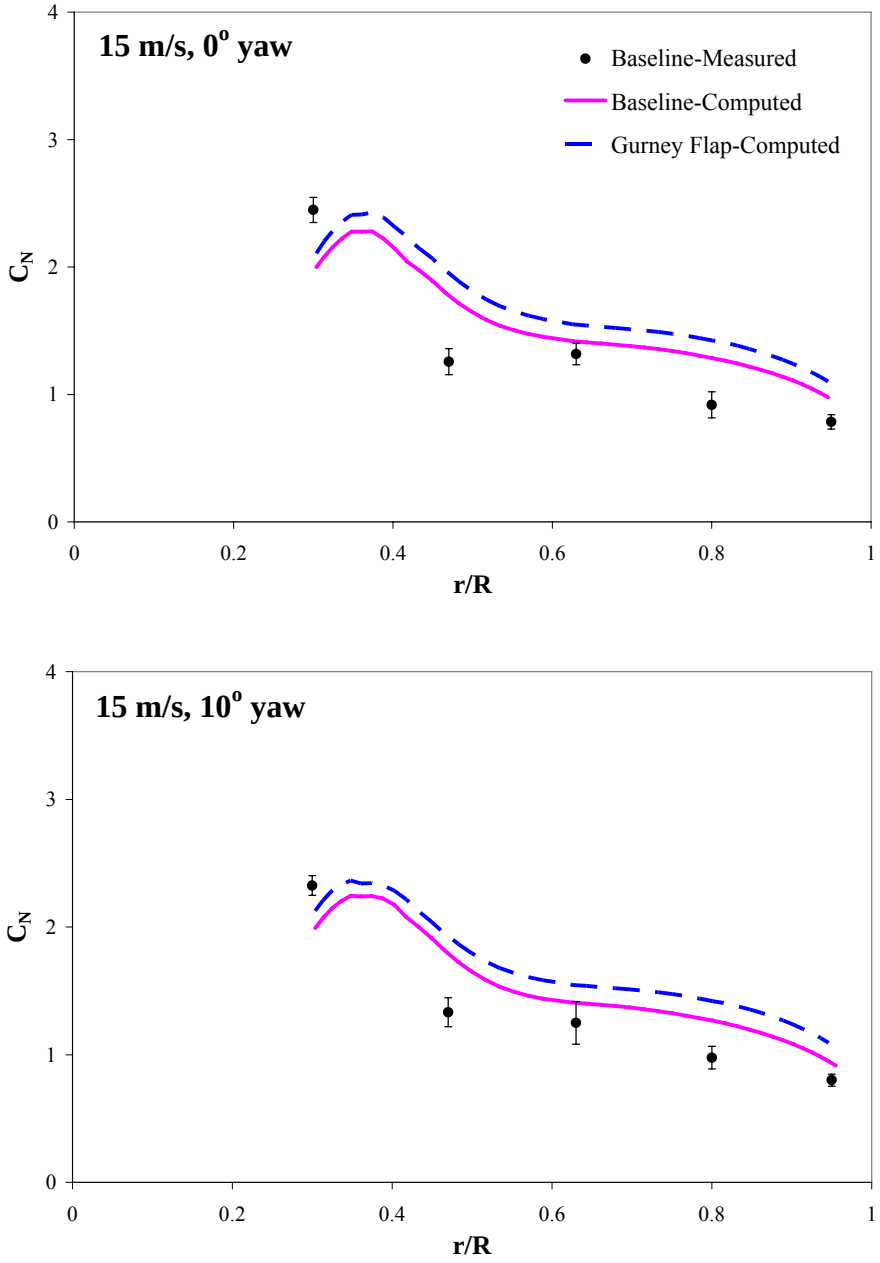

Figure 5.10 Radial distribution of the normal force coefficient C_N at 15 m/s (0° and 10° yaw); with and without a Gurney flap

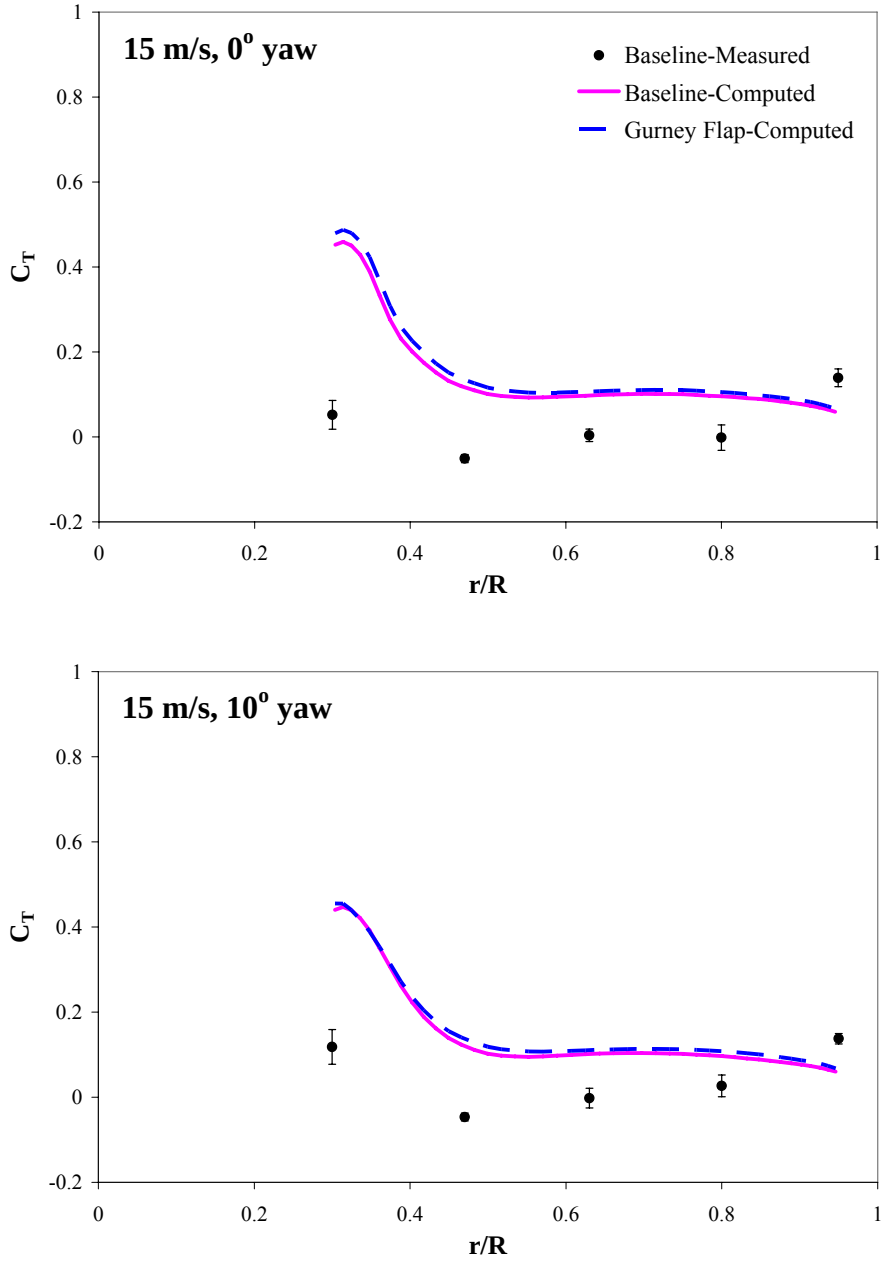

Figure 5.11 Radial distribution of the tangential force coefficient C_T at 15 m/s (0° and 10° yaw); with and without a Gurney flap

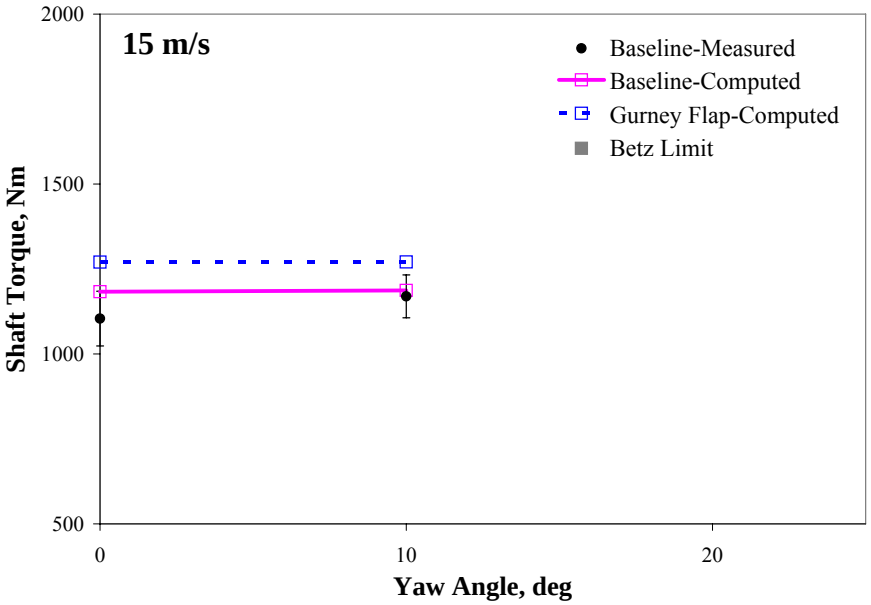

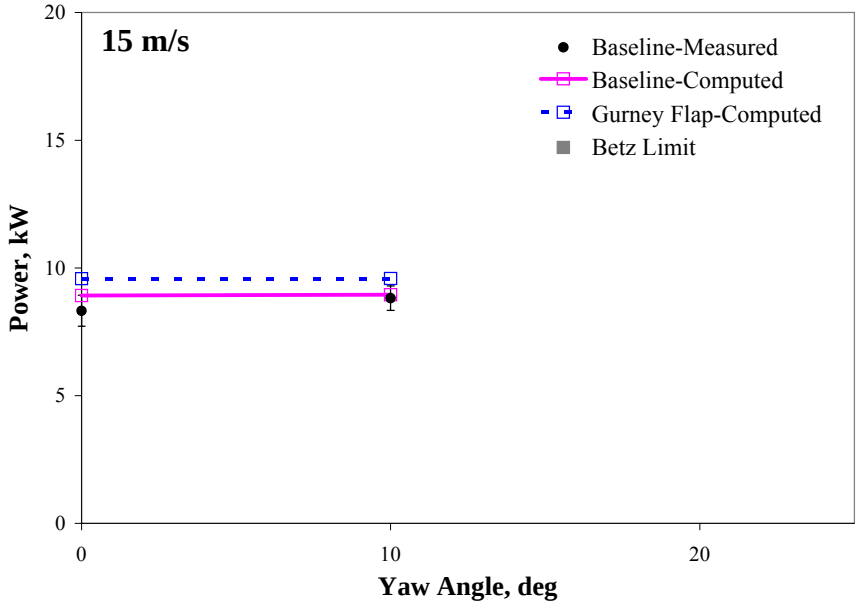

Figure 5.12 Variation of the shaft torque and the corresponding power at 15 m/s; with and without a Gurney flap (At zero yaw, the Betz limit is approximately 13,100 Nm and 98 kW, respectively)

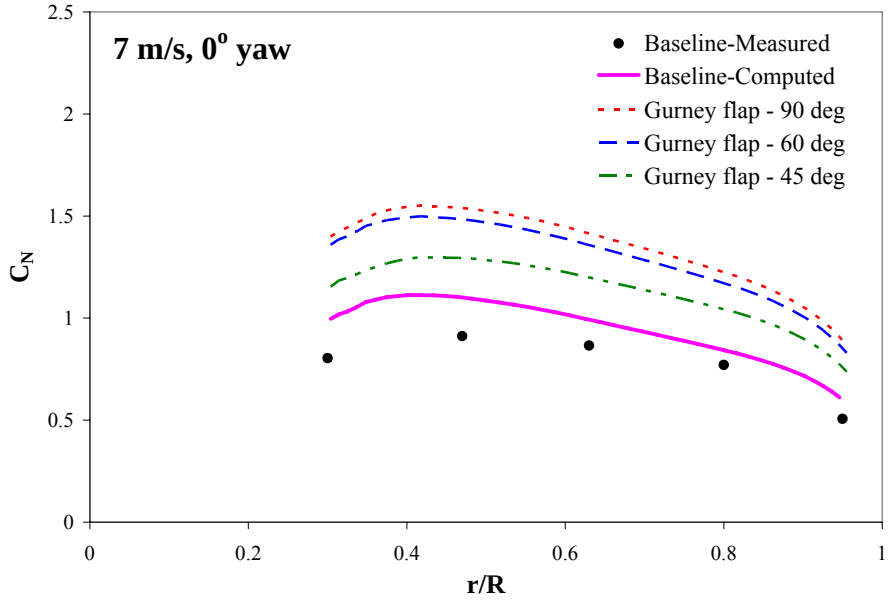

Figure 5.13 Radial distribution of the normal force coefficient C_N at 7 m/s and zero yaw with varying Gurney flap angle

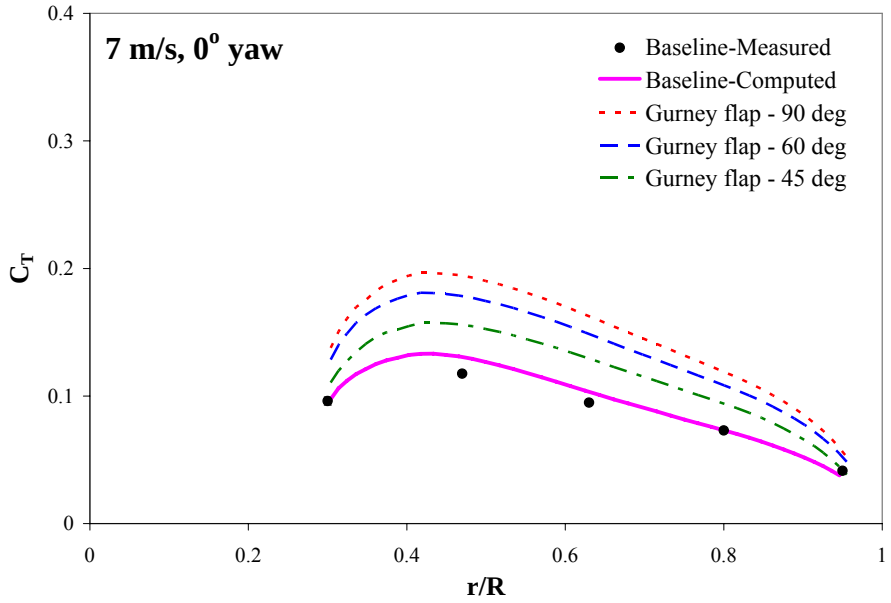

Figure 5.14 Radial distribution of the tangential force coefficient C_T at 7 m/s and zero yaw with varying Gurney flap angle

CHAPTER 6

CONCLUSIONS AND RECOMMENDATIONS

A first principles based method for modeling the aerodynamics of horizontal axis wind turbine has been developed. This analysis has been validated for the NREL Phase VI rotor tested at NASA Ames Research Center. Good agreement has been for a range of low wind speeds and yaw angles, although at high wind speeds the fundamental assumptions behind this approach breaks down for the turbulence model, giving less accurate results. Comparisons have been done against measurements for surface pressure distribution, force coefficients normal and tangential to the chord line, torque and root bending moments. Flow visualization studies have also been done to understand the physical phenomena of interest. Two approaches (using trailing edge blowing and Gurney flap) for enhancing the circulation around the airfoil sections (and hence L/D and power production) have been examined and found to produce useful increases in power at low wind speeds. A leading edge blowing jet is found to be helpful in increasing power generation at high wind speeds**.**

The following conclusions may be drawn from this study.

1. The present methodology is accurate for a range of wind speeds and yaw of interest to wind energy industry. At extreme wind conditions and yaw angles the method breaks down.
2. Because a phenomenological model is used to capture physical phenomena that influence the flow, calculations can be confined to a relatively small region

around the rotor disk, leading to efficient solutions, of the order of 40 hours per cage on a single CPU PC system.

3. For attached flow conditions, circulation control technology (using trailing edge blowing) and Gurney flap both are very effective at increasing circulation around the airfoil section leading to a net increase in generated power compared to the baseline rotor.
4. Active control of circulation (trailing edge blowing) resulted in greater blade forces and power output compared to the purely passive concept (Gurney flap) but the net excess power obtained from circulation control is comparable to that from Gurney flap. However, Gurney flap concept is more easily implemented and requires no external power source or compressed air supply.
5. At high wind speed conditions, where the flow is separated, the trailing edge blowing and the Gurney flap both become ineffective in increasing the power output. It was found that leading edge blowing can be used to create large leading edge suction, which leads to increased torque and power generation.
6. A thinner steady jet and a pulsed jet both use less mass flow rate, compared to a thicker steady jet. However, they require a higher input power. The slot height, and hence the thickness of the jet, must therefore be chosen from mass flow rate availability and power production considerations, both.
7. Although we have modeled only HAWT configuration in this study, this methodology is also applicable to other configurations such as water turbines, multi-stage coaxial turbines, and VAWTs.

The following topics are recommended for further study:

1. The present approach lends itself to a distributed computing architecture. Versions of this solver have been parallelized using MPI method passing paradigm, but have not been systematically tested or optimized. Further work in this area is needed. This will allow the designers to parametrically study the effects of flow conditions, and rotor blade geometries (taper ratio, twist, airfoil shape, etc) and thus reduce the time consumed in the design process. A user-friendly interface for setting up the calculations and a built-in grid generator are also recommended.
2. Recently, Sarun Benjanirat has implemented SA-DES and k-ω SST turbulence models and applied them to HAWTs for axial flow conditions. Only the SA-DES model was implemented in this study for yawed flow conditions. Additional systematic studies are needed to validate these advanced turbulence models.
3. Coupling this methodology with comprehensive structural analyses such as RCAS or DYMORE will allow the designers to better model the aeroelastic effects.
4. An advantage of this methodology is its ability to capture and visualize the flow physics in great details. To date, only the engineering quantities of interest have been extracted and validated. It is recommended that a detailed post-processing of the results from this study be used to understand phenomena such as 3D dynamic stall, stall delay, tip and root losses, wake structure, blade-vortex interaction, and tower effects, and to improve the empirical models currently in use in blade element theory based approaches such as YawDyn for modeling these complex phenomena.

5. In addition to blowing jet and Gurney flap, there are other interesting techniques (both active and passive control) that are available for enhancing the wind turbine performance. These include synthetic jet devices, flatback airfoils, vortex fence, nose droop, and miniature trailing edge effectors (MiTEs). These potential concepts should be systematically explored.

In summary, this work has been an attempt to use modern computational aerodynamics techniques to model and explore the fascinating world of wind turbines, and for arriving at predicting tools free of empiricism (except in the turbulence model) for predicting wind power generation for a user supplied configuration at a user specified wind speed and yaw angle. It is hoped that this work will serve as a stepping stone for further studies in this exciting and personally fulfilling area of research.

REFERENCES

[1] Gasch, R. and Twele, J., *Wind Power Plants*, Solarpraxis AG, Berlin, Germany, 2002.

[2] Shepherd, D. G., "Historical Development of the Windmill," NASA Contractor Report 4337, DOE/NASA/5266-1, 1990.

[3] Sepera, D. A., *Wind Turbine Technology: Fundamental Concepts of Wind Turbine Engineering*, ASME Press, New York, 1994.

[4] Gipe, P., *Wind Energy Comes of Age*, John Wiley & Sons, New York, 1995.

[5] Harrison, R., Hau, E., and Snel, H., *Large Wind Turbines: Design and Economics, John Wiley & Sons*, Chichester, 2000.

[6] Hansen, M. O. L., *Aerodynamics of Wind Turbines*, James & James, London, UK, 2000.

[7] Xu, G. and Sankar, L. N., "Effects of Transition, Turbulence and Yaw on the Performance of Horizontal Axis Wind Turbines," AIAA Paper 2000-0048, 2000.

[8] Benjanirat, S., Sankar, L. N., and Xu, G., "Evaluation of Turbulence Models for the Prediction of Wind Turbine Aerodynamics," AIAA Paper 2003-0517, 2003.

[9] Duque, E. P. N., Burklund, M. D., and Johnson, W., "Navier-Stokes and Comprehensive Analysis Performance Predictions of the NREL Phase VI Experiment," AIAA Paper 2003-0355, 2003.

[10] Madsen, H. A., Sorensen, N. N., and Schreck, S., "Yaw Aerodynamics Analyzed with Three Codes in Comparison with Experiment," AIAA Paper 2003-0519, 2003.

[11] Xu, G. and Sankar, L. N., "Computational Study of Horizontal Axis Wind Turbines," AIAA Paper 99-0042, 1999.

[12] Xu, G., "Computational Studies of Horizontal Axis Wind Turbines," Ph.D. Dissertation, School of Aerospace Engineering, Georgia Institute of Technology, Atlanta, GA, 2001.

[13] Benjanirat, S. and Sankar, L. N., "Recent Improvement to a Combined Navier-Stokes Full Potential Methodology for Modeling Horizontal Axis Wind Turbines," AIAA Paper 2004-0830, 2004.

[14] Tongchitpakdee, C., Benjanirat, S., and Sankar, L. N., "Numerical Simulation of the Aerodynamics of Horizontal Axis Wind Turbines under Yawed Flow Conditions," *Journal of Solar Energy Engineering*, Vol. 127, Nov. 2005, pp. 464-474.

[15] Duque, E. P. N., van Dam, C. P., and Hughes, S., "Navier-Stokes Simulations of the NREL Combined Experiment Phase II Rotor," AIAA Paper 99-0037, 1999.

[16] Sørensen, N. N. and Hansen, M. O. L., "Rotor Performance Predictions using a Navier-Stokes Method," AIAA Paper 98-0025, 1998.

[17] Sørensen, N. N. and Michelsen, J. A., "Aerodynamic Predictions for the Unsteady Aerodynamics Experiment Phase-II Rotor at the National Renewable Energy Laboratory," AIAA Paper 2000-0037, 2000.

[18] Sørensen, N. N., Michelsen, J. A., and Schreck, S., "Prediction of the NREL/NASA Ames Wind Tunnel Test," AIAA Paper 2002-0031, 2002.

[19] Shaw, S. T., Hill, J. L., and Qin, N., "Application of Engineering Transition Models to an Isolated Helicopter Rotor in Hovering Flight," AIAA Paper 2005-0467, 2005.

[20] Englar, R. J. and Huson, G. G., "Development of Advanced Circulation Control Wing High Lift Airfoils," AIAA paper 83-1847, 1983.

[21] Englar. R. J., "Circulation Control Pneumatic Aerodynamics: Blown Force and Moment Augmentation and Modification; Past, Present and the Future," AIAA Paper 2000-2541, 2000.

[22] Englar, R. J., Smith, M. J., Kelley, S. M., and Rover, R. C. III., "Development of Circulation Control Technology for Application to Advanced Subsonic Aircraft," AIAA Paper 93-0644, 1993.

[23] Englar, R. J., Smith, M. J., Kelley, S. M., and Rover, R. C. III., "Application of Circulation Control to Advanced Subsonic Transport Aircraft, Part I: Airfoil Development," *Journal of Aircraft*, Vol. 31, No. 5, Sep. 1994, pp. 1160-1168.

[24] Englar, R. J., Smith, M. J., Kelley, S. M., and Rover, R. C. III., "Application of Circulation Control to Advanced Subsonic Transport Aircraft, Part II: Transport Application," *Journal of Aircraft*, Vol. 31, No. 5, Sep. 1994, pp. 1169-1177.

[25] Shrewsbury, G. D. and Sankar, L. N., "Dynamic Stall of Circulation Control Airfoils," AIAA Paper 90-0573, 1990.

[26] Liu, Y., Sankar, L. N., Englar, R. J., and Ahuja, K. K., "Numerical Simulations of the Steady and Unsteady Aerodynamic Characteristics of a Circulation Control Wing," AIAA Paper 2001-0704, 2001.

[27] Liu, Y., "Numerical Simulations of the Aerodynamic Characteristics of Circulation Control Wing Sections," Ph.D. Dissertation, School of Aerospace Engineering, Georgia Institute of Technology, Atlanta, GA, 2003.

[28] Liu, Y., Sankar, L. N., Englar, R. J., Ahuja, K. K., and Gaeta, R., "Computational Evaluation of the Steady and Pulsed Jet Effects on the Performance of a Circulation Control Wing Section," AIAA Paper 2004-0056, 2004.

[29] Chang III, P. A. and Slomski, J., "Numerical Simulation of Two- and Three-Dimensional Circulation Control Problems," AIAA Paper 2005-80, 2005.

[30] Swanson, R. C., Rumsey, C. L., and Anders, S. G., "Progress Towards Computational Method for Circulation Control Airfoils," AIAA Paper 2005-89, 2005.

[31] Metral, A. R., "On the Phenomenon of Fluid Veins and their Application, the Coanda Effect," AF Translation, F-TS-786-RE, 1939.

[32] Lieback, R. H., "Design of Subsonic Airfoils for High Lift," *Journal of Aircraft*, Vol. 15, No. 9, Sep. 1978, pp. 547-561.

[33] Neuhart, D. H. and Pendergraft Jr., O. C., "A Water Tunnel Study of Gurney Flaps," NASA TM 4071, 1988.

[34] Jang, C. S., Ross, J. C., and Cummings, R. M., "Computational Evaluation of an Airfoil with a Gurney Flap," AIAA Paper 92-2708, 1992, pp. 801-809.

[35] Giguère, P., Lemay, J., and Dumas, G., "Gurney Flap Effects and Scaling for Low-Speed Airfoils," AIAA Paper 95-1881, 1995.

[36] Storms, B. L. and Jang, C. S., "Lift Enhancement of an Airfoil Using a Gurney Flap and Vortex Generators," *Journal of Aircraft*, Vol. 31, No. 3, May 1994, pp. 542-547.

[37] Jeffrey, D. R. M. and Hurst, D. W., "Aerodynamics of the Gurney Flap," AIAA Paper 96-2418, 1996.

[38] Myose, R., Papadakis, M., and Heron, I., "Gurney Flap Experiments on Airfoils, Wings, and Reflection Plane Model," *Journal of Aircraft*, Vol. 35, No. 2, Mar. 1998, pp. 206-211.

[39] van Dam, C. P., Yen, D. T., Vijgen, P. M. H. W., "Gurney Flap Experiments on Airfoil and Wings," *Journal of Aircraft*, Vol. 36, No. 2, Mar. 1999, pp.484-486.

[40] Brown, L. and Filippone, A., "Aerofoil at Low Speeds with Gurney Flaps," *The Aeronautical Journal*, Vol. 107, No. 1075, Sep. 2003, pp. 539-546.

[41] Chandrasekhara, M. S., Martin, P. B., and Tung, C., "Compressible Dynamic Stall Performance of Variable Droop Leading Edge Airfoil with a Gurney Flap," AIAA Paper 2004-0041, 2004.

[42] Rhee, M., "A Computational Study of an Oscillating VR-12 Airfoil with a Gurney Flap," AIAA Paper 2004-5202, 2004.

[43] Guzel, G., Sankar, L. N., and Rhee, M., "Computational Investigation of the Effects of Gurney Flap on the Aerodynamic Performance of VR-12 Airfoil," AIAA Paper 2005-4960, 2005.

[44] Bieniawski, S. and Kroo, I. M., "Flutter Suppression Using Micro-Trailing Edge Effectors," AIAA Paper 2003-1941, 2003.

[45] Lee, H., Kroo, I. M., and Bieniawski, S., "Flutter Suppression for High Aspect Ratio Flexible Wings Using Microflaps," AIAA Paper 2002-1717, 2002.

[46] Lee, H. and Kroo, I. M., "Computational Investigation of Airfoils with Miniature Trailing Edge Control Surfaces," AIAA Paper 2004-1051, 2004.

[47] Yen, D. T., van Dam, C. P., Bräeuchle, F., Smith, R. L., and Collins, S. D., "Active Load Control and Lift Enhancement Using MEM Translational Tabs," AIAA Paper 2000-2422, 2000.

[48] Yen, D. T., van Dam, C. P., Smith, R. L., and Collins, S. D., "Active Load Control for Airfoils Using Microtabs," *Journal of Solar Energy Engineering*, Vol. 123, No. 4, Nov. 2001, pp. 282-289.

[49] Yen, D. T., van Dam, C. P., Michel, J., and Morrison, P., "Load Control for Turbine Blades: A Non-Traditional Microtab Approach," AIAA Paper 2002-0054, 2002.

[50] Butterfield, C. P., Musial, W. P., and Simms, D. A., "Combined Experiment Phase I, Final Report," National Renewable Energy Laboratory, NREL/TP-257-4655, Golden, CO, Oct. 1992.

[51] Simms, D. A., Hand, M. M., Fingersh, L. J., and Jager, D. W., "Unsteady Aerodynamics Experiment Phase II-IV Test Configurations and Available Data Campaigns," National Renewable Energy Laboratory, NREL/TP-500-25950, Golden, CO, 1999.

[52] Hand, M. M., Simms, D. A., Fingersh, L. J., Jager, D. W., and Cotrell, J. R., "Unsteady Aerodynamics Experiment Phase V: Test Configuration and Available Data Campaigns," National Renewable Energy Laboratory, NREL/TP-500-29491, Golden, CO, Dec. 2001.

[53] Laino, D. J. and Butterfield, C. P., "Using YawDyn to Model Turbines with Aerodynamic Control Systems," ASME Wind Energy Conference, New Orleans, 1994.

[54] Hansen, A. C. and Laino, D. J., "User's Guide to the Wind Turbine Dynamics Computer Programs YawDyn and AeroDyn for ADAMS," 1999. Available for download from http://wind.nrel.gov/designcodes/simulators/yawdyn/ (December 2006)

[55] Selig, M. S. and Tangler, J. L., "Development and Application of a Multipoint Inverse Design Method for Horizontal Axis Wind Turbines," *Wind Engineering*, Vol. 19, No. 2, 1995, pp. 91-105.

[56] Giguère, P. and Selig, M. S., "Aerodynamic Blade Design Methods for Horizontal Axis Wind Turbines," 13th Annual Canadian Wind Energy Association Conference and Exhibition, Quebec City, Quebec, Canada, October 19-22, 1997.

[57] Giguère, P. and Selig, M. S., "Design of a Tapered and Twisted Blade for the NREL Combined Experiment Rotor", National Renewable Energy Laboratory, NREL/SR-500-26173, Golden, CO, Apr. 1999.

[58] Hand, M. M., Simms, D. A., Fingersh, L. J., Jager, D. W., Cotrell, J. R., Schreck, S., and Larwood, S. M., "Unsteady Aerodynamics Experiment Phase VI: Wind Tunnel Test Configurations and Available Data Campaigns," National Renewable Energy Laboratory, NREL/TP-500-29955, Golden, CO, Dec. 2001.

[59] http://www.airfoils.com (December 2006), Airfoils, Incorporated, 122 Rose Drive, Port Matilda, PA 16870-9483 U.S.A.

[60] Somers, D. M., "Design and Experimental Results for the S809 Airfoil," National Renewable Energy Laboratory, NREL/SR-440-6918, 1997.

[61] Kwon, J. and Sankar, L. N., "Numerical Simulation of the Effects of Icing on Finite Wing Aerodynamics," AIAA Paper 90-0757, 1990.

[62] Bangalore, A., Phaengsook, N., and Sankar, L. N., "Application of a Third Order Upwind Scheme to Viscous Flow over Clean and Iced Wings," AIAA Paper 94-0485, 1994.

[63] Sankar, L. N., Wake, B., and Lekoudis, S. G., "Solutions of the Euler Equations for Fixed and Rotary-Wing Configurations," *Journal of Aircraft*, Vol. 23, No. 4, Apr. 1986, pp. 283-289.

[64] Wake, B. E. and Sankar, L. N., "Solutions of the Navier-Stokes Equations for the Flow about a Rotor Blade," *Journal of the American Helicopter Society*, Vol. 34, No. 2, 1989, pp. 13-23.

[65] Berezin, C. R., "A Coupled Navier-Stokes/Full-Potential Analysis for Rotors," Ph.D. Dissertation, School of Aerospace Engineering, Georgia Institute of Technology, Atlanta, GA, 1995.

[66] Pulliam, T. H. and Steger, J. L., "Implicit Finite-Difference Simulations of Three-Dimensional Compressible Flow," *AIAA Journal*, Vol. 18, No. 2, 1980, pp. 159-167.

[67] Vinokur, M., "An Analysis of Finite Difference and Finite Volume Formulations of Conservation Laws," *Journal of Computational Physics*, Vol. 81, 1989, pp. 1-52.

[68] Jameson, A., Schmidt, W., and Turkel, E., "Numerical Solution of the Euler Equations by Finite Volume Methods Using Runge-Kutta Time-Stepping Schemes," AIAA Paper 81-1259, 1981.

[69] Steger, J. L. and Warming, R. F., "Flux Vector Splitting of the Inviscid Gasdynamic Equations with Application to Finite-Difference Methods," NASA TM D-78605, 1979.

[70] van Leer, B., "Flux Vector Splitting for the Euler Equations," Proceedings of the 8th International Conference on Numerical Methods in Fluid Dynamics, *Lecture Notes in Physics*, Vol. 170, Springer-Verlag, New York, 1982, pp. 507-512.

[71] Liou, M.-S. and Steffan, C., "A New Flux Splitting Scheme," NASA TM-104404, 1991.

[72] Godunov, S. K., "A Finite-Difference Method for the Numerical Computation and Discontinuous Solutions of the Equations of Fluid Dynamics," *Matematicheskii Sbornik*, Vol. 47, 1959, pp.271-306.

[73] Roe, P. L., "The Use of the Riemann Problem in Finite-Difference Schemes," *Lecture Notes in Physics*, Vol. 141, Springer-Verlag, New York, 1980, pp. 354-359.

[74] Roe, P. L., "Approximate Riemann Solvers, Parameter Vectors, and Difference Schemes," *Journal of Computational Physics*, Vol. 43, 1981, pp. 357-372.

[75] Osher, S., "Riemann Solvers, Entropy Conditions and Difference Approximations," *SIAM Journal on Numerical Analysis*, Vol. 21, 1984, pp. 217-235.

[76] Vinokur, M. and Liu, Y., "Equilibrium Gas Flow Computations II: An Analysis of Numerical Formulations of Conservation Laws," AIAA Paper 88-0127, 1988.

[77] Roe, P. L. and Pike, J., "Efficient Construction and Utilization of Approximate Riemann Solutions," *Computing Methods in Applied Sciences and Engineering*, R. Glowinski and J. L. Lions, eds., North Holland, Amsterdam, 1985.

[78] van Leer, B., "Towards the Ultimate Conservative Difference Scheme, V: A Second Order Sequel to Godunov's Method," *Journal of Computational Physics*, Vol. 32, 1979, pp. 101-136.

[79] van Leer, B., "Upwind Difference Methods for Aerodynamic Problems Governed by the Euler Equations," *Lectures in Applied Mathematics*, Vol. 22, 1985.

[80] van Albada, G. D., van Leer, B., and Roberts, W. W. Jr., "Comparative Study of Computational Methods in Cosmic Gas Dynamics," *Astronomy and Astrophysics*, Vol. 108, 1982, pp. 76-84.

[81] Thomas, J. L. and Walters, R. W., "Upwind Relaxation Algorithms for Navier-Stokes Equations," *AIAA Journal*, Vol. 25, 1987, pp. 527-537.

[82] Venkatakrishnan, V., "On the Accuracy of Limiters and Convergence to Steady State Solutions," AIAA Paper 93-0880, 1993.

[83] Kermani, M. J., Gerber, A. G., and Stockie, J. M, "Thermodynamically Based Moisture Prediction Using Roe's Scheme," 4th Conference of Iranian Aerospace Society, Amir Kabir University of Technology, Tehran, Iran, January 27-29, 2003.

[84] Beam, R. and Warming, R. F., "An Implicit Finite Difference Algorithm for Hyperbolic Systems in Conservation Law Form," *Journal of Computational Physics*, Vol. 22, Sep. 1976, pp. 87-110.

[85] Pulliam, T. H. and Chaussee, D. S., "Three-Dimensional Viscous-Flow Computations Using a Directionally Hybrid Implicit-Explicit Procedure," AIAA Paper 83-1910, 1983.

[86] Yoon, S. and Jameson, A., "An LU-SSOR Scheme for the Euler and Navier-Stokes Equations," AIAA Paper 87-0600, 1987.

[87] Yoon, S. and Jameson, A., "Lower-Upper Symmetric-Gauss-Seidel Method for the Euler and Navier-Stokes Equations," *AIAA Journal*, Vol. 26, No. 9, Sep. 1988, pp. 1025-1026.

[88] Rieger, H. and Jameson, A., "Solution of the Three-Dimensional Compressible Euler and Navier-Stokes Equations by an Implicit LU Scheme," AIAA Paper 88-0619, 1988.

[89] Obayashi, S. and Kuwahara, K., "An Approximate LU Factorization Method for the Compressible Navier-Stokes Equations," *Journal of Computational Physics*, Vol. 63, 1986, pp. 157-167.

[90] Pulliam, T. H. and Chaussee, D. S., "A Diagonal Form of an Implicit Approximate-Factorization Algorithm," *Journal of Computational Physics*, Vol. 39, 1981, pp. 347-363.

[91] Spalart, P. R. and Allmaras, S. R., "A One-Equation Turbulence Model for Aerodynamic Flows," AIAA Paper 92-0439, 1992.

[92] Spalart, P. R, Jou, W.-H., Strelets, M., and Allmaras, S. R., "Comments on the Feasibility of LES for Wings and on a Hybrid RANS/LES Approach," *Proceeding of the 1st AFOSR International Conference on DNS/LES*, Ruston, LA, 1997, pp.137-147.

[93] Benjanirat, S., "Computational Studies of Horizontal Axis Wind Turbines in High Wind Speed Condition Using Advanced Turbulence Models," Ph.D. Dissertation, School of Aerospace Engineering, Georgia Institute of Technology, Atlanta, GA, 2006.

[94] Eppler, R., *Airfoil Design and Data*, Springer-Verlag, New York, 1990, 562 pp.

[95] Michel, R., Arnal, D., and Coustols, E., "Stability Calculations and Transition Criteria on Two- or Three-Dimensional Flows," *Laminar-Turbulent Transition*, V. V. Koslov, ed., Springer-Verlag, New York, 1985, pp. 455-462.

[96] Spalart, P. R. and Allmaras, S. R., "A One-Equation Turbulence Model for Aerodynamic Flows," *La Recherche Aerospatiale*, 1994.

[97] Hoffmann, K. A. and Chiang, S. T., *Computational Fluid Dynamics Volume III*, Fourth Edition, Engineering Education System, Kansas, 2000, 175 pp.

[98] Wilcox, D. C., *Turbulence Modeling for CFD*, Third Edition, DCW Industries, 2006, 552 pp.

[99] Shur, M., Spalart, P. R., Strelets, M., and Travin, A., "Detached-Eddy Simulation of an Airfoil at High Angle of Attack," *4th Int. Symposium on Eng. Turb. Modeling and Experiments*, Corsica, France, May 1999.

[100] Chen, K. K. and Thyson, N. A., "Extension of Emmons' Spot Theory to Flow on Blunt Bodies," *AIAA Journal*, Vol. 9, 1971, pp. 821-825.

[101] Cebeci, T., "Essential Ingredients of a Method for Low Reynolds-Number Airfoils," *AIAA Journal*, Vol. 27, No. 12, December 1989, pp. 1680-1685.

[102] Kocurek, D., "Lifting Surface Performance Analysis for Horizontal Axis Wind Turbines," Solar Energy Research Institute, SERI/STR-217-3163, 1987.

[103] Kocurek, J. D., and Tangler, J. L., "A Prescribed Wake Lifting Surface Hover Performance Analysis," *Journal of the American Helicopter Society*, Vol. 22, No. 1, Jan. 1977, pp. 24-35.

[104] Simms, D. A., Schreck, S., Hand, M. M., and Fingersh, L. J, "NREL Unsteady Aerodynamics Experiment in the NASA-Ames Wind Tunnel: A Comparison of Predictions to Measurements," NICH Report No. TP-500-29494, 2001.

[105] Fingersh, L. J., Simms, D. A., Hand, M. M., Jager, D. W., Cotrell, J. R., Robinson, M., Schreck, S., and Larwood, S. M., "Wind Tunnel Testing of NREL's Unsteady Aerodynamics Experiment," AIAA Paper 2001-0035, 2001.

[106] Sørensen, N. N., Michelsen, J. A., and Schreck, S., "Navier-Stokes Predictions of the NREL Phase VI Rotor in the NASA Ames 80ft × 120ft Wind Tunnel," *Wind Energy*, Vol. 5, 2002, pp. 151-169.

[107] McCroskey, W. J., Carr, L. W., and McAlister, K. W., "Dynamic Stall Experiments on Oscillating Airfoils," *AIAA Journal*, Vol. 14, No. 1, January 1976, pp.57-63.

[108] Leishman, J. G. and Beddoes, T. S., "A Semi-Empirical Model for Dynamic Stall," *Journal of the American Helicopter Society*, Vol. 34, No. 3, July 1989, pp. 3-17.

[109] Munro, S., "Jet Noise of High Aspect-Ratio Rectangular Nozzles with Application to Pneumatic High-Lift Devices," Ph.D. Dissertation, School of Aerospace Engineering, Georgia Institute of Technology, Atlanta, GA, 2002.

[110] Munro, S. and Ahuja, K. K., "Aeroacoustics of a High Aspect-Ratio Jet," AIAA Paper 2003-3323, 2003.

[111] Maughmer, M., Lesieutre, G., Thepvongs, S., Anderson, W., and Kinzel, M., "Miniature Trailing-Edge Effectors for Rotorcraft Applications," *American Helicopter Society 59th Annual Forum Proceedings*, Phoenix, AZ, May 6-8, 2003.

[112] Kinzel, M. P., Maughmer, M. D., Lesieutre, G. L, and Duque, E. P. N., "Numerical Investigation of Miniature Trailing-Edge Effectors on Static and Oscillating Airfoils," AIAA Paper 2005-1039, 2005.

[113] Kinzel, M. P., Maughmer, M. D., and Lesieutre, G. A., "Miniature Trailing-Edge Effectors for Rotorcraft Performance Enhancement," *Journal of the American Helicopter Society*, Vol. 52, No. 2, 2007, pp. 146-158.

VITA

CHANIN TONGCHITPAKDEE

Chanin Tongchitpakdee was born on February 4, 1977 in Bangkok, Thailand. He completed high school program in March 1993 at Watsuthiwararam School, Bangkok. In March 1997, Chanin received a B.Eng. (First-class Honors) in Aerospace Engineering from Kasetsart University, Bangkok, where he worked as a lecturer later until December 1999. Chanin received a scholarship from The Anandamahidol Foundation under the Royal Patronage of His Majesty the King of Thailand to pursue graduate study at School of Aerospace Engineering, Georgia Institute of Technology in January 2000. Chanin earned his M.Sc. in Aerospace Engineering in August 2001. He worked as a graduate research assistant in the experimental aerodynamics group until May 2003 and then joined the CFD group to pursue his doctorate under supervision of Prof. Lakshmi N. Sankar. He is a student member of the American Institute of Aeronautics and Astronautics and the American Helicopter Society.